SYNTHETIC APERTURE RADAR DATA COMPRESSION AND FEATURE EXTRACTION

by

ABDELHAKIM EL-BOUSTANI

A Thesis

Submitted to the Faculty of Graduate Studies

in Partial Fulfilment of the Requirements

for the Degree of

DOCTOR OF PHILOSOPHY

Department of Electrical and Computer Engineering

University of Manitoba

Winnipeg, Manitoba, Canada

Thesis Advisor: Professor W. Kinsner, Ph. D., P. Eng.

(xvi + 179 +A10 = 205 pp)

THE UNIVERSITY OF MANITOBA

FACULTY OF GRADUATE STUDIES

*****

COPYRIGHT PERMISSION

"Synthetic Aperture Radar Data Compression and Feature Extraction"

BY

Abdelhakim El-Boustani

A Thesis/Practicum submitted to the Faculty of Graduate Studies of The University of Manitoba in partial fulfillment of the requirement of the degree

Of

DOCTOR OF PHILOSOPHY

Abstract

This thesis is concerned with developing new raw synthetic aperture radar (SAR) data compression schemes, as well as providing some processing techniques to extract features from the SAR images. The study involves neural networks, wavelets, wavelet packet, optimal wavelet, and multifractal analysis, with emphasis on quantization and bit allocation to compress such an SAR signal, and iterated function systems (IFS) to segment the SAR image.

A SAR system is a sophisticated remote sensing tool capable of producing high resolution images from a moving platform either in space or in the atmosphere. It offers the advantage over passive optical sensing of operating in either day or night and in all-weather. When such a radar is placed on board a satellite, compression of the raw SAR signal is necessary to reduce the large amount of collected data the downlink needs to transmit to a ground station within a restricted bandwidth. To this end, wavelets representations have proven to be very effective for signal compression, due to their time-frequency localization and their joint statistical regularities.

After a general presentation of SAR system and principles, this research investigates and implements methods for coding of raw SAR data which are based upon suitable transforms of the complex raw data. The Karhunen Loève Transform (KLT) is implemented with a three layers back-propagation neural network. Then, a compression of the raw SAR signal using five kinds of wavelets is presented: Haar wavelet, the Battle-Lemarié wavelets (linear and quadratic), and Daubechies wavelets (D4 and D20). A generalization to wavelet packet is also proposed. Experimental results point out advantages and drawbacks of this approach. Due to noise-like characteristics of the raw SAR signal, standard wavelets are not very efficient in compacting energy in the transform domain. We finish by developing an optimal wavelet for raw SAR data compression. The optimality criterion is redundancy minimization in the transform domain. Experimental results show that the optimal wavelet outperforms the standard wavelets and the present reference technique used to compress raw SAR data: the block adaptive quantization (BAQ).

Also, a multifractal-based approach to the extraction of textural features from SAR images is proposed. First, the Hölder exponents are estimated from the continuous wavelet transform of the image, then the singularity spectrum is computed. Each fractal component consisting of pixels having the same Hölder exponent can be an attractor of an IFS. The spectrum at each point is used as input for the K-means classifier. The theory and the algorithms for this segmentation approach are presented. Experimental results show that the approach is beneficial for SAR image segmentation, demonstrating better segmentation than those obtained by other techniques.

Acknowledgements

To begin, I would like to thank Professor W. Kinsner for agreeing to be my thesis advisor, and for providing me with the topic of this thesis. His support, encouragement and suggestions guided me during the course of my research. Dr. Kinsner was available when I needed him and I am very grateful for his support. His editorial suggestions for this thesis very much improved the manuscript. I would also like to thank Professor D. Gingras for agreeing to be the external examiner for this thesis. My thanks also go to Professor E. Shwedyk for the time he provided me and the useful discussions we had with him. I learned a lot from him, especially in applying mathematics to Engineering. I would like to thank the committee members Professor P. Aichison and Professor H. Soliman for agreeing to be on the committee and for their valuable comments.

My thanks go also to the Alaska SAR facilities for providing the data used in this thesis as well as the processing software. Special thanks go also to Dr. Isabelle Herlin, Director of AIR Project at INRIA in Rocquencourt, France for accepting me as a visiting student with her group.

This thesis would not have been possible without the financial support provided by the University of Manitoba, Telecommunication Research Laboratories (TRLabs) and the Natural Sciences and Engineering Research Council (NSERC) of Canada. To each of them, I say thank you.

During the course of my thesis, I had the opportunity to collaborate with two talented engineers from Dr. Kinsner's research group; Kalen Brunham and Sharjeel Siddiqui. I would like to thank and acknowledge both of them for their help during this research. My thanks also go to the other members of the research group with whom I had many useful discussions, including; Bin Huang, Richard Dansereau, Robert Barry, Michael Potter, Stephen Dueck, Aram Faghfouri, Neil Gadhok, and Leila Safavian.

Finally, I would like to thank my wife, Florence, for her continuous support. I would like to dedicate this work to her as well as to our children Sarah and Yannis.

TABLE OF CONTENTS

LIST OF FIGURES

Page

LIST OF TABLES

LIST OF ABBREVIATIONS AND ACRONYMS

1-D	one dimensional
2-D	two dimensional
A/D	analog to digital converter
ASF	Alaska SAR facility
BAQ	block adaptive quantization
BPN	backpropagation network
bps	bits per sample
CWT	continuous wavelet transform
DA	deterministic algorithm
Dn	Daubechies wavelet with n vanishing moments
DCT	discrete cosine transform
DWT	discrete wavelet transform
ERS	european remote sensing satellite
FBAQ	flexible block adaptive quantization
FPBAQ	floating point block adaptive quantization
FFT	fast Fourier transform
ICWT	inverse continuous wavelet transform
IFS	iterated function system
iid	independent and identically distributed
KLT	Karhunen-Loève transform
LBG	Linde Buzo Gray (algorithm)
LR	likelihood ratio
MA	multifractal analysis
MMSE	minimum mean square error
MRA	multiresolution analysis
MSD	multiresolution signal decomposition
MSE	mean squared error

MSM	most singular manifold
NN	neural network
OWT	optimal wavelet transform
PCA	principal component analysis
PDF	probability density function
PNN	probabilistic neural network
PRF	pulse repetition frequency
PSNQR	peak signal to quantization ratio
Radar	radio detection and ranging
RIA	random iteration algorithm
ROA	ratio of averages
ROEWA	ratio of exponentially weighted averages
SAR	synthetic aperture radar
SLRAR	side-looking real aperture radar
SNR	signal-to-noise ratio
SQNR	signal to quantization noise ration
vel	volume element
VQ	vector quantization
WFT	windowed fourier transform
WPT	wavelet packet transform

List of Symbols

δ_a	Azimuth resolution
δ_D	Resolution of Doppler frequency measurement
δ_g	Ground range resolution using pulse compression
δ_s	Slant range resolution
τ_p	Time duration of radar pulse
θ	Incidence angle
$\theta(q)$	Scaling exponent
θ_r	Vertical radar beamwidth
ϕ_k	Elementary phasor phase delay
$\phi(t)$	Scaling function
λ	Radar beam wavelength
μ^s	Hausdorff measure
$\psi(t)$	Mother wavelet
$\Psi(\omega)$	Fourier transform of $\psi(t)$
Δ	Quantization step
σ_D^2	Mean squared quantization error
σ_x^2	Variance of x
A_j	Approximation signal of $f[x]$ at resolution j
a_n^j	n th approximation coefficient at resolution j
B	Frequency bandwidth of transmitted pulse
b_i	Quantizer boundary
c	Speed of light in vacuum
C	Cantor set
D	Distortion due to quantization
D_{BC}	Box counting dimension
D_C	Capacity dimension
D_H	Hausdorff dimension
$D(h)$	Singularity spectrum
D_j	Detail signal of $f[x]$ at resolution j
d_n^j	n th detail coefficient at resolution j
D_q	Rényi dimension spectrum

D_S	Similarity dimension
$D(x, y_i)$	Distortion metric for quantization of x to y_i
$E[X]$	Expectation of X
f_D	Doppler frequency
$\tilde{f}(m, n)$	Wavelet coefficients
f_{prf}	Pulse repetition frequency
f_s	Sampling frequency
f_r	Radar pulse frequency
$f_x(x)$	Probability density function of x
H	Altitude of radar platform
H_1	First order entropy
H_q	Rényi entropy
$h(x)$	Hölder exponents at point x
L_a	Antenna length
L_g	Antenna height
$L^2(\Re)$	Vector space of all square integrable real valued functions
R	Distance to target in range
$\Re$	Set of all real numbers
$R(D)$	Rate-distortion function
R_k	Number of bits assigned to k th coefficient
R_m	Distance in range to mid-swath
R_s	Distance to target in slant range
t_{ipp}	Inter-pulse period
t_R	Round trip pulse time
V_i	Quantization region of vector quantizer
V_j	Approximation space at resolution j
V_s	Speed of radar platform relative to the surface
W_a	Extent of radar beam footprint in azimuth
W_g	Ground range swath width
W_j	Detail space at resolution j
W_r	Slant range swath width
y_i	Quantizer reconstruction value
$\mathbf{Z}$	Set of all integers

CHAPTER I

INTRODUCTION

1.1 Background and Motivation

Synthetic Aperture Radar (SAR) is a sophisticated remote sensing tool that is capable of providing high resolution images from a moving platform. It presents the advantage over optical sensing of operating day or night and in all-weather. Although the SAR system is used today for non-imaging applications, it was originally developed as an imaging radar. The image generation process can be broken up into three basic stages: (i) sensing of the target area using the imaging radar, (ii) digitization and compression of the reflected SAR signal for archiving or downlink to a ground station, and (iii) processing of the reconstructed SAR signal into image data, as illustrated in Fig 1.1. This thesis will focus primarily on compressing the digitized reflected raw SAR signal for transmission from a satellite down to a ground station, namely downlinking as much information as possible within the bandwidth constraints in order to fit the data stream into the available communication channel on the satellite. This digitized reflected SAR signal is known as raw SAR data. The SAR images are also investigated for feature extraction to improve the raw SAR data compression.

In imaging radars like SAR, the length of the radar antenna determines the resolution in the azimuth (along-track) direction of the resulting image, thus the longer the antenna, the finer the resolution in this dimension. As it is prohibitively expensive to place a very large radar antenna in space, an alternative approach is to synthesize the aperture. In

SAR, the radar sends out many pulses very rapidly as it travels over a particular object, and captures the backscattered responses. The ability of the radar antenna to receive many backscattered responses per object, as it moves along its flight track, allows the radar to synthesize a very long antenna.

Since a high resolution radar can produce hundreds of megabits of data per second, a trade-off between the resolution and the bandwidth allocated to the downlink channel should exist. As radar technology advances and user demands for quality increase, current raw SAR data compression techniques will encounter serious limitations. To ensure that future imaging radars can convey the highest resolution possible, improvements in raw SAR data compression techniques are necessary.

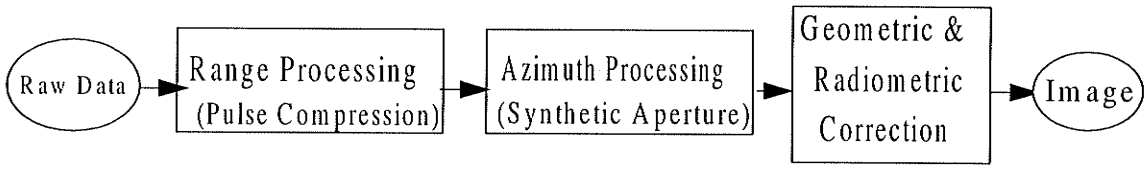

Fig. 1.1 SAR processor.

The necessity for raw SAR data compression can be best understood by simply examining the Nyquist sampling frequency of the radar returns. If we consider the Canadian spaceborne SAR system, Radarsat-1, which has a minimum pulse bandwidth of B_R = 11.6 MHz, the Nyquist theorem then dictates that the minimum sampling frequency is 23.2 MHz, which results in an instantaneous bandwidth of 185.6 Mbps when quantized using an 8-bit *analog-to-digital* (A/D) converter. This data must then be transmitted in Radarsat-1's bandlimited channel of 105 Mbps. Clearly, compression factor of 2 is necessary. Currently, the most widely used raw SAR data compression technique is

the *block adaptive quantization* (BAQ) [KwJo89] first developed by the NASA Jet Propulsion Laboratory (JPL). The BAQ algorithm is, however, not an optimal algorithm as it results in a low *signal to quantization noise ratio* (SQNR) compared to the theoretical Shannon bound. With new higher resolution radars currently in development, compression techniques with low SQNR could preclude the advancements of SAR.

As any compression technique is application dependent, this thesis investigates the segmented SAR image. This allows for further evaluation of the used raw SAR signal compression technique and provides new feedback to improve it for future compression of similar terrain. SAR provides a high-resolution imagery, which is principally used for terrain classification. The wide range of textures observed in SAR images makes them difficult to analyze unless an efficient segmentation technique is applied in order to discriminate between these textures. The speckle phenomena on SAR images which results from coherent processing of radar echoes makes any segmentation of such images with classical methods very difficult. Also, the majority of SAR images contain only naturally occurring terrain. With the SAR resolution, even the man-made objects can be seen as textural information in the SAR image. Hence texture analysis and segmentation of SAR images can be better handled by fractal geometry rather than the Euclidean geometry. Different studies have established that there is a correlation between decreasing fractal dimension of SAR data and microwave backscatter from special objects, which help interpret SAR images [TuBA98]. Fractal characterization, however, is very limited in detecting local regularities in images. In contrast, multifractal analysis has been applied in image analysis and classification and proven to be important in texture analysis [DuYe02], [VGBF03].

1.2 Objectives and Goals

The purpose of this thesis is twofold: (i) developing new techniques for raw SAR data compression, and (ii) developing image processing techniques for statistical features extraction. The primary research questions addressed in this thesis are:

1. How to condition raw SAR signals for compression;
2. What is the contribution of neural network for compressing SAR signals;
3. How can a 2-dimensional (2-D) discrete wavelet transform (DWT) compression technique be used in the compression of raw SAR data using a standard wavelet basis function, and what are the advantages and drawbacks of this approach;
4. Which standard wavelet basis function gives the best signal to quantization noise ratio (SQNR) in the compression of raw SAR data using the 1-D DWT compression technique;
5. How to determine an optimal wavelet able to minimize the redundancy in the transform domain;
6. How to extend the optimality formalism to the wavelet packet case and what is the advantage of this approach; and
7. How the fractality character of SAR images can be used to extract features.

This thesis develops new and promising approaches for SAR data compression and segmentation based on neural networks, wavelets and multifractal analysis. It shows how to adapt and to apply these modern techniques with a maximum benefit for SAR data compression and feature extraction. By using wavelets, the thesis points out the

limitations of the standard bases, and determines a wavelet basis adapted to the SAR signal. This thesis develops also an algorithm for SAR image segmentation using a combination of multifractal analysis and the *iterated function systems* (IFSs).

1.3 Organization

The organization of this paper follows the temporal development of the thesis research. Thus, a background on SAR system is provided in Ch. 2, followed by an extensive literature review of the current raw SAR data compression techniques in Ch. 3. Chapters 4 and 5 present the development of wavelet, wavelet packet and optimal wavelet for raw SAR data compression. The multifractal analysis and its application to SAR image segmentation are provided in Chapters 6 and 7. Chapter 8 provides conclusions. A brief description of each chapter content follows.

Chapter 2 explains the physics of SAR and the SAR signal processing algorithms. Pulse compression and azimuth focusing are developed. Then SAR image formation and characteristics are presented. Since the raw SAR signal is central to this thesis, a discussion of its nature, statistics and other characteristics are provided in this chapter. Since the original 8-bit sampled data on the satellites are not available to the general public, Ch. 2 also presents a discussion on transforming the available reduced 4 and 5-bit per sample SAR data to 8-bit for experimental use. This makes also a lossy compression technique less severe. The details of the pre-conditioning of data test sets used in this thesis are presented in the last section of the chapter. The contributions include a comprehensive bibliographical study as well as the pre-processing of data in hand.

Chapter 3 begins by discussing a mathematical model of images, then states the notations and fixes the hypothesis of work. Then background information on recent developments on quantization is provided, followed by a discussion of current raw SAR data compression techniques. This chapter demonstrates that currently, even the best techniques are either still quite far from the theoretical Shannon bound, or are prohibitively complex for implementation on a satellite. The main contribution in this chapter is presented at the end and consists of a new compression scheme using a three layer back-propagation neural network.

Chapter 4 provides the wavelet transform of signals. Both continuous and discrete transforms are presented. The relationship to the filter banks, thanks to the multiresolution analysis, is described. Then a compression of the raw SAR data using standard wavelets is developed. This work, done in collaboration with INRIA, Rocquencourt, France, point out advantages and drawbacks of the approach. Several design parameters are discussed, including the choice of wavelet basis function over 100 standard wavelet bases. Specific contributions in this chapter include a unified presentation of wavelets and their adaptation and application to raw SAR signal compression.

Chapter 5 reviews the wavelet optimality developed in the literature and presents a formalism in order to determine an optimal wavelet able to minimize the redundancy in the transform domain. Application to raw SAR signal compression is described. Therefore, the wavelet packet tree is investigated and applied to the compression of raw SAR signal. Extension of the optimal formalism to the case of wavelet packet is also described. Wavelet adaptation to raw SAR signal is our contribution in this chapter.

Chapter 6 presents the necessary background on fractals, multifractals and iterated function systems. After overviewing fractal objects and dimensions, we emphasize the mathematical formalism behind multifractal measures and singularity spectrum as described in Sec. 7.3. It is shown how signal local regularities can be measured by the Hölder exponent and how to estimate this exponent by the mean of wavelet transform. The chapter ends by a presentation of IFS encoding and decoding algorithms. An extensive bibliographical research leading to a unified presentation is the resultant contribution.

Chapter 7 proposes a multifractal-based approach to the extraction of textural features from SAR images. The Hölder exponents are estimated first from the continuous wavelet transform of the image, as well as the corresponding Rényi dimension spectrum. Next, an algorithm for the segmentation of SAR images based on the spectrum at each pixel is presented. Also, each fractal component consisting of pixels having the same Hölder exponent can be an attractor of an IFS. To highlight the edges, the K-means algorithm is used. The experimental results are presented and show that the approach is beneficial for SAR image segmentation. Specific contributions include algorithm design and experimental implementation.

Chapter 8 gives conclusions, confirms and summarizes the contributions of this thesis, and outlines recommendations for future research.

CHAPTER II

SYNTHETIC APERTURE RADAR

Radar systems present an advantage over optical sensing by using microwave illumination which makes them operational during day or night and in all-weather. However, conventional radars have the disavantage in that they can hardly reach the level of optical resolutions. In fact, the resolution in both cases is proportional to the antenna length and inversely proportional to the wavelength of the illumination source. Since the wavelengths of microwaves are much longer than those of visible light and the use of a long antenna is impracticable, a technique called *Synthetic Aperture Radar* (SAR) was developed and is capable of providing optical resolutions.

This chapter presents the general principles of SAR. Section 2.1 presents the conventional radar systems and develops the pulse compression technique. Then, azimuth processing, which is the core of the SAR technique is presented in Sec. 2.2. The raw SAR signal, our primary interest in this thesis, is derived in Sec. 2.3. Section 2.4 discusses the SAR image formation and characteristics, and finally data are presented in Sec. 2.5. Most of the material presented in this chapter can be found in [Brow67], [Brun02], [Cook60], [CuMc91], [EBJW82], [Kova76], [Lebe95], [MuVi89], [OlQu98], [Skol70], [Touz88].

2.1 Radar

The purpose of radar (RAdio Detection And Ranging) is the detection of targets and the extraction of information related to their speed, their distance from the radar, their

sizes, by measuring the strength and round-trip time of the microwave signals that are emitted by the radar antenna and reflected from these objects.

The radar antenna transmits a pulse $S(t)$ at a particular wavelength λ (in the range 1 cm to 1 m, which corresponds to a frequency range of about 300 MHz to 30 GHz) and receives a phase shifted signal $D(t)$ generally contamined by white noise $N(t)$. Thus the signal available for processing is

$$D_n(t) = D(t) + N(t) \tag{2.1}$$

if a target is present and

$$D_n(t) = N(t) \tag{2.2}$$

if a target is absent. The impulse response $H(t)$ which maximizes the signal-to-noise ratio is given by (matched filter) [Tree71]

$$H(t) = S^*(-t) \tag{2.3}$$

The matched filter realizes not only an enhancement of the detectability but also achieves a high resolution in the range dimension by using the linear frequency modulation (LFM), or "chirp", with a pulse duration *(pulse width)* τ_p (of typically 10-50 microseconds (μs))

$$S(t) = rect\left(\frac{t}{\tau_p}\right)\cos 2\pi\left(f_0 t + \frac{Kt^2}{2}\right) \tag{2.4}$$

Where f_0 is the carrier frequency and K is called the chirp rate.

2.1.1 Side-looking Radar Acquisition

Figure 2.1 presents the scanning configuration of a side-looking radar. The radar is moving perpendicularly (this is strip map mode, other modes can be considered like squint imaging mode or spotlight) to the flight path, at speed V_s and at constant altitude H. While the platform is moving, the antenna illuminates an Earth's area called *swath.* At any fixed time the illuminated area is an ellipsoid (beam footprint) contained in a rectangle with dimensions $W_a \times W_g$, where a denotes the *azimuth* (the parallel to the direction of travel) and g denotes the ground swath width (or *range*). These lengths are related to the dimensions of the antenna $L_a \times L_g$, the spread of the radar pulse β_a and β_g in the azimuth and range directions, respectively, and the radar's look angle θ at the center of the beam by

$$W_a = \beta_a \times \frac{H}{\cos\theta} \tag{2.5}$$

$$W_g = \beta_g \times \frac{H}{\cos^2\theta} \text{ (since } W_g \times \cos\theta \text{ can be approximated by } \beta_g \times \frac{H}{\cos\theta}) \tag{2.6}$$

2.1.2 Radar Resolution

In ground imaging radars, spatial resolution is the minimum distance of two point targets that can be distinguished as separate in the image. The resolution of interest is the ground range resolution and the azimuth resolution. The need for fine azimuth resolution relates to the development of the synthetic aperture radar (SAR) as we will see in the sequel. Finer range resolution is obtained by using LFM pulse compression.

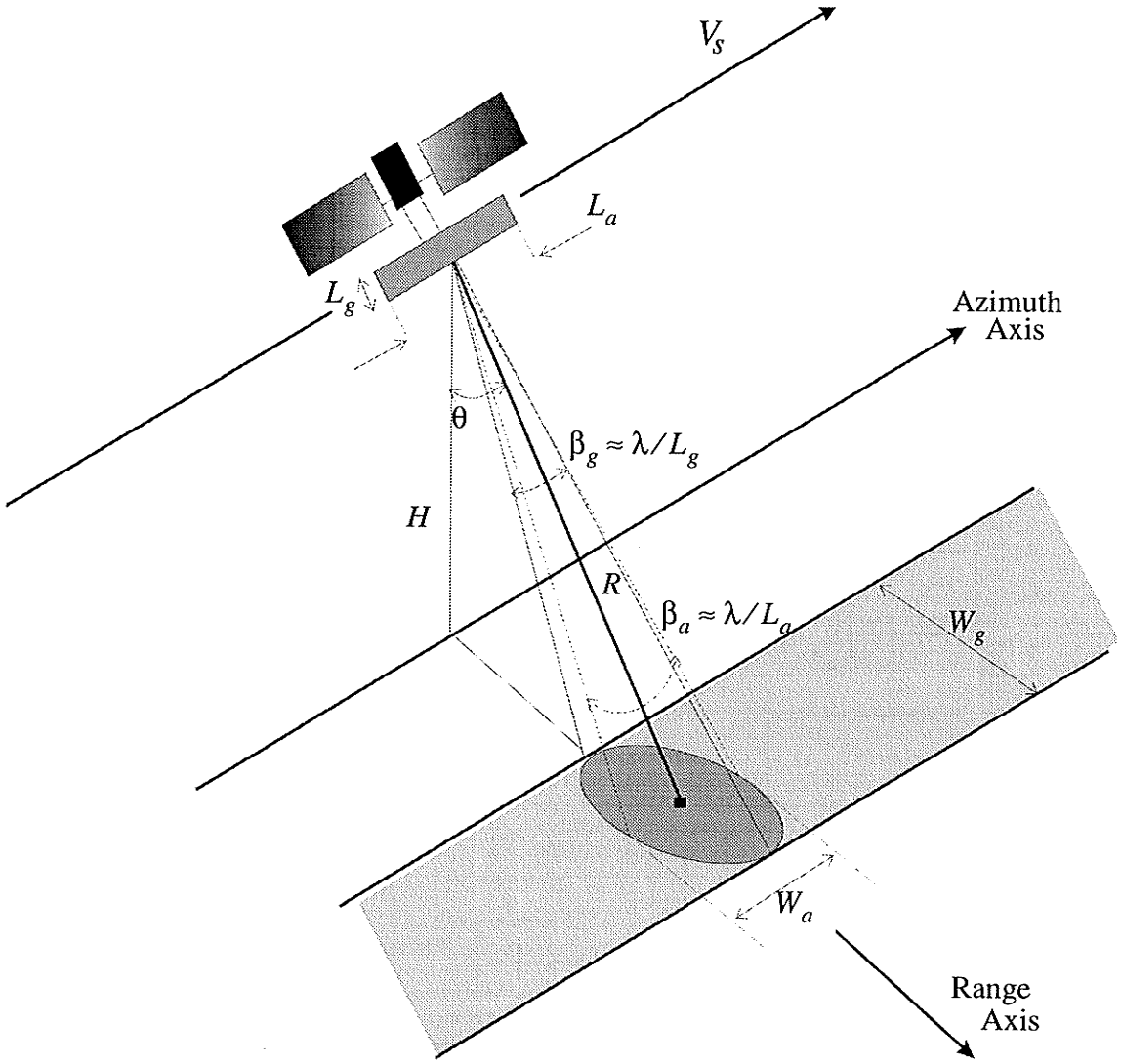

Fig. 2.1 Configuration of a spaceborne side-looking radar.

Azimuth Resolution

The azimuth resolution is defined as the minimum separation of two targets in azimuth that can be distinguished as separate by the system. Two such targets on the ground at the same slant range R can only be distinguished if they are not both in the radar beam at the same time. The azimuth resolution W_a at a slant range R is then given by

$$W_a = R\beta_a \tag{2.7}$$

and can be approximated by

$$W_a = R\left(\frac{\lambda}{L_a}\right) \tag{2.8}$$

where λ is the wavelength of the RF signal.

Equation 2.8 is very similar to the resolution in optics, and this equation demonstrates that the azimuth resolution of a real aperture radar (RAR) is inversly proportional to the antenna length. Thus, the azimuth resolution can be improved by simply increasing the antenna length. Unfortunately, this is not a possibility in all cases due to the mechanical problems involved in constructing a precise antenna with an L_a/λ ratio greater than a few hundred [CuMc91]. The alternative is the SAR technique which uses successive transmit pulses to synthesize a long antenna array by moving a small physical antenna. This technique will be investigated in detail in Sec. 2.2.

Ground Range Resolution

The slant range resolution δ_s of the radar defines the minimum slant range separation of two points that can be distinguished as separate by the system. As shown in Fig. 2.2, the two point targets A and B are distinguishable, but there is no clear distinction between where C ends and D begins. In fact, if the head of an echo pulse arrives at the antenna at time $t > 0$ after the tail of the previous echo pulse, then they can be distinguished by the system as separate. Therefore, for two targets to be distinguished,

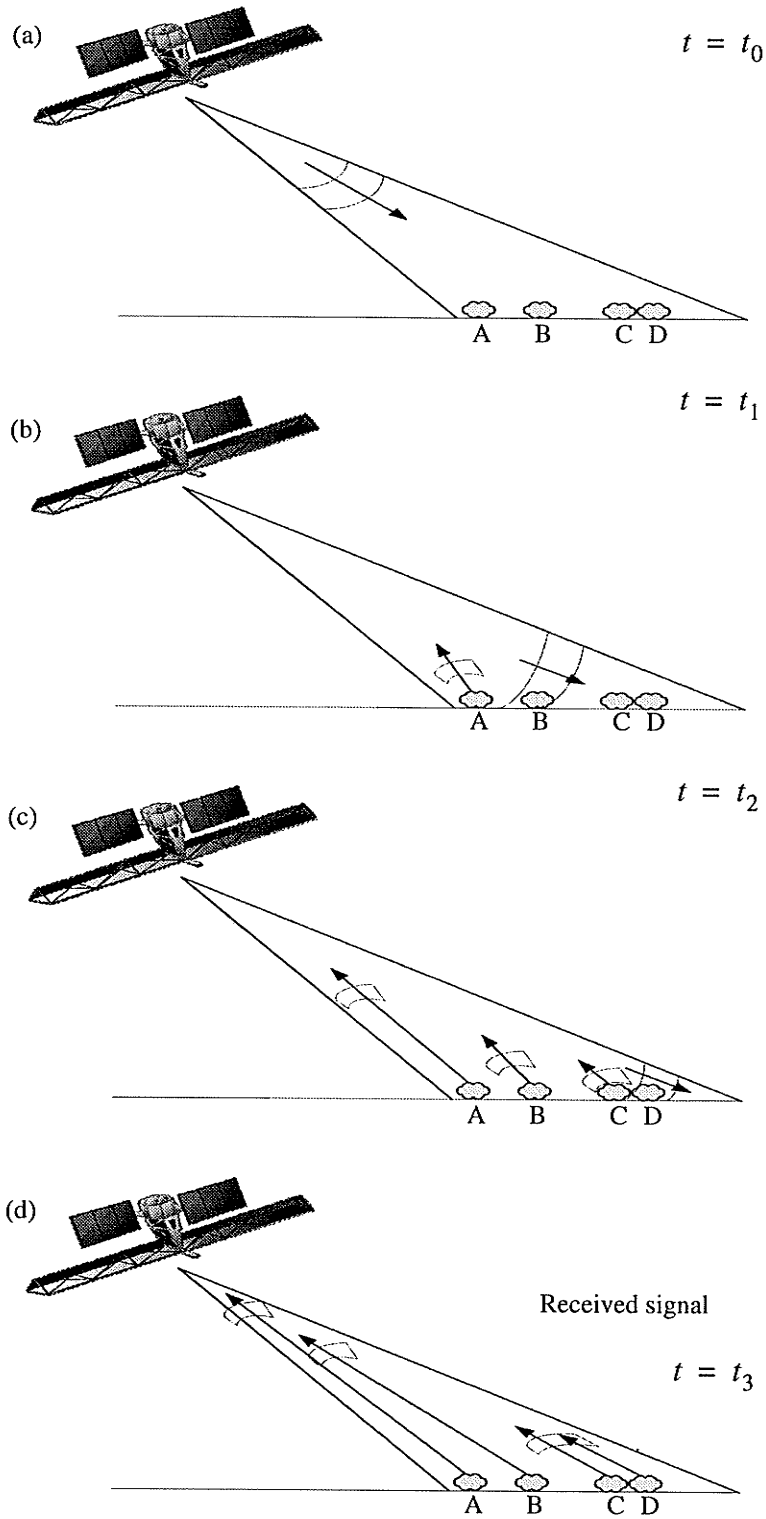

Fig. 2.2 Propagation of a radar pulse and separation of the echoes (after [Lebe95]). (a) The radar radiates a pulse. (b) The pulse hits the target A and an echo is reflected. (c) An echo is reflected from target B and the pulse interacts with targets C and D. (d) An echo from targets C and D is reflected.

they should be separated by at least the pulse duration, τ_p, or equivalently, the slant range resolution

$$\delta_s = \frac{c\tau_p}{2} \tag{2.9}$$

where c is the speed of light.

Targets are located on the ground and it is more interesting to find the minimum ground range separation of two points that can be distinguished as separate by the system, called the ground range resolution. Figure 2.2 shows that, to be resolved, the targets have to be separated further (by a factor of $1/(\sin\eta)$, where η is the incidence angle) . In the considered side-looking configuration, the incidence angle is the same as the look angle θ and the ground range resolution can then be approximated by

$$\delta_g = \frac{c\tau_p}{2\sin\theta} \tag{2.10}$$

Equation 2.10 shows that the ground range resolution is determined by the geometry of the radar and the radar pulse duration, but it is independent of the radar-target distance. The pulse compression technique presented in the following section allows a finer resolution while, independently, keeping an important radar-target distance.

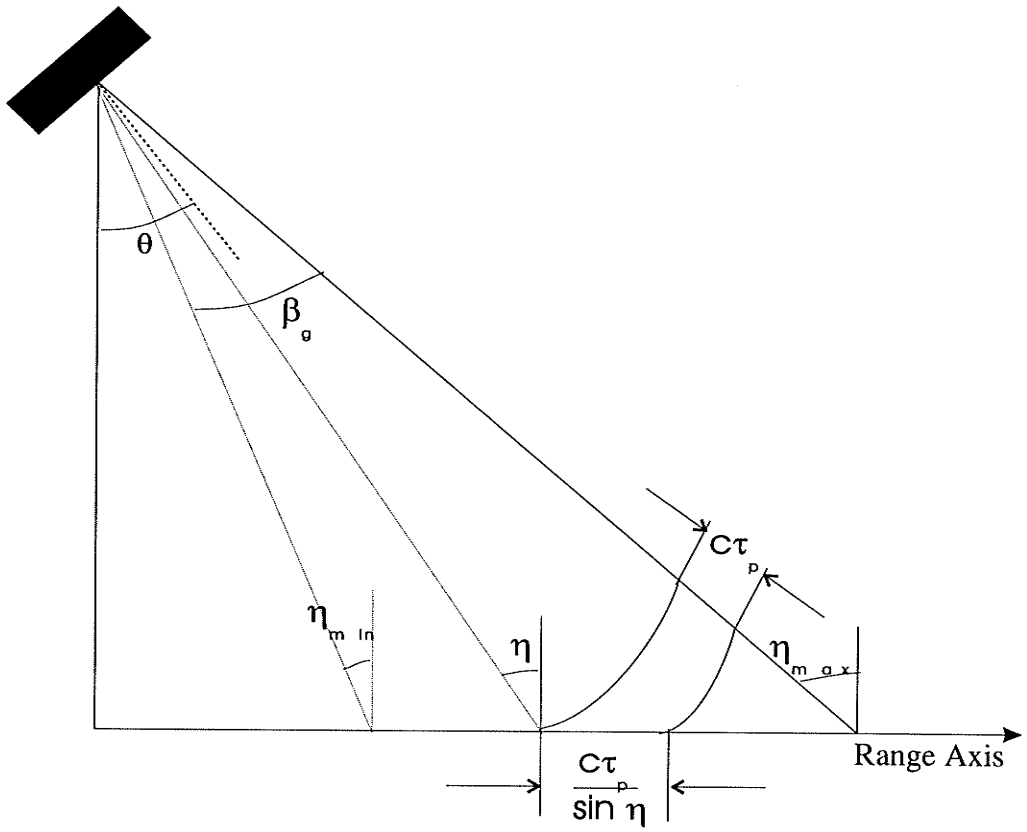

Fig. 2.3 Ground range resolution vs slant range resolution [CuMc91].

2.1.3 Pulse Compression

At the Earth's surface, the energy in the radar pulse is scattered in all directions, with some reflected back toward the antenna. This backscatter returns to the radar as a weaker radar echo and is received by the antenna only if it has enough energy to be detectable. However, as the energy contained within a pulse is increased so is the pulse duration τ_p. Therefore, the requirement for a fine ground range resolution conflicts with the requirement for reliable detection. To achieve a combination of both requirements, one uses the pulse compression technique, which consists of transmitting long radar pulses

with duration T coded in a way that it is possible at the reception to reduce this time to a smaller value τ.

The transmitted waveform is a signal chirp and when it is compressed, the resultant pulsewidth is approximatly equal to the reciprocal of the radar bandwidth B

$$\tau = \frac{1}{B} \tag{2.11}$$

The ground range resolution is then improved by a factor equal to the ratio of the transmitted to compressed pulsewidth

$$\frac{T}{\tau} = BT \text{ (also called time-bandwidth product)} \tag{2.12}$$

To see how Eq. 2.11 can be derived, consider the complex form of the LFM signal given in Eq. 2.4

$$S(t) = rect\left(\frac{t}{T}\right)\exp\left\{2\pi i\left(f_0 t + \frac{Kt^2}{2}\right)\right\} \tag{2.13}$$

The bandwidth of this signal is then $B = KT$. After stripping off the carrier frequency and performing a correlation with the matched filter, the shape of the detected signal, in absence of noise is

$$U(t) = (T-|t|)\sin c(Kt[T-|t|])rect\left(\frac{t}{T}\right) \tag{2.14}$$

where $\sin c(x) = (\sin \pi x)/(\pi x)$. The first positive zero of $U(t)$ is given by

$$\tau = \frac{T}{2}\left(1 - \sqrt{1 - \frac{4}{BT}}\right) \tag{2.15}$$

and for a large time-bandwidth product BT, a good approximation is $\tau = 1/B$, which is Eq. 2.11.

2.2 Synthetic Aperature Radar: Azimuth Focusing

We have seen that the azimuth resolution is proportional to the distance radar-target R and inversely proportional to the antenna length L_a (Eq. 2.8). To achieve fine azimuth resolution at long ranges, radars with small physical antennas employ SAR processing. This is illustrated in Fig. 2.4.

While the radar is moving in space, it transmits a train of radar pulses at intervals determined by f_{prf}, the *pulse repetition frequency* (PRF) (about 1500 high- power pulses per second are transmitted toward the target or imaging area). Between successive pulses, the radar platform moves a distance of V_s/f_{prf}, which is often much less than the azimuth extent of the beam footprint W_a. Because of this small platform displacement, the point targets in the radar beam footprint are hit by many different pulses from the radar. SAR processing is then achieved by summing all the radar returns to form an azimuth beam which is governed by the length of the synthesized array and not the length of the physical antenna.

The key observation that ultimately allows for fine azimuth resolution with a manageable antenna length appears in the work of Carl Wiley of the Goodyear Aircraft

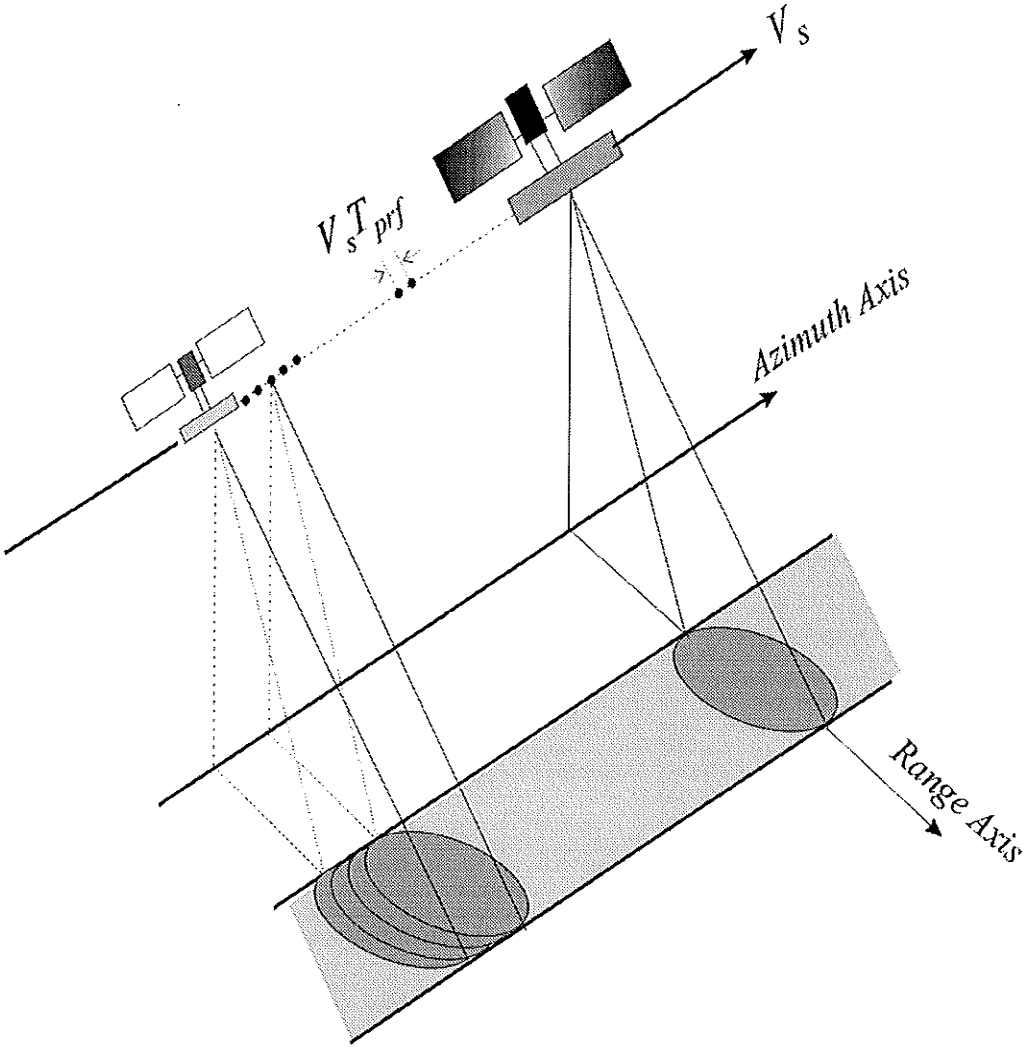

Fig. 2.4 Synthetic aperture principle

Corporation in the early 1950s [ShRR62]. Wiley observed that a one-to-one correspondance exists between the azimuth coordinate of a reflecting object being linearly traversed by a radar beam, and the instantaneous Doppler shift of the signal reflected to the radar by that object. He concluded that a frequency analysis of the reflected signals could enable finer azimuth resolution than that permitted by the along-track width of the physical beam itself.

Consider the radar echoes for an isolated point target as shown in Fig. 2.5. When the radar, travelling parallel to the point target with velocity V_s, reaches x_1, the point target is illuminated by the radar beam. This point target continues to be illuminated until the radar reaches x_2, travelling a distance $L_s \approx \beta_a r_0$ equal to the length of the synthetic antenna. When the radar platform is at position x, the corresponding slant range $r(x)$ to the point target is given by

$$r(x) = \sqrt{r_0^2 + x^2} \tag{2.16}$$

As x is very small with respect to r_0, the change in slant range $\Delta r(x)$ to the target is then approximately

$$\Delta r(x) \approx \frac{x^2}{2r_0} \tag{2.17}$$

The phase change $\phi(x)$ corresponding to a change in slant range $\Delta r(x)$ as a function of radar position x is given by the quadratic function

$$\Delta\phi(x) \approx \frac{2\pi x^2}{\lambda r_0} \tag{2.18}$$

Assuming a constant velocity V_s for the radar platform and substituting the displacement x with $V_s t$, the phase change as a function of time is

$$\Delta\phi(t) = \frac{2\pi V_s^2 t^2}{\lambda r_0} \tag{2.19}$$

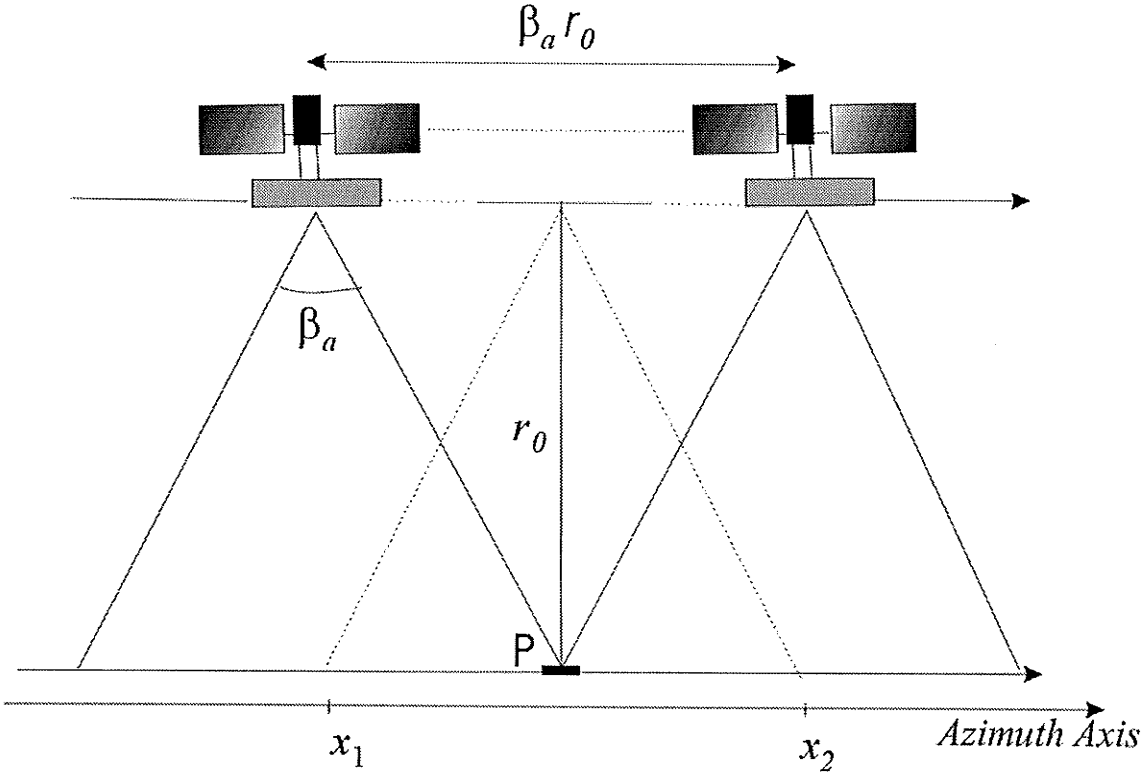

Fig. 2.5 Radar-target geometry (after [Tomi78]).

As a time rate of change in Eq. 2.19 causes a frequency shift, the Doppler frequency f_D, calculated by taking the first derivative of Eq. 2.19, is given by

$$f_D = \frac{1}{2\pi}\frac{d(\Delta\phi(t))}{dt} = \frac{2V_s^2 t}{\lambda r_0} \tag{2.20}$$

Therefore, if the received signal is frequency analyzed at time t, any energy observed in the return at a time t corresponding to a slant range r and at Doppler frequency f_{D_1} will be associated with a target at coordinate $x = \frac{\lambda r_0 f_D}{2V_s}$. Similarly, energy at a different

Doppler frequency f_D will be assigned to a corresponding coordinate x'. This allows targets to be discriminated even though they are in the radar beam at the same time.

For $t = T_s$, the time of synthetic aperture, the corresponding bandwidth B_a of the signal is

$$B_a = \frac{2V_s^2 T_s}{\lambda r_0} \tag{2.21a}$$

but $T_s = L_s/V_s$, $L_s \approx \beta_a r_0$ and $\beta_a = \lambda/L_a$; therefore

$$B_a = \frac{2V_s}{L_a} \tag{2.21b}$$

Similarly to the pulse compression technique, the time resolution in the azimuth direction after processing is $1/B_a$, and it corresponds to the following spatial azimuth resolution

$$\delta_a = \frac{V_s}{B_a} = \frac{L_a}{2} \tag{2.22}$$

as shown by Cutrona *et al.* [CVLH61], [CuHa62]. Equation 2.22 presents the counter-intuitive result that arbitrarily fine azimuth resolution is obtainable by reducing the antenna length. However, this assumes that the synthetic antenna length is equal to the distance across the radar beam at each range line, which is not always valid [CuMc91].

The data are sampled in the azimuth direction with a frequency equal to f_{prf} and the Nyquist condition means that this frequency must exceed the bandwidth B_a. This gives a lower bound to the antenna length $L_a \geq \frac{2V_s}{f_{prf}}$.

More generally, a requirement on the antenna area A is found [CuMc91] so that

$$A = L_a L_g > \frac{4V_S \lambda R_m (\tan\theta)}{c} \tag{2.23}$$

where R_m is the slant range from radar to mid swath.

2.3 Raw SAR Data

2.3.1 Raw Data

To determine in more detail the raw SAR signal, consider again the complex form of the signal emitted by the antenna $S(t) = A(t)e^{i\varphi(t)}$. Each target in a slant range r in the interval $[R_m - (W_g \tan\theta)/2, R_m + ((W_g \tan\theta)/2)]$, with a reflectance $e_0(r) = a(r)e^{i\xi(t)}$, contributes to the returns. Therefore, the backscattered signal is the sum of all the returns and is given by [Lebe94]

$$\tilde{D}(t) = \int_{(R_m - (W_g \tan\theta)/2)}^{(R_m + ((W_g \tan\theta)/2))} a(r) S\left(t - \frac{2r}{c}\right) e^{i\left[2\pi f_0\left(t - \frac{2r}{c}\right) + \xi(r)\right]} dr \tag{2.24}$$

After demodulation (carrier frequency removal), the raw SAR signal is obtained by

$$D(t) = \int_{(R_m - (W_g \tan\theta)/2)}^{(R_m + ((W_g \tan\theta)/2))} a(r) S\left(t - \frac{2r}{c}\right) e^{i\left[\xi(r) - 2\left(\frac{2\pi}{\lambda}\right)\right]} dr \qquad (2.25)$$

This continuous time raw signal representing the return for some particular pulse is then sampled and stocked in a line of an array. Each column (the block corresponding to the aperture time) of the array represents the returns from a target for different pulses as shown in Fig. 2.6.

As stated before, the signal is, by the SAR principle, sampled automatically in the azimuth direction. The sampling frequency is simply the pulse frequency repetition f_{prf}. In the range direction, the A/D converter must obey the Nyquist condition to avoid aliasing. In general, the sampling frequency is greater than the Nyquist frequency by a factor of 0.2 ($f_s \approx 2[1.2B]$, B is the pulse bandwidth and 2 is because of the complex nature of the signal). For example, in the Seasat case, B = 19 MHz, while f_s = 11.38 MHz.

2.3.2 Statistical Characterestics

To better understand the statistical proprties of the raw SAR signal presented as a 2-D array in the previous section, Eq. 2.25 is discretized and transformed to spatial coordinates. As seen before, the backscatter returns from a synthetic aperture radar instrument can be modeled as the superposition of N small scatters within the antenna beam footprint [KwJo89]. The coherent radar return $A(x,y)$ at observation point (x,y) (x for azimuth direction and y for range direction), is then given by

$$A(x, y) = |A|e^{i\theta} = \sum_{k=1}^{N} e(x_k, y_k)q(x - x_k, y - y_k) \tag{2.26}$$

where $e(x_k, y_k)$ is the reflectance amplitude of the elementary phasor k located at (x_k, y_k), and $q(x_k, y_k) = q_k e^{i\theta_k}$ is the transfer function depending only on the system but independent of e. Here, the complex amplitude e of the target k is given by $e(x_k, y_k) = a(x_k, y_k)e^{i\xi_k}$. The phase $\xi_k = \zeta_k + \varphi_k$ is the sum of the target phase ζ_k and the phase φ_k caused by the round-trip distance.

Since the elementary phasors are randomly placed in the resolution cell, the coherent sum in Eq. 2.26 can be interpreted as a random walk in the complex plane. Therefore, the randomly phased phasors can be assumed to have the following assumptions (Goodman conditions) [Good75]:

(1) The amplitude $a(x_k, y_k)$ (henceforth denoted by a_k for simplicity) and phase ξ_k of the kth elementary phasor are statistically independent of each other and of the amplitudes and phases of all other elementary phasors; and

(2) The phases ξ_k are uniformly distributed on the interval $[-\pi,\pi]$.

Assumption (2) is a result of the scatters having an unknown range and the range resolution of the SAR being much greater than the wavelength of the transmitted SAR signal. This produces the result that phase excursions of many times 2π radians produce a uniform distribution on the interval $[-\pi,\pi]$ [KwJo89]. These two properties allow the

determination of the statistical characteristics of the real and imaginary parts, along with the magnitude and phase, of the received SAR signal.

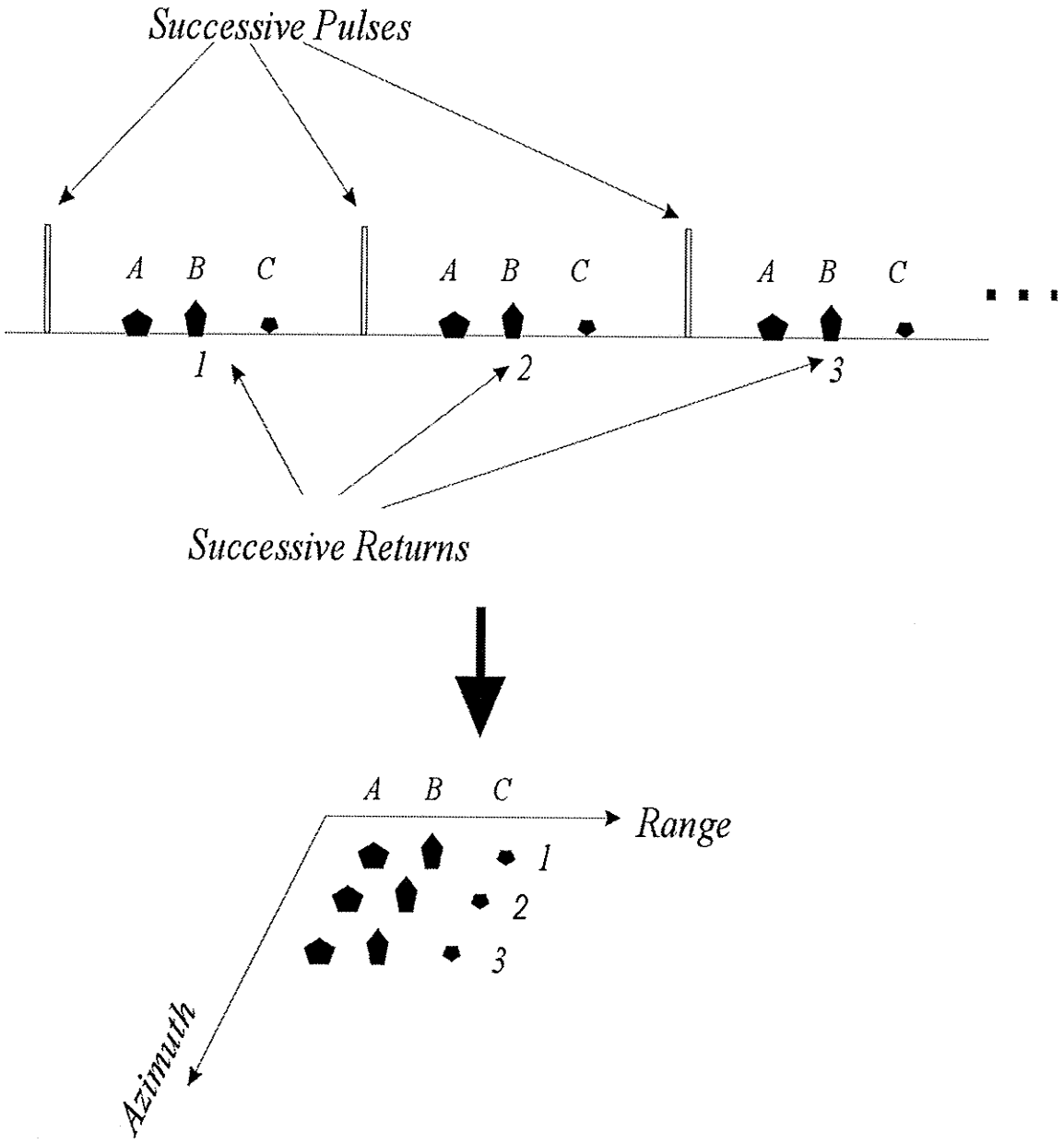

Fig. 2.6 Raw data collection.

Real and Imaginary Parts

The real (or *Inphase*) and imaginary (or *Quadrature*) parts of the received SAR signal are given by

$$I = \mathrm{Re}\{A\} = \sum_{k=1}^{N} a_k q_k \cos(\xi_k + \theta_k) \tag{2.27}$$

$$Q = \mathrm{Im}\{A\} = \sum_{k=1}^{N} a_k q_k \sin(\xi_k + \theta_k) \tag{2.28}$$

As q_k and θ_k are deterministic quantities, Assumption (1) guarantees that I and Q are sums of independent random variables. If we now suppose that the number N of elementary phasor contributions is very large, the central limit theorem implies that the real and imaginary parts of the received SAR signal are Gaussian. Thus, the distribution is completely determined by their means and their standard variations.

It is easy to see that Assumption (2) implies

$$E[\cos(\xi_k + \theta_k)] = E[\sin(\xi_k + \theta_k)] = 0 \tag{2.29}$$

The expected values of the real and imaginary parts of the received SAR signal is then also zero

$$\mathrm{E}[I] = E[Q] = 0 \tag{2.30}$$

Proceeding in a similar fashion, the variances of the real and imaginary parts of the received SAR signal are given by

$$\begin{aligned} \mathrm{E}[I^2] &= \sum_{k=1}^{N}\sum_{m=1}^{N} q_k q_m \mathrm{E}[a_k a_m]\mathrm{E}[\cos(\xi_k+\theta_k)\cos(\xi_m+\theta_m)] \\ &= \frac{1}{2}\sum_{k=1}^{N} q_k^2\ \mathrm{E}[a_k{}^2] \\ &= \sigma^2 \end{aligned} \tag{2.31}$$

$$\begin{aligned} \mathrm{E}[Q^2] &= \sum_{k=1}^{N}\sum_{m=1}^{N} q_k q_m \mathrm{E}[a_k a_m]\mathrm{E}[\sin(\xi_k+\theta_k)\sin(\xi_m+\theta_m)] \\ &= \frac{1}{2}\sum_{k=1}^{N} q_k^2\ \mathrm{E}[a_k{}^2] \\ &= \sigma^2 \end{aligned} \tag{2.32}$$

where we have used the fact that independent and uniformly distributed random variables X_k exhibit the expectations

$$\mathrm{E}[\cos X_k \cos X_m] = \mathrm{E}[\sin X_k \sin X_m] = \begin{cases} \frac{1}{2} & k = m \\ 0 & k \neq m \end{cases} \tag{2.33}$$

The covariance of the real and imaginary parts of the raw signal is obtained by

$$\begin{aligned} Cov(I, Q) = E[IQ] &= \sum_{k,m=1}^{N} q_k q_m \mathrm{E}[a_k a_m]\mathrm{E}[\cos(\xi_k+\theta_k)\sin(\xi_m+\theta_m)] \\ &= 0 \end{aligned} \tag{2.34}$$

Thus, the real and imaginary parts of the received SAR signal are independent, zero mean, identical variances, Gaussian distributed.

Magnitude and Phase

The magnitude $|A|$ and the phase ϕ of the received SAR signal are related to the real and imaginary parts of A by

$$|A| = \sqrt{I^2 + Q^2} \tag{2.35}$$

$$\phi = \arctan\frac{Q}{I} \tag{2.36}$$

Thus, $|A|$ is Rayleigh distributed, ϕ is uniformly distributed on $[-\pi,\pi]$, and they are independent.

2.4 Image Formation and Characteristics

Many applications of the contemporary SAR systems, such as physical oceanography measuring moving currents, moving target detection on the ground, digital mapping, and atmospheric changes, use only the raw SAR signal without any SAR image formation. However, other applications necessitate image formation. Once the raw SAR data have been received at the ground station, it must be processed to form the SAR image. The processing consists of correlating all Doppler components for ground targets. Originally, this processing was done using optical lenses [CLPU66], however, all current processing is done using numerical computers. The processor used in this thesis is the Alaska SAR Processor (ASP) from the Alaska SAR Facility (ASF) in Fairbanks Alaska.

Details about the ASP can be found in [Olms93]. In this process, the raw data is first range processed (pulse compression), then the SAR technique (azimuth processing) is applied. To obtain a good quality SAR image, a geometric and radiometric calibration must be performed. The processor assumes that the land is flat, the sensor and platform are stable and that the speed is constant. These assumptions are not realistic, which generates what is called geometric distortion. The other kind of distortion is radiometric distortion and arises from the system effects.

After calibration, each pixel in the radar image represents the radar backscatter for a related area on the ground (the pixel intensity is expressed in terms of the mean surface backscatter coefficient known as σ^0). Backscatter for a target area will vary for a variety of conditions: size of the scatterers in the target area, moisture content of the target area, polarization of the pulses, observation angles, and the pulses' wavelengths. The scattering aspects of the radar signals can be through either surface scattering or volume scattering and the return can be from transmission, reflection or scattering, or a combination of both making the SAR interpretation very complex.

2.4.1 SAR Image Characteristics

Since the raw SAR signal is a complex number, one can form either a complex image, image of the real part, the imaginary part image, the amplitude image, the phase image, the intensity image or the log intensity image. The intensity image $X = |A|^2$, $|A|$ given by Eq. 2.35, is the most commonly used.

Under Goodman conditions, $|A|$ is Rayleigh distributed and it follows that the intensity is exponentially distributed

$$P_X(x) = \frac{1}{\sigma} e^{\frac{-x}{\sigma}} \text{ if } x \geq 0, 0 \text{ otherwise} \tag{2.37}$$

(Other statistical models were developed for the intensity images such as Weibull distribution, log normal or K distribution [OlQu98], [SMTH83]).

As in sonar and ultrasound, the SAR image is formed from the return of coherent signals which may cause a random aspect on the extended homogeneous targets of the image known as *speckle*. The presence of speckle leads to the following multiplicative model

$$X = RS \tag{2.38}$$

where S denotes the speckle and R is the ground reflectivity.

Due to speckle, the ground reflectivity cannot be correctly estimated from a single pixel. This suggests the multi-look approach: incoherently averaging L images of the same area. This leads to the gamma distribution for the intensity

$$P_X(x) = \frac{1}{\Gamma(L)} \left(\frac{L}{\sigma}\right)^L x^{L-1} e^{-(Lx)/\sigma} \text{ if } x \geq 0, 0 \text{ otherwise} \tag{2.39}$$

Speckle Reduction

Since speckle poses many problems in detection and classification of SAR images, its removal is still a major issue in SAR image processing. Several filtering techniques, using either a heuristic approach or statistical adaptive approaches, have been developed.

Recently, wavelet transform combined with classical approaches were used and gave promising results [FoBB01], [Fouc00], [Touz99].

2.4.2 The Fractal Nature of SAR Images

The majority of SAR images contain only naturally occurring terrain. With the SAR resolution, even the man-made objects can be seen as textural information in the SAR image. Hence texture analysis and segmentation of SAR images can be better handled by fractal geometry rather than the Euclidian geometry. Different studies have established that there is a correlation between decreasing fractal dimension of SAR data and microwave backscatter from special objects, which help interpret SAR images [TuBA98].

2.5 Data Presentation and Condition

The data sets used in this thesis are from the ERS-1, ERS-2 and Radarsat-1 satellites (Appendix A). The test sets E1-22089R from ERS-1, E2-5551R from ERS-2 and R1-24576R from Radarsat-1 are provided by the Alaska SAR facility. In this section, only the pre-conditioning results for E1-22089R are presented. The results for the other sets are presented in Appendix A.

2.5.1 Statistics of Data

Figures 2.7 to 2.9 show histograms of a block of data from the E1-22089R test set, while Fig. 2.10 shows a normal probability plot of the same block of data. The large probability at the tails of the histogram can be attributed to the limited dynamic range of the A/D converter used to quantize the data aboard the ERS-1 satellite.

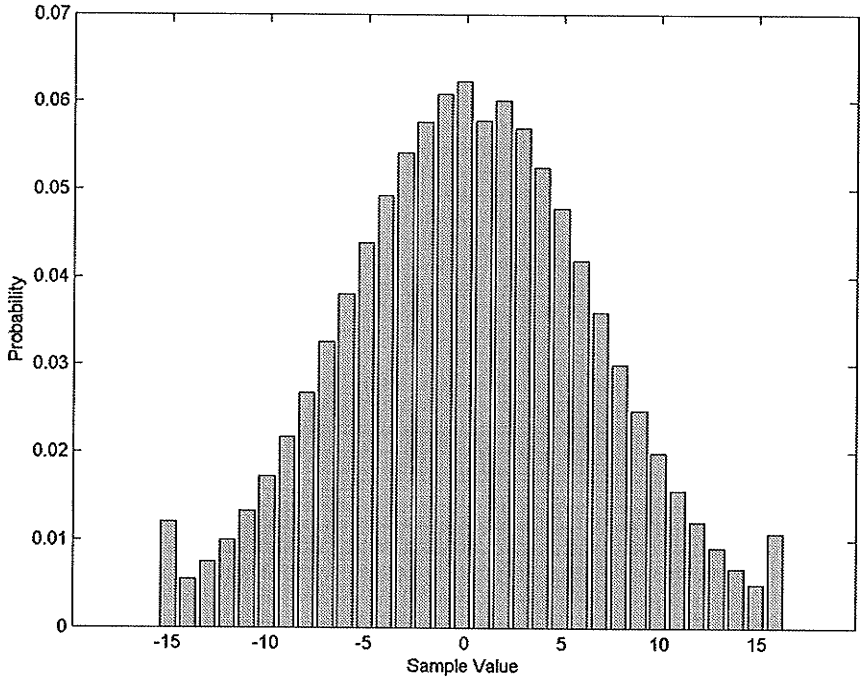

Fig. 2.7 Histogram of imaginary data from the ERS1-22089R SAR dataset.

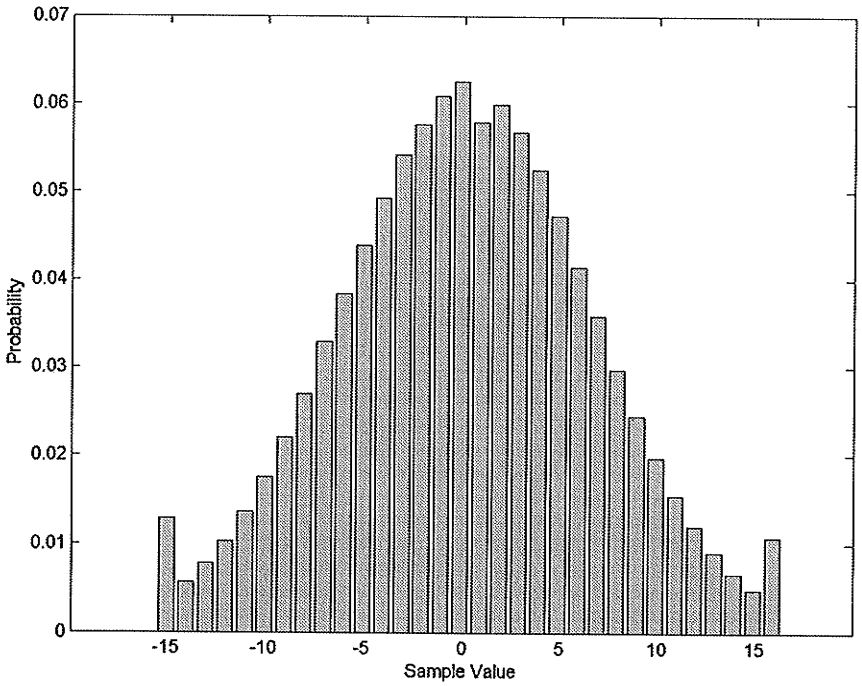

Fig. 2.8 Histogram of real data from the ERS1-22089R SAR dataset.

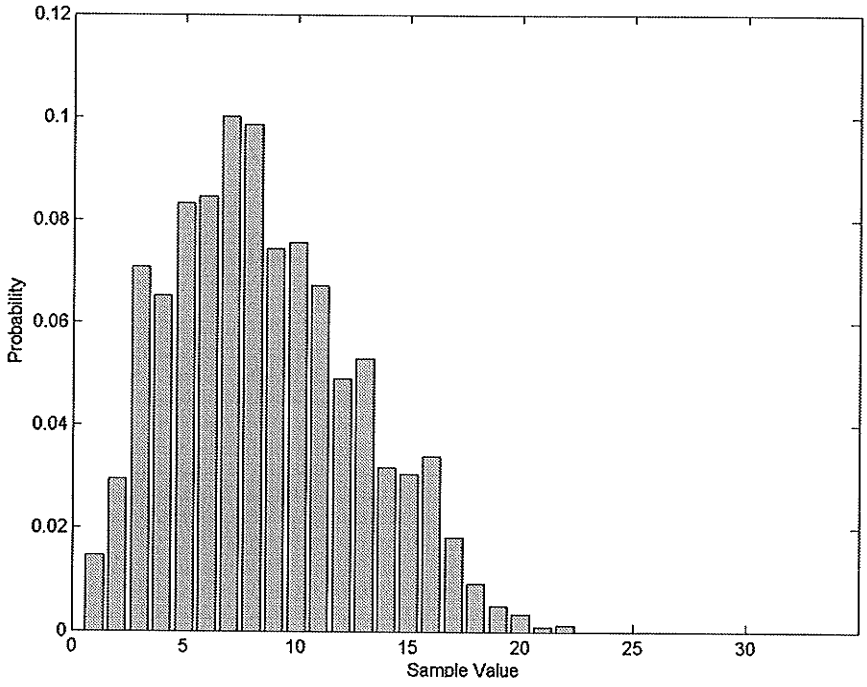

Fig. 2.9 Histogram of magnitude data from the ERS1-22089R SAR dataset.

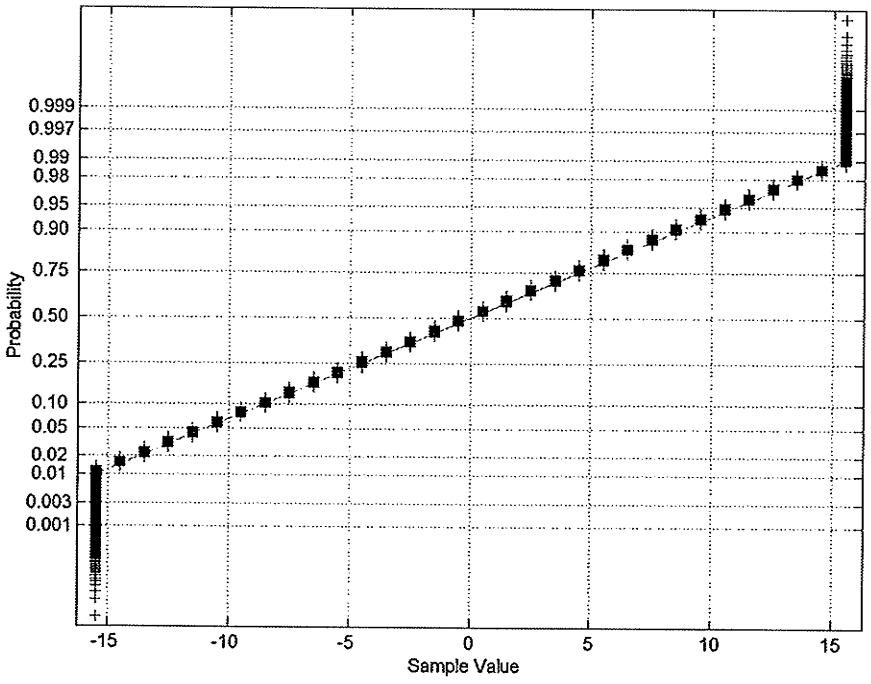

Fig. 2.10 Normal probability plot of ERS1-22089R raw SAR data.

Figure 2.10 shows that the block of raw SAR data does, in fact, follow a normal distribution, except at the tails where there is deviation. These plots shows that the statistical models derived above for the received SAR signal components are very close to the true statistics of data.

2.5.2 Data Pre-conditioning

The data compression technique used on-board ERS-1 and Radarsat-1 satellites is dynamic range reduction. This means that of the 8-bits available on the satellite, if an 8-bit A/D converter had been used, only 5-bits, or 4-bits for Radarsat, were transmitted. The problem is then how to take the 4 and 5-bit quantized raw SAR data and make it 8-bit. The resulting data, which is based on real raw SAR data, has 3 or 4 bits of additional simulated data added and is known as pre-conditioned raw SAR data [McCu95].

This problem of generating 8-bit test sets has been investigated by several researchers, however, no paper explicitly describes the pre-conditioning technique used. Instead, most refer to the proprietary ESA document developed by MacDonald Dettwiler (MDA) [Dutk93]. The standard techniques used to add the missing bits of information consist of generating noise by using either Gaussian or uniform white noise. Figures 2.11 and 2.12 show the histograms of E1-2208R data set using Gaussian and uniform noise respectively. In [Dutk93], the author reduced the data range and added negative exponential noise at the tails, and uniform noise elsewhere in order to reduce the saturation at the tails caused by the addition of uniform noise. The MDA technique can be shown to produce data that satisfies all statistical requirements [Dutk93], but the histogram is not as smooth as would be desired as shown in Fig. 2.13.

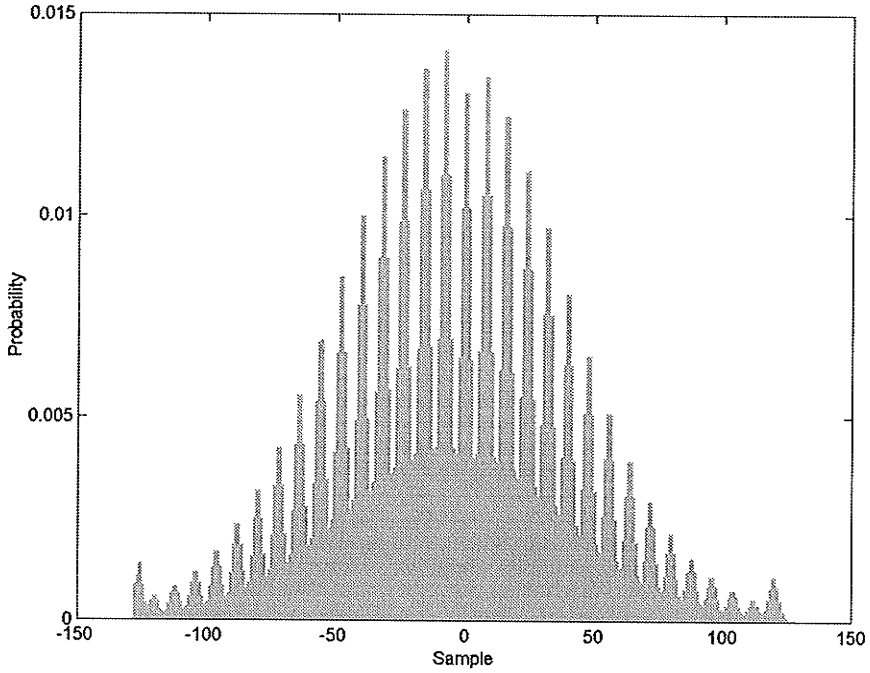

Fig. 2.11 Histogram from the E1-22089R test set pre-conditioned using Gaussian white noise technique.

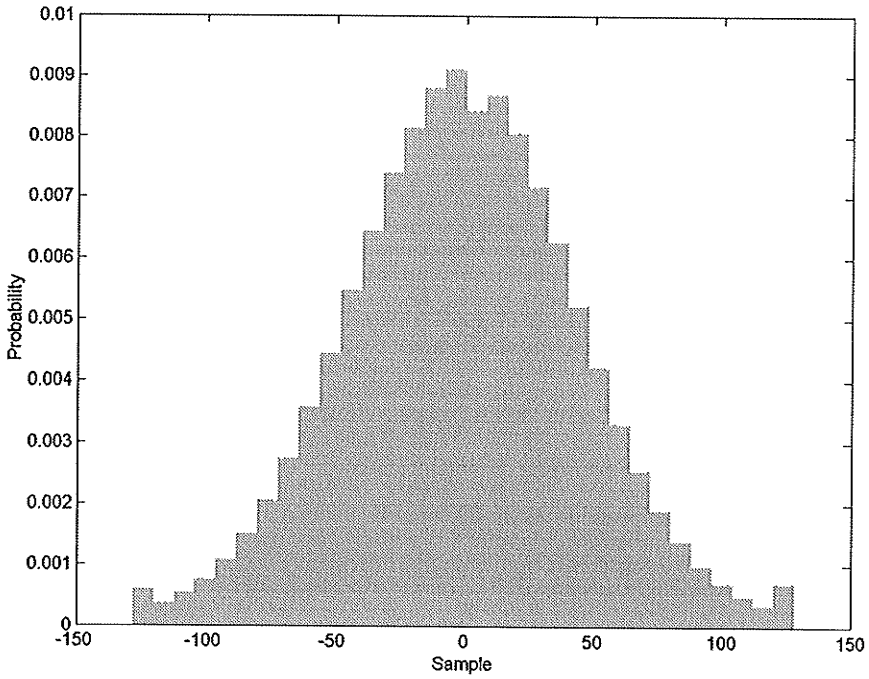

Fig. 2.12 Histogram from the E1-22089R test set pre-conditioned using the uniform white noise technique.

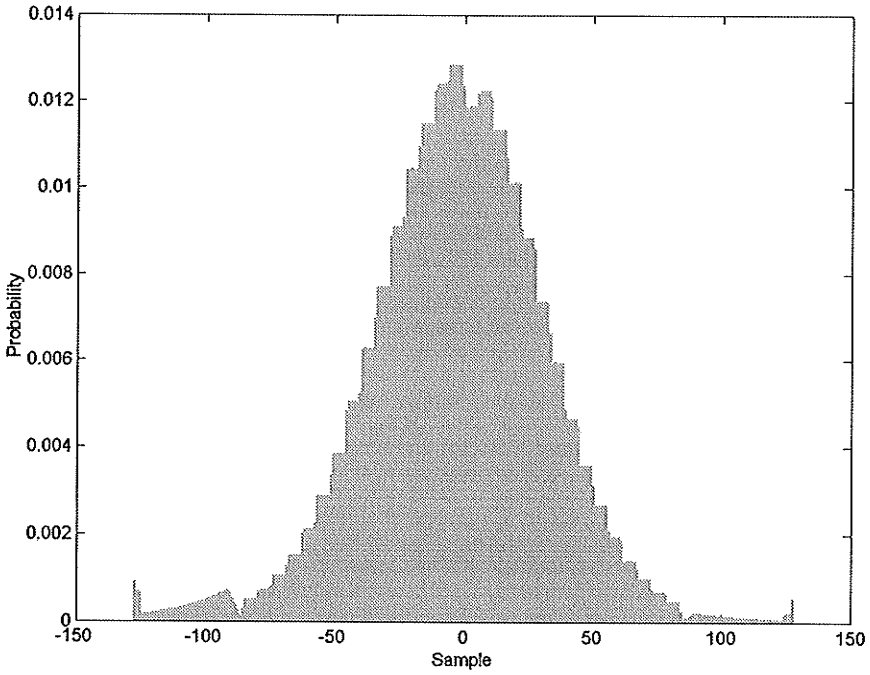

Fig. 2.13 Histogram from the E1-22089R test set using the MDA pre-conditioning technique.

In an attempt to improve upon the MDA technique a *cubic spline interpolation* [PrFT92] was investigated. Using this technique, each range line is in turn fitted using a cubic spline and is then evaluated using an offset. Following this interpolation, the data is normalized and requantized to the desired number of bits. The resulting histogram is shown in Fig. 2.14. As can be seen from the figure, the shape of the histogram is very smooth, and the saturation at the tails is less than the original data. There are, however, small local regions of higher than expected probability close to the tails as a result of the tail saturation of the original data. Upon examination of the other statistical requirements of a data pre-conditioning technique, it can be seen that the cubic spline interpolation produces good results. Statistics of the E1-22089R test set and resulting pre-conditioned data are shown in Table 2.1.

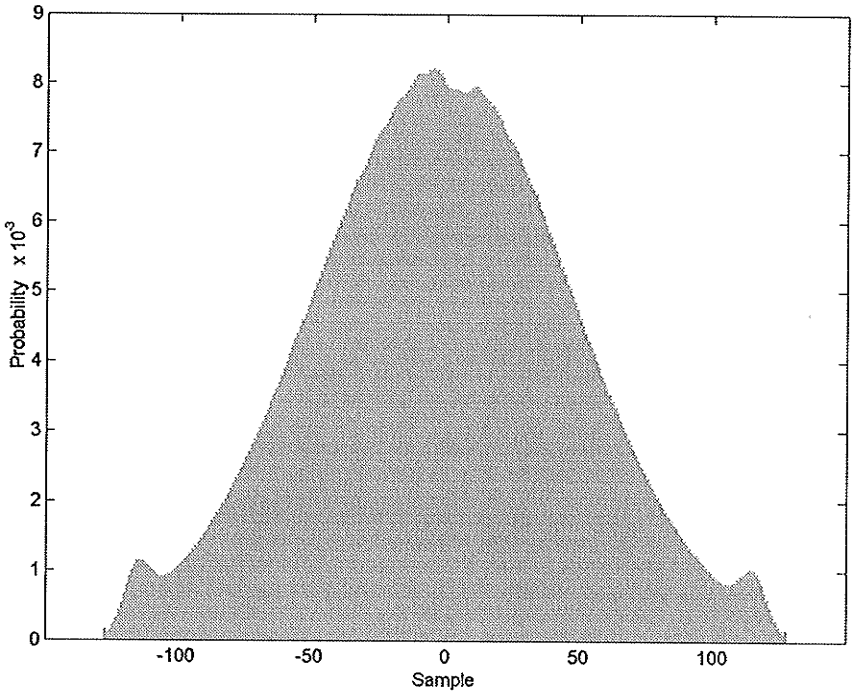

Fig. 2.14 Histogram from the E1-22089R test set pre-conditioned using the cubic spline technique.

Table 2.1: Statistics of the original and cubic spline pre-conditioned data from the E1-2208R.

Statistic	Original	Pre-conditioned (cubic spline)
Entropy	4.52	7.47
Redundancy	0.48	0.53
Standard deviation	16.37	133.68
σ factor	n/a	8.17
Kurtosis	1.44	1.39
Skewness	1.16	1.14
Mean	0.001	0.005

As seen in Table 2.1, the entropy difference is very similar, with the entropy of the pre-conditioned data only slightly less. The other statistics are also all in line with expectations, being similar or off by a factor, such as the standard deviation.

2.6 Summary

The general SAR systems principle have been presented. The range resolution of a side-looking radar is shown to be independent of the radar-target distance, and by the mean of the pulse compression technique, high range resolution can be achieved. High azimuth resolution can also be achieved by SAR processing. However, because of geometric and radiometric distortions, the azimuth processing, unlike the pulse compression, can be very complex. Under Goodman conditions, the statistics of the I and Q components of the raw SAR data are totally uncorrelated zero mean Gaussian, with identical variances. This model was confirmed on real SAR data sets and any compression technique should be adapted to it as will seen in the subsequent chapters.

CHAPTER III

CURRENT RAW SAR DATA COMPRESSION TECHNIQUES

This chapter presents a brief introduction to the probabilistic image modelling, establishes concepts such as stationarity and ergodicity, and state the hypotheses in the context of this research. Background information is then given about image compression and rate distortion theory. An overview of current raw SAR data compression techniques is organized into three sections: (i) techniques using scalar quantization, (ii) techniques using vector quantization, and (iii) techniques in the transform domain. Finally, an introduction to a new raw SAR data compression technique using neural networks is presented. Several articles have been written comparing different raw SAR data compression techniques (i.e., [KuDC94], [SBBE94], [BeSM95], [PaCl99], and [ElBK01]).

3.1 Image Modeling

As seen in Ch. 2, raw SAR data are presented as a 2-D array (image). Therefore, any compression technique may be either 2-D or 1-D, depending on the sought compression rate. In the following development, images are considered rather than 1-D signals, although the raw SAR data are not visualized before the ground processing.

A data compression algorithm is usually developed in two steps: modelling and coding. The modelling step consists of first determining the statistical distribution of data and then extracting the image characteristics for the development of a suitable compression technique. Digital images are most commonly represented in a computer as a

rectangular array of small picture elements, *pixels*. Each pixel is a random variable representing the grayscale in an image (black, white and a number of shades of gray in between).

3.1.1 Stochastic Processes

A stochastic process is a family of random variables $\{X(t), t \in T\}$. For each $t \in T$, where T is the index set of the process, $X(t)$ is a random variable (RV). The stochastic process is said to be a *discrete* (respectively *continuous*) *parameter process* if T is a discrete (respectively continuous) set, and is denoted by $\{X_n\}$. The *state space* of the process is the set of all possible values that the RV $X(t)$ can take. A stochastic process is said to be discrete or continuous if the state space is discrete or continuous, respectively.

The statistical properties of a stochastic process are determined by the family of the joint probability density functions (*pdf*) $[f_{t_1, \ldots, t_n}(x_1, \ldots, x_n), x_i, t_i, n]$. It is generally difficult to evaluate all these quantities, and in many applications the knowledge of the first ($n=1$) and second ($n=2$) order densities will suffice to characterize the process in order to compute the following three moments and a parameter

a) the mean $m(t)$ of $X(t)$ (the expected value of the RV $X(t)$) given by

$$m(t) = E[X(t)] = \int_{-\infty}^{\infty} x f_t(x) dx \tag{3.1}$$

b) the autocorrelation

$$R(t_1, t_2) = E[X(t_1)X(t_2)] = \int_{-\infty}^{\infty} \int_{-\infty}^{\infty} x_1 x_2 f_{t_1, t_2}(x_1, x_2) dx_1 dx_2 \tag{3.2}$$

c) the autocovariance

$$C(t_1, t_2) = R(t_1, t_2) - m(t_1)m(t_2) \tag{3.3}$$

d) and the correlation coefficient

$$r(t_1, t_2) = \frac{C(t_1, t_2)}{\sqrt{C(t_1, t_1)C(t_2, t_2)}} \tag{3.4}$$

$C(t_1, t_2)$ vanishes if $X(t_1)$ and $X(t_2)$ are independent. However, the converse is not true (exception has to be made for Gaussian RVs) since two uncorrelated RVs can have higher order dependencies.

Also notice that $R(t, t)$ and $C(t, t)$ are respectively the average power and the variance of the RV $X(t)$ and if $X(t)$ is centered (i.e., $m(t) = 0$), then the autocovariance is the same as the autocorrelation.

Image as a Random Field

An image is defined [GoWo92] as a sample of a 2-D stochastic process (or random field). Thus, a digital image $\{I(i, j), 1 \le i \le M, 1 \le j \le N\}$ is a realization of a discrete parameter random field $\{X_{ij}, 1 \le i \le M, 1 \le j \le N\}$. One can assume without loss of generality that each pixel is a sample of a centered RV. Therefore, the correlation between two pixels is

$$C(i, j; m, n) = E[X_{ij}X_{mn}] \tag{3.5}$$

To fully characterize this image, the joint *pdf,* which is a function of M x N variables, must be evaluated. However, this task is not possible for two reasons: (i) it is impractical (for a 512 x 512 image, there is 262144 variables), and (ii) the lack of information (there is a unique sample, the image itself). Under the stationarity and ergodicity assumptions, this problem can be made tractable.

3.1.2 Stationarity and Ergodicity

A random field is said to be *strict-sense stationary* (SSS) if its statistical properties are invariant to a shift of the origin and *ergodic* if with a probability of one, its statistics can be determined from a single sample [Papo84].

For the stochastic process $X(t)$, the SSS means that the two processes $X(t)$ and $X(t+c)$ have the same statistics for any c. $X(t)$ is ergodic in the mean if the mean $m(t) = m$ is independent of t, and

$$\lim_{T \to \infty} \frac{1}{2T} \int_{-T}^{T} X(t)dt = m \text{ (with probability one)} \tag{3.6}$$

The assumption of strict-sense stationarity is a very strong assumption, and a weaker condition is usually used, called *wide sense-stationarity.* It is given by the two conditions: (i) the mean $m(t) = m$ is independent of t, and (ii) the autocorrelation function $R(t_1, t_2)$ depends only on the difference between t_1 and t_2; i.e,

$$R(t_1, t_2) = R(t_1 - t_2) \tag{3.7}$$

Images are generally non-stationary even in the wide-sense definition (for example, the means of a dark region and a bright region in an image are not the same), therefore there is no meaning to check for ergodicity. However, in order to characterize images statistically, the stationarity and ergodicity must be assumed. Under these two conditions, the image pixels are then identically distributed and the characteristics of this same distribution can be easily estimated from the image which is now a set of samples from the underlying distribution. Thus the mean, the autocovariance, and the distribution are estimated from

$$m = \frac{1}{MN} \sum_{i=1}^{M} \sum_{j=1}^{N} I(i,j) \tag{3.8}$$

$$C(\tau_1, \tau_2) = \frac{1}{MN} \sum_{i=\tau_1}^{M} \sum_{j=\tau_2}^{N} (I(i,j) - m)(I(i-\tau_1, j-\tau_2) - m) \tag{3.9}$$

$$P(x) = \frac{number\ of\ pixels\ with\ value\ x}{MN} \tag{3.10}$$

3.2 Data Compression

Data compression is the reduction in the number of bits required to represent data. It is motivated by physical limitations: (i) limited system bandwidth for digital communication systems, and (ii) limited storage capacity for computer systems. For example, in the case of the Radarsat-1 satellite, data is collected with a maximum bandwidth B_{raw} of about 310 Mbits/s and the downlink bandwidth B_c is limited to 105

Mbits/s, so that a compression ratio of about 3:1 is necessary. Typically a downlink data rate of B_{raw} cannot be achieved since it would require a large downlink transmitter and antenna subsystem that cannot be accommodated within the platform resources given the large mass and power requirements of the SAR. The alternative is to reduce the system performance by modifying the system design or adding compression to the data collection procedure [CuMc91].

The mathematical basis for data compression is provided by information theory in general, and rate-distortion theory in particular. Both theories were developed by Claude Shannon [Shan48] who, first, defined a measure of information content of a source X with *pdf* $f(x)$ in terms of *entropy (differential)*

$$H(X) = -\int_{-\infty}^{\infty} f(x)\log_2 f(x)dx \text{ [bits/symbol]} \tag{3.11}$$

(For a discrete source, the *pdf* is replaced by the mass density function, *mdf* $[p_i]$ and the integral by the sum).

Data compression is divided into two classes: lossless and lossy compression.

Lossless compression consists of removing redundancy from data without any loss of information so that the original data are fully recovered after decompression. This kind of compression is based on the first Shannon theorem, which says that the best achievable performance by a lossless compression algorithm is to encode the source with an average number of bits equal to the entropy of the source. Many source coding

techniques have been developed and implemented, including Huffman coding [Huff51], arithmetic coding [WiNC87], Tunstall's algorithm [Mass93], and Lempel-Ziv [ZiLe77].

Due to the extremely high entropy of the raw SAR data, lossless compression techniques are not usually employed (For example, the case of 5-bit quantized raw SAR data from the E1-22089R data set, the entropy is 4.5452 bits/sample, so that the redundancy is only $5 - 4.5452 = 0.4548$ bits/sample). There has been, however, some research done on transform coding by [BrEK02] and [Bolle97], [Bolle98]. In [BrEK02], bit-planes of the raw SAR data and coded raw SAR data were investigated in an attempt to reduce the entropy of the data. It was found in [BrEK02] that none of the applied simple coding transforms yielded a significant entropy reduction, and it was suggested that a more advanced transform such as wavelets may produce better results.

The work of Bolle [Bolle97], [Bolle98] took a different approach by examining a reversible transform for the raw SAR data before entropy coding the coefficients. Bolle proposed the very interesting idea of applying a reversible transform to remove the chirp from the received SAR signal before transforming the data using the *discrete cosine transform* (DCT) and coding the coefficients, as shown in Fig. 3.1. This encoding scheme results in perfect reconstruction of the original SAR data with a compression ratio of 2.5-3.5 depending on the scene being imaged [Bolle98].

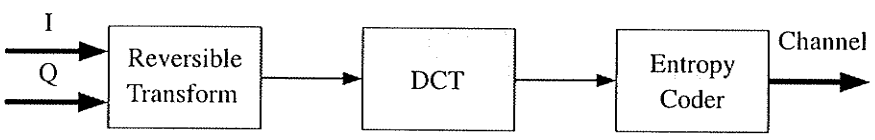

Fig. 3.1 Block diagram of Bolle encoder scheme.

Lossy compression leads to higher compression ratios at the price of some loss of information. The original data cannot be reconstructed exactly after decompression. The theoretical foundation of the lossy compression is mainly the rate-distortion theorem, also called the fourth Shannon theorem [CoTh91] which gives the theoretical bounds that can be achieved. The techniques used for implementation are essentially borrowed from quantization.

3.2.1 Rate-Distortion Theory

As stated before, the rate-distortion theory deals with the trade-offs between distortion and rate in lossy compression schemes. Given a source X with a known *pdf* $f(x)$, one seeks a discrete representation of X, denoted $\hat{X}$ using a given average bit-rate R. While doing so, a distortion, denoted by $d(x, \hat{x})$, is incurred and two kinds of optimization problems arise: (i) Given a distortion constraint $d(x, \hat{x}) \leq D$, find the representation that minimizes the rate $R(D)$, called the rate-distortion function, and (ii) given a rate constraint $r \leq R$, find the representation that minimizes the distortion $D(R)$, called the distortion-rate function. Since, in general, these two problems are reciprocal and finding one function leads to the other by a simple operation, only the rate-distortion function is considered. The evaluation of $R(D)$ is, in general, very complex and the simplification of the problem is required in many situations. The following theorem, known as the fourth Shannon theorem, relates the rate-distortion function to the mutual information and is a useful tool for the computation of $R(D)$

Theorem [CoTh91]: *For any bounded distortion $d(x, \hat{x})$, the minimum achievable rate at distortion D is given by*

$$R(D) = min\left\{ I(X;\hat{X}), f(\hat{x}/x) \,/\, \sum_{(x,\hat{x})} f(x) f(\hat{x}|x) d(x,\hat{x}) \le D \right\} \tag{3.12}$$

where $I(X;\hat{X})$ *is the mutual information between* X *and* $\hat{X}$, *and* $f(\hat{x}/x)$ *is the conditional distribution of* $\hat{X}$ *given* X.

For a memoryless Gaussian source with variance σ_x^2 , the rate-distortion function is obtained as a direct consequence of this theorem and the fact that the Gaussian distribution maximizes the entropy, by

$$R(D) = \begin{cases} \frac{1}{2}\left(\log_2 \frac{\sigma_x^2}{D}\right) & 0 \le D \le \sigma_x^2 \\ 0 & D > \sigma_x^2 \end{cases} \tag{3.13}$$

where the mean-squared-error distortion is used

$$d = E[X - \hat{X}]^2 \tag{3.14}$$

The distortion-rate function for Gaussian sources can then be expressed from Eq. 3.13 by

$$D_G(R) = \sigma_x^2 \, 2^{-2R} \tag{3.15}$$

Exactly as with the Gaussian entropy, the Gaussian distortion in Eq. 3.15 presents an upper bound for any other source distribution making the Gaussian distribution the most difficult to compress. In general an exact expression for the distortion-rate is hard to

obtain, however, Shannon derived a lower bound also

$$D_I(R) = \frac{1}{2\pi e} 2^{2(H(X)-R)} \leq D(R) \leq D_G(R) \tag{3.16}$$

The rate-distortion limit $R(D)$ is achieved in most cases by considering long blocks of source symbols, even infinitely long as illustrated by Shannon (maybe it is the reason why the word *theory* is always associated to rate-distortion). The practical design of the representation $\hat{X}$ is performed by quantization techniques presented in the following section. Before that, it is important to mention that the performance of these techniques will be evaluated primarily by comparing the SQNR (signal to quantization noise ratio) of each technique to the theoretical SQNR computed from Eq. 3.16 by

$$\text{SQNR} = 10\log_{10}\frac{\sigma_x^2}{D} \qquad [\text{dB}] \tag{3.17}$$

3.2.2 Quantization

A quantizer q can be defined as a function relating the state space of the source X to the set of representation values $\hat{X} = \{y_i;\, i \in I\}$, where I is a set of consecutive integers. This functional is completely determined by the choice of a family of disjoint and exhaustive cells $S = \{S_i;\, i \in I\}$ such that

$$q(x) = \sum_{i \in I} y_i 1_{S_i}(x) \tag{3.18}$$

where the indicator function $1_S(x)$ is 1 if $x \in S$ and 0 otherwise.

When the symbol x is represented by $q(x)$, this results in a *quantization error* $d(x, q(x)) = d(x, y_i)$ so that the overall error is

$$\sigma_q^2 = \sum_i \int_{S_i} d(x, q(x)) f(x) dx \tag{3.19}$$

Different cases can arise in formulating the quantization problem. Depending on the dimensionality of x and y_i, one can speak about scalar or vector quantization, depending on the size of I, one can have low or high-resolution quantization. One can also consider fixed-rate or variable-rate quantization and uniform versus non-uniform quantization. A complete description of all cases can be found in the excellent article [GrNe98]. Other references on the subject include [Wils80], [ChLG89], [Lloy82], [Maxj59], [Gray84], [LiBG80], [Sayo96], [GeGr92]. In the following, the Max-Lloyd algorithm and its generalized version, known as LBG algorithm are presented.

Max-Lloyd algorithm

Scalar quantization is the process of quantizing source strings, one symbol at a time. That is to say the quantizer will examine only one source output at a time, and then output the appropriate reconstruction value. In the scalar quantization case, the family S is a set of disjoint intervals of the real line, i.e $S_i = (b_{i-1}; b_i]$, $i = 1, \ldots, M$ for a fixed M.

Scalar quantizers can be uniform or non-uniform quantizers. A popular example of uniform scalar quantizer is an A/D converter. The uniform quantizer, optimal for uniform sources and easy to implement, does not give good results for other distributions.

When using a non-uniform quantizer for a source with a known distribution, it is more adequate to use a *pdf*-optimized quantizer. With the *minimum square error* (MSE), the task of designing a *pdf*-optimized quantizer is to find a set of decision boundaries $\{b_i\}$ and reconstruction values $\{y_i\}$ to minimize the distortion

$$\sigma_q^2 = \sum_{i=1}^{M} \int_{b_{i-1}}^{b_i} (x - y_i)^2 f(x) dx \tag{3.20}$$

The solution to this optimization problem is given by the following two equations

$$y_i = \frac{\int_{b_{i-1}}^{b_i} x f(x) dx}{\int_{b_{i-1}}^{b_i} f(x) dx} \text{ and } b_i = \frac{y_i + y_{i+1}}{2} \tag{3.21}$$

The problem with these two equations is that to solve for y_i one needs b_i and b_{i-1} and to solve for b_i one needs y_i and y_{i+1}. Independently, Joel Max [Max60] and Stuart Lloyd [Lloy82] developed a method permitting an iterative solution of the two equations, giving rise to the Max-Lloyd algorithm as summarized in Table 3.1.

It can be shown that for a known probability distribution, the *pdf*-optimized quantizer is the optimum scalar quantizer [Sayo96]. As can be seen from the SQNR results shown in Table 3.2, the *pdf*-optimized quantizer is still quite far from the Shannon bound given by Eq. 3.17. In fact, the *pdf*-optimized quantizer performs on average 4 dB worse than the Shannon bound for bit rates of 2-4 bits/sample. This disparity demonstrates that

the optimal scalar quantizer is not the overall optimal quantizer, and that another quantization scheme may be superior, if based on groups of pixels (vectors).

LBG algorithm

Vector quantization extends the concept of quantization from just one symbol at a time, to a string of symbols. The input string is quantized by comparing it to all codevectors in its codebook, to determine which one has the lowest distortion, then representing it by that codevector. This process is essentially a multi-dimensional quantization, where the decision boundaries of the quantizer now produce N-dimensional

Table 3.1 Max-Lloyd algorithm.

Step	Description
1	• Start with a set of reconstruction values $\{y_i^{(0)}\}_{i=1}^{M}$ • Set $k = 0$, $D^{(0)} = 0$. • Select a threshold ε.
2	• Find the decision boundaries $b_j^{(k)} = \dfrac{y_{j+1}^{(k)} + y_j^{(k)}}{2}$
3	• Compute the distortion $D^{(k)} = \sum_{j=1}^{M} \int_{b_{j-1}^{(k)}}^{b_j^{(k)}} (x - y_j^{(k)})^2 f(x)dx$
4	• If $D^{(k)} - D^{(k-1)} < \varepsilon$ then stop, otherwise continue.
5	• Set $k = k + 1$. • Compute the new reconstruction values $y_j^{(k)} = \dfrac{\int_{b_{j-1}^{(k-1)}}^{b_j^{(k-1)}} x f_x(x)dx}{\int_{b_{j-1}^{(k-1)}}^{b_j^{(k-1)}} f_x(x)dx}$ • Go to Step 2.

Table 3.2 SQNR of Gaussian optimized quantizer and Shannon bound.

bits/sample	SQNR in dB	
	PDF Optimized	Shannon Bound
2	9.30	12.04
3	14.61	18.06
4	20.17	24.08

partitions of the N-dimensional space, where N is the length of the codevectors. Vector quantization can be shown [GeGr91] to always be at least as good as scalar quantization because, by considering more than one symbol at a time, the structure that may be present in the source can be exploited. The basic vector quantization algorithm is shown in Table 3.3.

Table 3.3 Basic vector quantization algorithm.

Step	Description
1	• Create a N-dimensional vector X from N source samples.
2	• Compute the distortion D between X and all codevectors $\{Y_i\}_{i=1}^{M}$
3	• Represent the input vector X as the codevector with the smallest distortion.

The choice of codebook is of paramount concern when using vector quantization, as a poorly designed codebook produces suboptimal results. Perhaps the most commonly used algorithm for codebook design is the one developed by Linde, Buzo and Gray, known as the LBG-algorithm [LiBG80]. Their key paper [LiBG80] generalized the Max-Lloyd algorithm for the case of a known source distribution where the inputs are no longer scalars, but rather vectors. The generalized Max-Lloyd algorithm is listed in Table 3.4.

An obvious practical problem with this algorithm is that it depends on knowing the multi-dimensional *pdf* of X. Furthermore, integrals are required to calculate the distortion and centroids of odd-shaped regions in N-dimensional space at every iteration step.

Table 3.4 Generalized Max-Lloyd algorithm for codebook design.

Step	Description
1	• Start with an initial set of reconstruction values $\{Y_i^{(0)}\}_{i=1}^{M}$ • Set $k = 0$, $D^{(0)} = 0$. • Select a threshold ε.
2	• Find the quantization regions $V_i^{(k)} = \{X : d(X, Y_i^{(k)}) < d(X, Y_j^{(k)}) \quad \forall j \neq i$
3	• Compute the distortion $D^{(k)} = \sum_{i=1}^{M} \int_{V_i^{(k)}} \left\| X - Y_i^{(k)} \right\|^2 f(X) dX$
4	• If $\frac{D^{(k)} - D^{(k-1)}}{D^{(k)}} < \varepsilon$ then stop, otherwise continue.
5	• Set $k = k + 1$. • Find the new reconstruction values $\{Y_i^{(k)}\}_{i=1}^{M}$ that are the centroids of $\{V_i^{(k-1)}\}$. • Go to Step 2.

Consequently, of greater practical interest is the codebook design algorithm developed by [LiBG80] for an unknown source distribution that works on a training set of vectors. The algorithm more commonly known as the LBG algorithm is listed in Table 3.5.

The LBG algorithm guarantees that the distortion does not increase from iteration to iteration, but it does not guarantee that the algorithm will converge to the optimal solution. As can be seen from the algorithm steps, shown in Table 3.5, the final codebook

is heavily dependent on the choice of the initial reconstruction values. To address this, [LiBG80] describes a codebook initialization for the LBG algorithm called the splitting technique.

Table 3.5 LBG algorithm for vector quantizer codebook design.

Step	Description
1	• Start with an initial set of reconstruction values $\{Y_i^{(0)}\}_{i=1}^{M}$ and a set of training vectors $\{X_n\}_{n=1}^{N}$. • Set $k = 0$, $D^{(0)} = 0$. • Select a threshold ε.
2	• Find the quantization regions $\{V_i^{(k)}\}_{i=1}^{M}$ that are given by $V_i^{(k)} = \{X_n : d(X_n, Y_i^{(k)}) < d(X_n, Y_j^{(k)}) \ \ \forall j \neq i\}$ $i = 1, 2, \ldots, M$
3	• Compute the average of the distortions $D^{(k)}$ between the training vectors and their reconstruction value.
4	• If $\frac{D^{(k)} - D^{(k-1)}}{D^{(k)}} < \varepsilon$ then stop, otherwise continue.
5	• Set $k = k + 1$. • Find the new reconstruction values $\{Y_i^{(k)}\}_{i=1}^{M}$ that are the average value of the elements in each of the quantization regions $V_i^{(k-1)}$. Go to Step 2.

Using the splitting technique on a training set, the codebook is doubled at each iteration until the desired number of levels in the codebook is reached. By using the final codebook from the LBG algorithm of the previous iteration at each "splitting", the codebook is guaranteed to be at least as good as the codebook prior to splitting. If the desired number of levels is not a power of two, then during the last iteration, instead of generating two new reconstruction values for each previous reconstruction value during

the splitting step, only the necessary number of vectors are perturbed. The reconstruction points chosen to be perturbed should be those with the largest distortion, or the largest number of training set vectors.

Quantization in the Transform Domain

The motivation behind transform coding is that if a sequence of inputs is transformed into another sequence, in which most of the information is contained in only a few elements, then fewer bits will be required to represent the same information, or reduced distortion will be possible using the same number of bits. By performing a suitable linear transformation on an input vector, a new vector can be obtained. The new vector, called the transform coefficients, might have the feature that the coefficients are much less correlated than the original samples. With this correlation removed, the information may be much more compact in the sense of being concentrated in only a few of the transform coefficients. Having in this sense removed (or reduced) redundancy, the hope is to be able to quantize these coefficients more efficiently [GeGr92], [Sayo96].

A measure of the differing information of the different coefficients is the variance (thus the energy for zero-mean coefficient) of each element σ_n^2. Using the MSE as the distortion criterion, a bit allocation strategy for the transform coefficients can be found as [Sayo96], [CoTh91]

$$R_k = R + \frac{1}{2}\log_2 \frac{\sigma_k^2}{\prod_{n=1}^{M} (\sigma_n^2)^{\frac{1}{M}}} \tag{3.22}$$

where R_k is the number of bits assigned to the k^{th} coefficient, R is the average bits per coefficient desired, and M is the number of coefficients to be quantized. This equation will minimize the R_ks, but does not guarantee that the bit allocations will be integers or even positive. The standard approach to this problem is to round all R_ks to the nearest integer, zero all negative R_ks, and then uniformly reduce all the non-negative R_ks until the average rate is equal to R.

The objective is then to find the transform that most decorrelates the input. The decorrelation performance of a transform is evaluated by the *coding gain* [GeGr92]

$$G = \left(\sum_{n=1}^{M} \sigma_n^2 \right) / M \left(\prod_{n=1}^{M} \sigma_n^2 \right)^{1/M} \tag{3.23}$$

It can be shown that the *Karhunen-Loéve transform* (KTL) is an optimal decorrelation for a Gaussian distribution in that it maximizes the coding gain [Sayo96]. Unfortunately, the KLT is impractical as it requires the calculation of the autocorrelation matrix for each block of input data [GeGr92]. In the last section of this chapter, a neural network based technique approximating the KLT transform is presented. Wavelet-based transform are presented in the subsequent chapters.

3.3 Current Compression Techniques

As early as 1977, compression of raw SAR data has been a major topic of research [LiBu77] due to the enormous amount of data generated from a SAR system. Perhaps the

simplest compression technique for raw SAR data is the quantization of data itself [LiBu77]. The technique discussed in [LiBu77] addresses the problem of storing and transmitting the raw SAR signal before being processed into a SAR image, by digitizing the analog received SAR signal into digital raw SAR data. With the advancements in digital computing, the on-board quantization of the raw SAR data using A/D converter is now used on almost all SAR satellites.

Perhaps the most significant constraint in the design of a SAR system is the bandlimited downlink channel. The bandwidth necessary for a given SAR system is determined by three key factors: (i) the number of bits used in the A/D conversion, (ii) the baseband bandwidth of the received SAR signal, and (iii) the *PRF* (pulse repetition frequency). The bandwidth of the received SAR signal and the *PRF* are both determined by the geometry of the SAR radar. There are several options available to attempt a reduction in the required bandwidth by altering the radar geometry:

(1) Increase the length of the SAR antenna and reduce the *PRF* at the expense of increased mass and degraded azimuth resolution;

(2) Reduce the bandwidth of the transmitted radar pulse and/or the oversampling factor to reduce the A/D converter sampling frequency at the expense of degraded range resolution;

(3) Reduce the swath width by increasing the incidence angle or changing the radar geometry at the expense of reduced ground coverage and increased geometric distortion from foreshortening and layover effects [CuMc91 Ch.8]; and

(4) Reduce the quantization performed by the A/D converter to fewer bits per sample at the expense of increased distortion noise and, therefore, degraded radiometric accuracy.

Of all the options, Option 4 has been most typically used aboard SAR systems, as the range and azimuth resolution are still maintained and it is implemented by simply using an A/D converter with a larger quantization step size. The resulting radiometric loss produces images with less dynamic range and more overall noise. This technique is currently used aboard the ERS-1 [Atte91] and the Radarsat-1 satellites.

As indicated in Ch. 1, the most widely recognized technique for raw SAR data compression is the block adaptive quantization (BAQ) developed by [KwJo89]. The other techniques were developed in order to increase the performance by using, in most cases, a different quantization method. In [ElBK01], the authors presented a review of the current raw SAR data compression techniques which were separated into three different categories according to the method of quantization, scalar or vector, and the domain of compression. Although a multitude of methods of evaluating the effects of coding on SAR data exists (e.g., [ArVE99], [DuCu92], [DuCu94], [HOCC88]), the SNR is used here to compare the different techniques.

3.3.1 Techniques Using Scalar Quantization

Block Adaptive Quantization

The *block adaptive quantization* (BAQ) was developed by Kwok and Johnson of the NASA JPL [KwJo89]. As indicated by its name, the BAQ algorithm takes advantage of the slowly varying echo power in range from pulse-to-pulse to allow the block

adaptation of the quantizer. This is accomplished by the determination of the statistics for each block of data samples, which in turn is used to adjust the quantizer levels. Since the statistical distribution of the real (I) and quadrature (Q) data samples is assumed to be zero-mean Gaussian with identical variance, the standard deviation is the only parameter necessary to describe the distribution.

The choice of block size is an important parameter in the BAQ algorithm. It is essentially a trade-off between the number of samples necessary to ensure that the block will have a Gaussian distribution, and an attempt to minimize the block size to keep valid the stationary signal assumption.

The BAQ algorithm is a non-uniform quantizer optimized for a Gaussian probability distribution where the threshold values are adapted on a block by block basis, and are derived from the variance of the block. A block diagram of the algorithm is shown in Fig. 3.2.

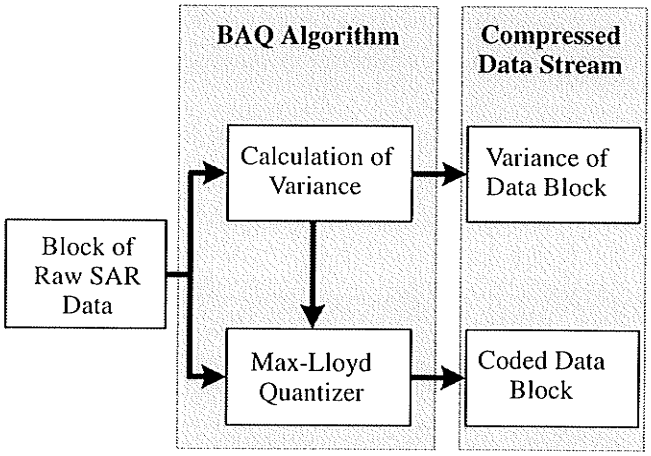

Fig. 3.2 Block diagram of the BAQ algorithm.

For the Magellan mission to Venus, the BAQ algorithm was modified slightly for two reasons: (i) to reduce hardware complexity, the average signal magnitude was used as

an estimate of the standard deviation, and (ii) to preserve the radiometric energy of the reconstructed signal, the Max-Lloyd quantizer construction levels were adjusted.

As shown in Fig. 3.3, the average signal magnitude $|\bar{I}| = |\bar{Q}|$ is a close approximation to the standard deviation. The performance difference between using the average magnitude statistic and the variance is small, however, the hardware complexity savings were significant [KwJo89].

The energy after quantization to the signal energy ratio is given by

$$G = \frac{E[(q(X))^2]}{E[X^2]} = \frac{1}{\sigma^2}\sum_{i=1}^{M}\int_{b_{i-1}}^{b_i} y_i^2 f(x)dx \tag{3.24}$$

In the case of a 4-level symmetric quantizer (2-bit quantization), Eq. 3.24 can be simplified to

$$G = 2\left[\frac{1}{2}\left(\frac{y_1}{\sigma}\right)^2 erf\left(\frac{b_2}{\sigma}\right) + \frac{1}{2}\left(\frac{y_2}{\sigma}\right)^2\left[1 - erf\left(\frac{b_2}{\sigma}\right)\right]\right] \tag{3.25}$$

Using the Max-Lloyd reconstruction levels for 2 bits [Sayo96] into Eq. 3.25, it is easy to obtain $G \approx 0.8825$. Therefore, the average energy of the quantized raw SAR data is $0.8825\sigma^2$. In order to maintain the radiometric energy of the reconstructed raw SAR signal, the reconstruction levels of the Max-Lloyd quantizer would have to be raised by a factor of $1/0.8825$, resulting in the reconstruction levels of $\pm 0.52\sigma$ and $\pm 1.72\sigma$. This change in reconstruction levels also changes the SNR of the reconstructed signal for a

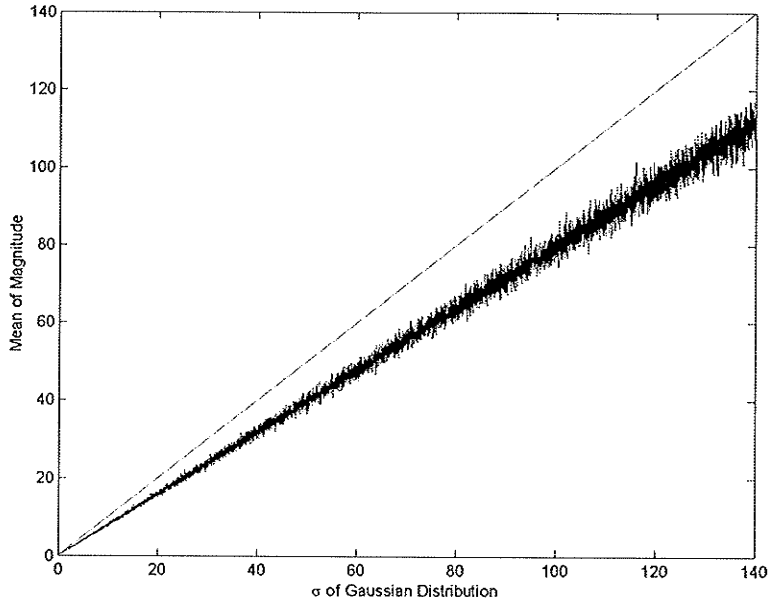

Fig. 3.3 Average magnitude versus standard deviation of a Gaussian signal.

2-bit BAQ to 8.76 dB as shown in Table 3.6. Although BAQ does produce acceptable results and presents a low implementation complexity, it is still quite far from the Shannon bound as shown in Table 3.6.

Table 3.6 SQNR of BAQ, radiometric corrected BAQ, and the Shannon bound using the test set E1-22089R

bits/sample	SQNR [dB]		
	BAQ	BAQ with Radiometric Correction	Shannon Bound
2	9.30	8.76	12.04
3	14.61	14.46	18.06
4	20.23	20.18	24.08

Flexible BAQ

A slight variation on the BAQ algorithm is the flexible BAQ (FBAQ) [McCu95], [KuDC94]. The FBAQ algorithm works in the same manner as the Magellan BAQ except that the number of quantization bits for a given imaging pass is programmable from the ground station. FBAQ also only operates on a 1-D vector of samples, whereas the Magellan BAQ operates on a 2-D block of samples [KuDC94]. The finding of [KuDC94] indicates no significant improvement in the performance of the algorithm using a 2-D block, and therefore decided on the simpler 1-D block. The findings also demonstrate the performance of FBAQ to be the same as the Magellan BAQ. A block diagram of FBAQ is shown in Fig. 3.4.

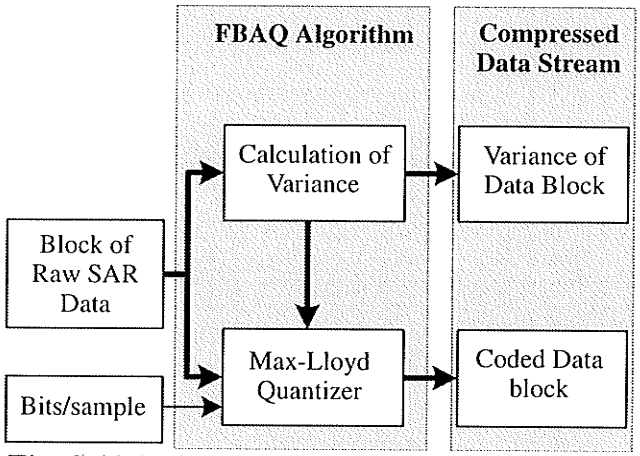

Fig. 3.4 Block diagram of the FBAQ algorithm.

Fuzzy Block Adaptive Quantization

The BAQ algorithm assumes that all blocks are Gaussian zero-mean distributed; however, a small block does not guarantee this supposition. The *fuzzy block adaptive quantization* (fuzzy-BAQ) attempts to improve this by the determination of the degree of

membership of each block of data to a distinct Gaussian distribution [Benz94], [BeSM95], [SBBE94]. The membership then determines which Gaussian distribution, and thereby which variance, best represents the data to give the lowest distortion. A block diagram of the fuzzy-BAQ algorithm is shown in Fig. 3.5.

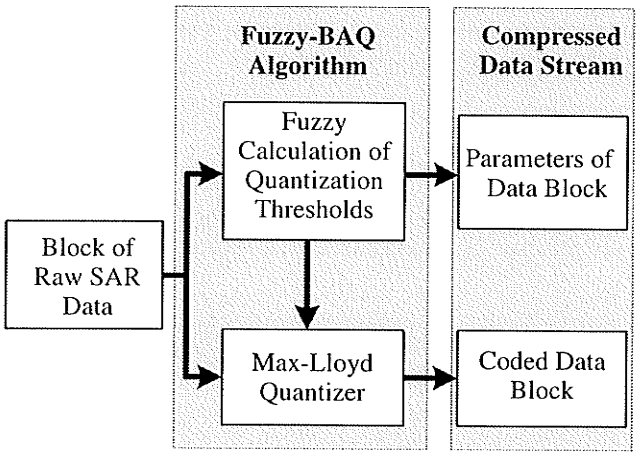

Fig. 3.5 Block diagram of the fuzzy-BAQ algorithm.

The estimation of the standard deviation and other quantization parameters such as the reconstruction levels are computed using a fuzzy system. The fuzzy input variables are generated by the fuzzification of the crisp input variables, where the inputs are frequencies of the distinct values in the block. Using a rule-based algorithm, the fuzzy output variables are then calculated. Finally, the defuzzified output variables are used for the quantization. Performance results from the fuzzy-BAQ algorithm developed in [BeSM95] are shown in Table 3.7.

Table 3.7 SQNR of fuzzy-BAQ [BeSM95] and BAQ.

bits/sample	SQNR [dB]	
	Fuzzy-BAQ	BAQ
2	10.7	9.30
3	n/a	14.61
4	n/a	20.23

Block Adaptive Histogram Equalization Quantization

The block adaptive histogram equalization quantization (BHEQ) [KuDC94] is an algorithm that first transforms a block of raw SAR data from a Gaussian distribution to a uniform distribution using the variance of the block. The transformation is achieved by computing the cumulative distribution function of the Gaussian distribution, and can be performed using look-up tables [KuDC94]. A block diagram of the BHEQ algorithm is shown in Fig. 3.6.

The BHEQ algorithm approaches, without surpassing, the SQNR of BAQ using a uniform quantizer. This lower SQNR is the result of the BHEQ minimizing the quantization error in the histogram-equalized domain, and not the quantization error in the original Gaussian distribution. Although BHEQ has a lower SQNR than BAQ, it has the benefit of a slightly less complex quantizer.

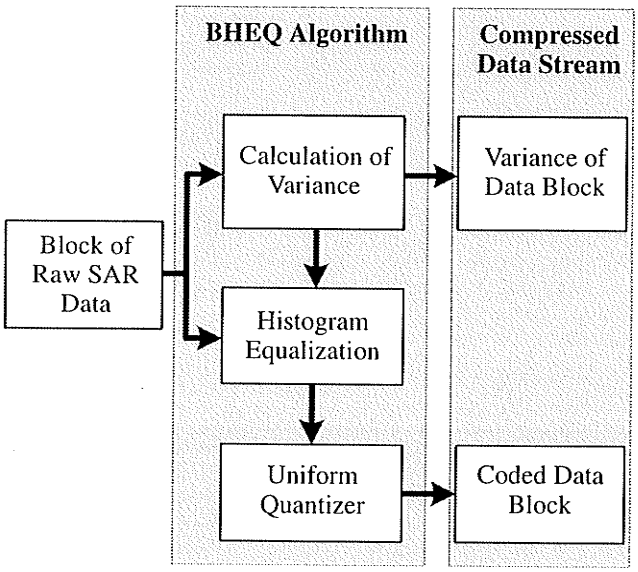

Fig. 3.6 Block diagram of the BHEQ algorithm.

The SQNR results for BHEQ algorithm developed in [KuDC94] are shown in Table 3.8 and compared with BAQ. These SQNR results show that the BHEQ is consistently inferior to BAQ by, on average, 0.24 dB.

Table 3.8 SQNR of BHEQ [KuDC94], and BAQ.

bits/sample	SQNR [dB]	
	BHEQ	BAQ
2	9.15	9.30
3	14.34	14.61
4	19.94	20.23

Block Adaptive Complex Quantization

In a typical SAR system, the raw SAR data is digitized as individual streams of real (I) and quadrature (Q) data samples. The *block adaptive complex quantization* (BACQ) functions by treating a pair of I and Q values as a complex sample, and then quantizing the sample using a quantizer with boundaries and reconstruction levels in 2-dimensional space [KuDC94]. Treating the data as a complex sample is essentially applying vector quantization to BAQ, where the codebook is comprised of vectors of length two. This algorithm is discussed in this section because the complex value is treated as a single scalar.

To ensure that only one codebook is needed for the complex quantizer, each block of raw SAR data must have the same statistics. To accomplish this, the block can be histogram equalized [KuDC94], or simply normalized (divided by its variance). A block diagram of the BACQ algorithm is shown in Fig. 3.7.

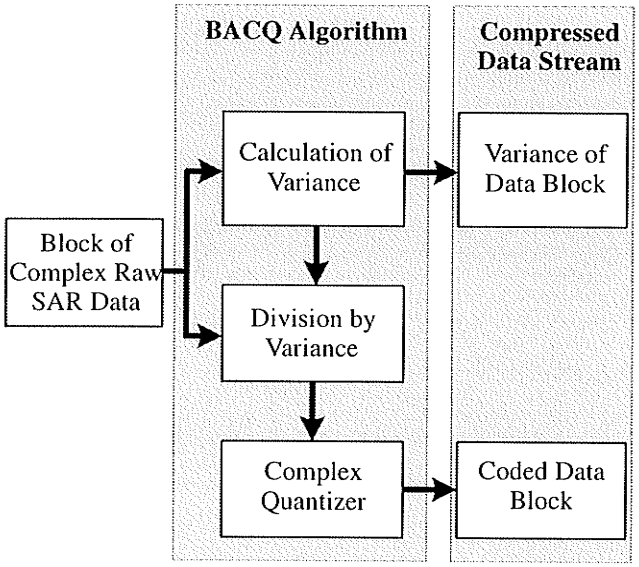

Fig. 3.7 Block diagram of the BACQ algorithm.

The SQNR results for BACQ algorithm developed in [KuDC94] are shown in Table 3.9 and compared with BAQ. The only results presented in [KuDC94] for BACQ is for 2 bits/sample, and this result is inferior to BAQ by 0.15 dB.

Table 3.9 SQNR of BACQ [KuDC94] and BAQ.

bits/sample	SQNR [dB]	
	BACQ	BAQ
2	9.15	9.30
3	n/a	14.61
4	n/a	20.23

Entropy-Constrained Block Adaptive Quantization

More recently, an *entropy-constrained BAQ* (ECBAQ) has been proposed by [Algr00]. This technique promises to outperform BAQ in SQNR, while still maintaining a low level of computational complexity. The implementation of ECBAQ by [Algr00] also

possesses the ability to control the output data rate by adjusting the level of quantization. This adjustment can be done without the need for developing new hardware, and can use non-integer rates.

The ECBAQ algorithm is simply an optimum quantizer, followed by an entropy coder. The quantizer in ECBAQ is an adaptive quantizer which adapts the thresholds based on the standard deviation of each block of data. This, in turn, also adapts the entropy coder. Unlike BAQ, where the optimum quantizer is non-uniform, a uniform quantizer in ECBAQ is optimum. In [Algr00], the entropy coder used is a Huffman coder [Sayo96]. However, an adaptive arithmetic coder could also be used. A block diagram of the ECBAQ algorithm is shown in Fig. 3.8.

The SQNR results for ECBAQ algorithm developed in [Algr00] are shown in Table 3.10 and are compared with BAQ. As can be seen from the SQNR results, ECBAQ outperforms BAQ at all bit rates by 1.31 dB, on average.

Table 3.10 SQNR of ECBAQ [Algr00] and BAQ.

bits/sample	SQNR [dB]	
	ECBAQ	BAQ
2	9.67	9.30
3	16.17	14.61
4	22.23	20.23

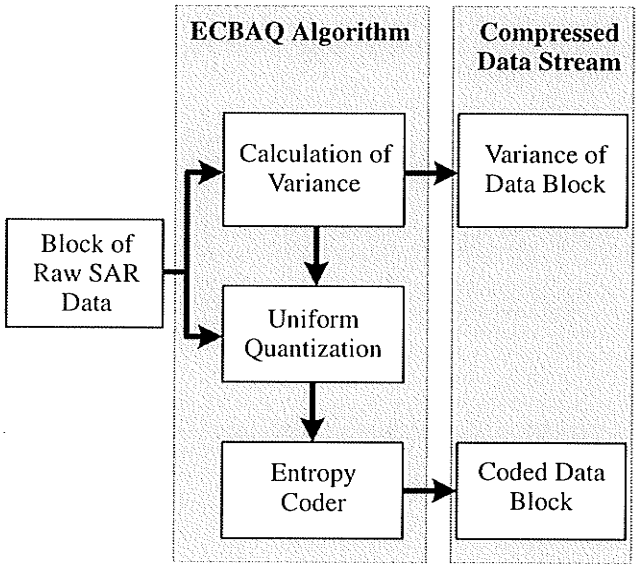

Fig. 3.8 Block diagram of the ECBAQ algorithm.

Block Floating Point Quantization

The *block floating point quantization* (BFPQ) is similar to the BAQ algorithm, except that BFPQ uses a uniform quantizer, whereas BAQ uses a non-uniform quantizer [Hune89], [Hune90], [JoHW91]. The uniform quantization in BFPQ is simply a division by the quantization step adapted to each block, followed by a rounding. To speed up the calculation time, the quantization step can be rounded to the nearest power of 2, making the division a simple right shift.

The BFPQ algorithm derives its name from both the block of raw SAR data which are uniformly quantized and the subsets of available bits being selected by a predetermined algorithm, the equivalent of moving the "floating point" marker of the binary data. A block diagram of the BFPQ algorithm is shown in Fig. 3.9.

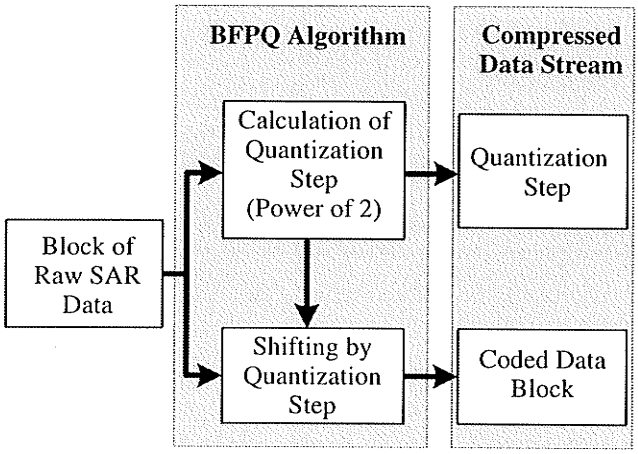

Fig. 3.9 Block diagram of the BFPQ algorithm.

The BFPQ is particularly attractive because of its low computation complexity, which is even lower than that of BAQ. Like the BAQ algorithm, the BFPQ can adapt to the variation in power; however, the performance of BFPQ is always inferior to that of BAQ because BFPQ uses a non optimal quantizer. The BFPQ has been used on several SAR systems, most notably the SIR missions [Hune89].

3.3.2 Techniques Using Vector Quantization

As indicated already, from communication theory, it can be shown that vector quantization always performs at least as well as scalar quantization [Gray84]. It is then a natural progression for vector quantization to be applied in the compression of raw SAR data. Many researchers have applied vector quantization to raw SAR data compression, approaching it from two different perspectives. The first group of researchers developed techniques to apply vector quantization to the entire data frame at once [Arno87], [JVFC88], [MGBB94], [RACC88], and the second group of researchers applied vector

quantization on blocks of raw SAR data [Lebe95], [LMBL95], [BoBl93], [SBBE94], [BeSM95], [PaCl99].

Vector Quantization

The appeal of vector quantization in other applications has led researchers to apply it in the compression of raw SAR data. The techniques used in [Arno87], [JVFC88], [MGBB94], and [RACC88], are fundamentally the same, whereby a vector quantizer is used to compress an entire raw SAR data frame at once. The standard techniques of LGB and lattice vector quantization have been used to design the codebooks [Arno87], [MGBB94], in addition to determining the optimal codebook size [JVFC88]. Although no raw SAR data SQNR results are described in those papers, it is noted in [MGBB94] that vector quantization outperforms BAQ, especially at low bit rates. It was also noted in [MGBB94] that the lattice vector codebook design was superior to the LBG codebook.

Block Adaptive Vector Quantization

It has been shown [KwJo89] that raw SAR data has a slow-changing power in both range and azimuth directions. By applying vector quantization on a block-by-block basis, the vector quantizer codebook can be more specific to the statistics of the given block. If the block of raw SAR data is normalized to have the same variance, then only one codebook is needed for all blocks. This sequence is basically a BAQ with the output followed by a vector quantizer. The resulting algorithms, which are all fundamentally the same, are the *block gain adaptive vector quantization* (BGAVQ) [Lebe95], [LMBL95], the *block adaptive vector quantization* (BAVQ) [MoBl93], [SBBE94], [BeSM95], and the *gain-shape vector quantization* (GSVQ) [PaCl99]. A block diagram of the BAVQ is

shown in Fig. 3.10. Performance results for the BGAVQ algorithm from [Lebe95] for a vector of length 4 and compared with BAQ, are shown in Table 3.12. It has been noted by most relevant authors that the computation complexity increase for a block vector quantization technique is slightly larger than BAQ, but the performance results justify this increase.

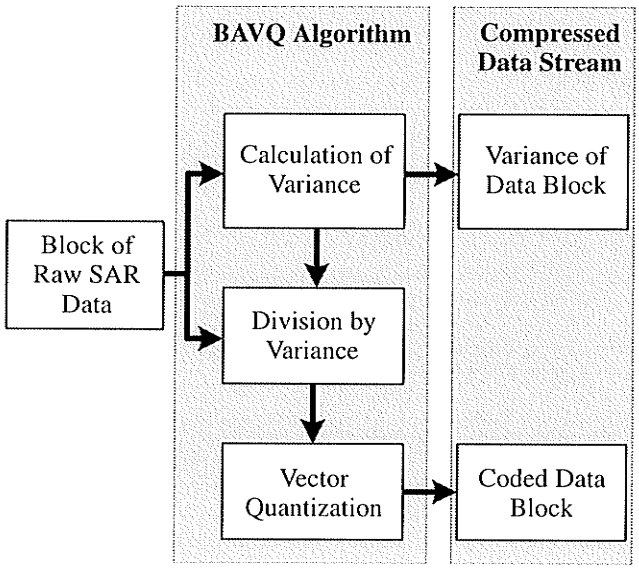

Fig. 3.10 Block diagram of the BAVQ algorithm.

The BAVQ algorithm can be broken down into the following four steps as shown in Table 3.11.

Table 3.11 BAVQ algorithm.

Step	Description
1	• Acquisition of a block of raw SAR data in range.
2	• Calculation of the variance of the block.
3	• Normalization of the block by division by the block's variance.
4	• Quantization of each vector of samples using a vector quantizer and a predesigned codebook.

Trellis Coded Quantization

Similar to the idea of vector quantization is the *trellis coded quantization* (TCQ), which has been applied in the compression of raw SAR data by several researchers [Owen97], [OMHK97], [OMHK99]. One of the attractive features of TCQ is that it can process very long vectors with a computational complexity that is independent of vector length. This is in sharp contrast to full search vector quantization which requires exponential complexity for increasing vector length.

Two TCQ techniques have been applied in the compression of raw SAR data, the *trellis coded vector quantization* (TCVQ), and the *universal TCQ* (UTCQ). UTCQ is a refinement over TCQ in that it does not require trained and stored codebooks, and allows non integer encoding rates. However, UTCQ uses an arithmetic coder [Sayo96] and as such has variable length codes making it very sensitive to bit error rates. TCVQ addresses this problem by using fixed length codes. More detailed information on TCQ can be found in [FiMW91]. Performance results for TCVQ and UTCQ from [OMHK99] are shown in Table 3.12 and compared with BAQ. These results show that both TCVQ and UTCQ outperform BAQ at all bit rates with UTCQ yielding the greatest gains. The SQBR results show that UTCQ outperforms BAQ by 1.86 dB on average and increases in SQNR gains with increasing bit rates.

Table 3.12 SQNR of TCVQ [OMHK99], UTCQ [OMHK99], and BAQ.

bits/sample	SQNR [dB]			
	BAQ	TCVQ	UTCQ	Shannon Bound
1	4.39	5.19	5.22	6.02
2	9.30	10.69	11.30	12.04
3	14.61	16.29	17.37	18.06

3.3.3 Techniques in the Transform Domain

Transform BAQ

The BAQ algorithm was developed to compress a zero mean Gaussian signal, such as raw SAR data. This means that BAQ can also be applied to transform raw SAR data if it has the same statistics, as is the case of an orthogonal transform. This has led to substantial research in the development of transform-based BAQ algorithms [SBBE94], [BeSM95], and [FiBM99]. That research attempted several transforms such as the *discrete cosine transform* (DCT), the *Walsh-Hadamard transform* (WHT), and the *fast Fourier transform* (FFT).

All of these transform based BAQ techniques work in the same manner as shown in the block diagram of Fig. 3.11. The techniques are simply a transform on a block of raw SAR data followed by a BAQ of the coefficients.

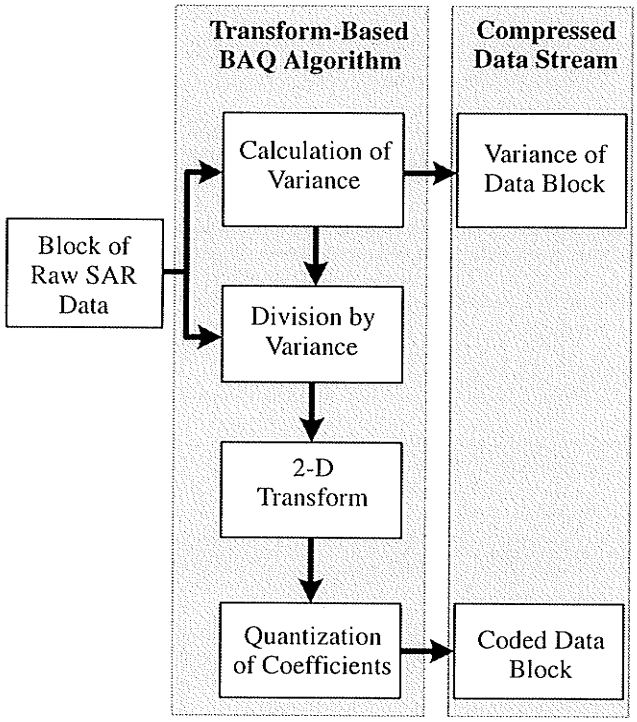

Fig. 3.11 Block diagram of transform based BAQ.

The transform based BAQ algorithms can be broken down into the following five steps, as shown in Table 3.13.

Table 3.13 Transform-based BAQ algorithm.

Step	Description
1	• Acquisition of a 2-D block of raw SAR data.
2	• Calculation of the variance of the block.
3	• Normalization of the block by division by the block's variance.
4	• 2-D transformation of the block of data.
5	• Quantization of the transform coefficients using BAQ.

Although no SQNR performance metrics in the signal domain are given in the papers, it has been noted in [BeSM95] that the FFT-BAQ algorithm had the best performance but the highest computational complexity.

Particularities of the FFT-BAQ Algorithm

The idea presented in [BeSM95] for FFT-BAQ is to adapt the data compression to the energy variation of the frequency envelope of the raw SAR data, thereby quantizing the regions with higher energy with more bits. Additionally, the frequency region outside the processed bandwidth does not need to be coded at all. This then requires that the BAQ used on the transformed data has a variable compression ratio.

[BeSM95] claims that in practice, the processed bandwidth corresponds to approximately 85% of the full signal bandwidth, allowing an immediate data reduction of 15% with no image degradation. The bit allocation scheme for the BAQ used on the transformed data in the FFT-BAQ from [BeSM95] is shown in Fig. 3.12.

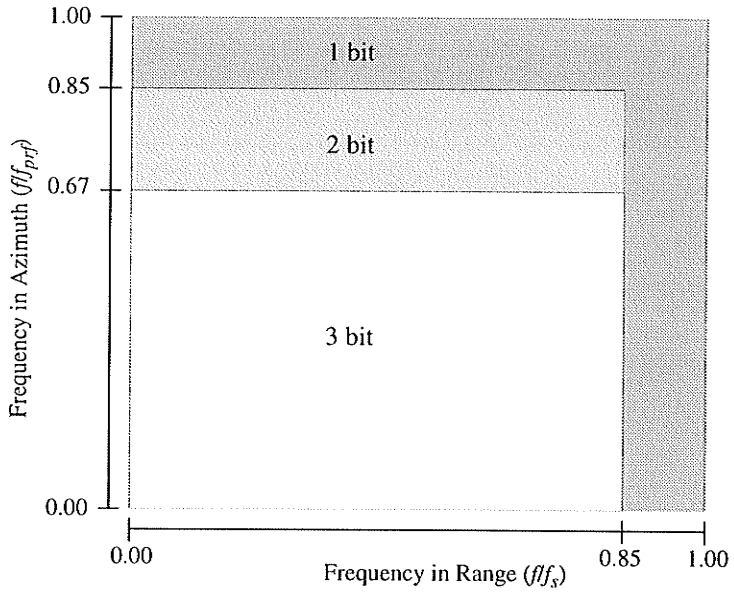

Fig. 3.12 Bit allocation scheme for FFT-BAQ (From [BeSM95]).

Compression Using Wavelets

The growing popularity of wavelets, has led several researchers to take an interest in applying wavelets to the compression of raw SAR data. In [PaSc99], [PaSB99], [PaSc00] wavelets were applied to the entire data frame at once to compress the raw SAR data. An alternative approach to applying wavelets directly to the entire data frame is to apply it to blocks of data and adapt the quantization to the specifics of each block, thereby creating the wavelet-BAQ. In [ETHB02], the authors have introduced an algorithm whereby blocks of raw SAR data are transformed using DWT and the coefficients quantized using a Max-Lloyd quantizer for Gaussian distribution. This algorithm will be summarized in Ch. 4.

To end this chapter, a neural network based technique for raw SAR data compression is described. The motivation for this approach comes from the observation that the data come from a Gaussian distribution, while the architecture of the neural network considered performs a KLT which offers the optimal decorrelation for Gaussian processes among all transforms.

3.4 Back-Propagation Based Compression

Back-propagation neural networks (BPNN) have been used extensively for compression purposes, and have been shown to be an approach of choice mainly because of their massively parallel computation, which provides fast algorithms [Jian99]. This is a strong advantage when the amount of data is important, as it is the case for raw SAR data.

The BPNN used in raw SAR data compression scheme consists of one input layer of N neurons, one hidden layer of K neurons and one output layer of N neurons, as shown on Fig. 3.13. This network architecture was also used for medical images compression [ElKi01]. It achieves a compression ratio of $(N/K):1$. The network training uses for the output the same data frame as the input. During the training process, the network synaptic weights w_{ji} and w'_{ij} are adjusted iteratively in order to minimize the error term

$$E_i = \frac{1}{N}\sum_{j=1}^{N} e_{ij}^2 = \frac{1}{N}\sum_{j=1}^{N} (x_{ij} - o_{ij})^2 \tag{3.26}$$

where the (x_{ij}) are the input values and the (o_{ij}) are the output values of the BPNN.

The transfer functions used in the hidden and output layers are linear functions. In fact, the linear BPNN for compression has been proven to outperform non-linear networks (which use sigmoid transfer functions) in terms of training speed and compression performance [MoAA91], [CoMZ87].

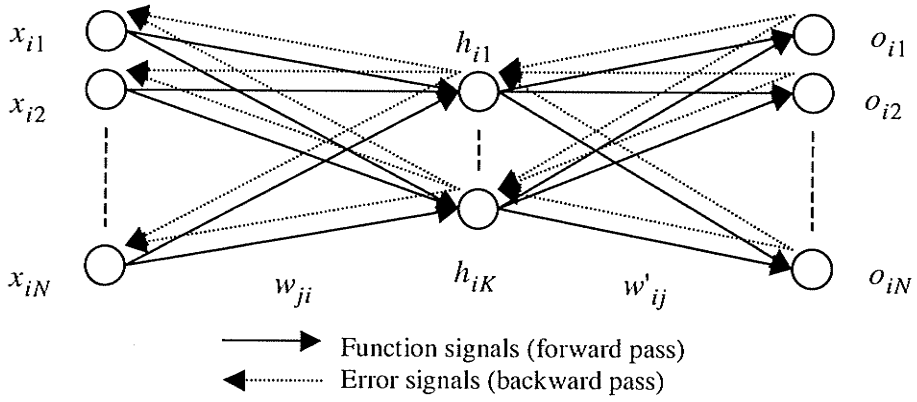

Fig. 3.13 Back-propagation neural network

3.4.1 Experimental Results

All experiments were performed on a SUN SPARCstation 5. A training set of about 3500 blocks taken from the data frame E1-22089R was used. The input layer is composed of 9 neurons to process the 3x3 successive non-overlapping blocks, i.e., $N=9$. K has been chosen from 1 to 3 neurons, leading to the compression ratios 9:1, 4.5:1 and 3:1. The performance goal (evaluated by Eq. 3.26) for the BPNN was set to 10^{-4}, with an adaptive learning rate.

Once the BPNN was trained (i.e., the network synaptic weights w_{ji} and w'_{ij} are determined), the method was tested on both training set E1-22089R and on the set R1-24576R. Since the raw data are not readable (as can be seen from Fig. 3.14), only the computation of the SNR is of interest. Table 3.14 shows the results for both test sets. Table 3.15 presents the BAQ performance (SQNR) on the three test sets and the Shannon bound. Although the BPNN performance does not reach the Shannon bound, it outperforms the BAQ technique. It is well known that linear auto associative NN is similar to the principal component analysis (PCA) approach [Kram91]. The BPNN scheme presented here is then a good approximation of the KLT. This scheme presents also the advantage of reaching rational bit-per-sample (bps) values. Moreover, since the SNR values are very comparable for both the training set and for the other set, it demonstrates good generalization properties of the present method.

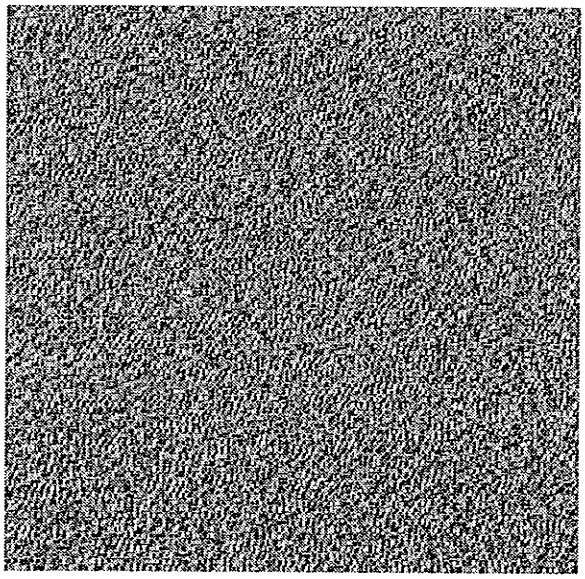

Fig. 3.14 Raw SAR data: frame from the set E1-22089R.

Table 3.14 SNR values using BPNN.

bits/sample	SNR [dB]	
	E1-22089R	R1-24576R
0.89	5.14	5.03
1.78	10.21	9.89
2.67	16.13	15.94

Table 3.15 SQNR values using BAQ as well as the Shannon bounds.

	Test Set SQNR [dB]								
	E1-22089R			E2-5551P			R1-24576R		
	2	3	4	2	3	4	2	3	4
Shannon Bound	12.04	18.06	24.08	12.04	18.06	24.08	12.04	18.06	24.08
BAQ	9.60	15.00	20.51	9.36	14.66	20.19	9.45	15.02	20.42

3.5 Summary

Throughout research on raw SAR compression, many techniques have been developed and attempted, but the BAQ algorithm developed by NASA JPL still remains the standard. Recent work in the vector quantization of raw SAR data and transform based technique have shown promising results. It is important to note, however, that most techniques achieve SQNR performance results that are not significantly different than BAQ, and are still quite far from the theoretical Shannon bound.

Of the techniques developed and discussed in this chapter, vector quantization based techniques appear to perform better at the price of complexity increase. The proposed neural network-based scheme gives better results than BAQ. Transform techniques are most promising as they are able to decorrelate the raw SAR data, removing any redundancy that may exist. This issue will be addressed in the following chapter by developing a raw SAR data compression technique based on wavelets and optimal wavelets.

CHAPTER IV

WAVELETS AND APPLICATION TO RAW SAR DATA COMPRESSION

The goal of this chapter is to provide an introduction to the wavelet transform in its different forms and to apply the discrete wavelet transform to raw SAR data compression. In this presentation, the historical development made in the subject is followed. Hence we the wavelet development is motivated by underlining the limitations of the Fourier analysis in some situations. Once the theory is stated, a transform-based compression system using the Haar wavelet, the Battle-Lemarié wavelets (linear and quadratic) and Daubechies wavelets (D4 and D20) is presented. The transformed data are then quantized using a bit allocation strategy. Advantage is taken from the multiresolution analysis to use different quantizers in each frequency band of wavelet coefficients. Experimental results point out advantages and drawbacks of the approach.

4.1 From Fourier Transform to Wavelets

Let $L^2(\Re)$ denote the Hilbert space of signals having a finite energy

$$L^2(\Re) = \left\{ f, f \text{ is measurable and } \|f\|^2 = \langle f, f \rangle = \int_{-\infty}^{\infty} |f(x)|^2 dx < \infty \right\} \qquad (4.1)$$

where $\langle f, g \rangle = \int_R f(x)\overline{g(x)}dx$ denotes the inner product and $\bar{g}$ is the complex conjugate of g.

The Fourier transform (FT) of a signal $f(x)$ in $L^2(\Re)$ is a decomposition of this signal into sinusoidal waveforms of different frequencies $e_w(x) = e^{2\pi iwx}$,

$$F(w) = \int_R f(x)e^{-2\pi iwx}dx = \langle f, e_w \rangle \tag{4.2}$$

Equation 4.2, when it converges, gives the analysis of f into its frequency components. Although for many applications, working in the frequency domain has been extremely useful and sufficient for the application, the Fourier transform has many drawbacks which are summarized as follows [Kais94]:

(i) Although the reconstruction of the signal is guaranteed from its FT under certain conditions by $f(x) = \int_R \langle f, e_w \rangle e_w(x)dx$, the basis function (e_w) does not belong to $L^2(\Re)$ and the FT does not exist for general $f \in L^2(\Re)$.

(ii) The functions (e_w) are very well localized in frequency domain, however, they are not well time-localized and local features in the time-domain in a signal cannot be easily detected.

(iii) As a consequence of (ii), all time information is needed in the computation of the Fourier transform and this information is lost in the transform domain. Without this time information, an event could be seen in the frequency domain, but no information regarding when it occurred would be available. For *stationary* signals where all frequency components exist at all times, this loss is not important. This loss is, however most severe when we deal with non-stationary signals. As most real-world signals are non-stationary, the FT is then a far less natural tool.

To overcome these drawbacks, a solution was proposed initially by Gabor [Gabo46], giving information about signals simultaneously in the time and the frequency domains. This solution, called the *windowed-Fourier transform* (WFT), consists of windowing the signal f by a weight function g or *window,* to obtain a localized version $f_x(u) = \overline{g(u-x)}f(u)$, then applying the FT,

$$\tilde{f}(w,x) = F_x(w) = \int_R f(u)\overline{g(u-x)}e^{-2\pi iwu}du = \langle f, g_{w,x}\rangle \tag{4.3}$$

where $g_{w,x}(u) = g(u-x)e^{2\pi iwu}$ are the new basis functions. The WFT solves completely the first FT drawback given in (i); in fact, for $g \in L^2(\Re)$, the functions $g_{w,x}$ are in $L^2(\Re)$, and the inner product defining the WFT in Eq. 4.3 is well defined. Concerning the two other drawbacks (ii) and (iii), the WFT gives a partial solution. If g is small outside an interval of length T and its FT, G is small outside an interval of length Ω, then an accurate information about f can be obtained in both time and frequency domain by the WFT. The WFT is then well adapted to the category of non-stationary signals that are stationary in each interval of length T. One can usually let T be infinitely small in order to have a good approximation of the non-stationary signals. The problem with this approach is that infinitely small T implies infinitely large Ω (as $T\Omega \geq \frac{1}{4\pi}$ by the Heisenberg uncertainty principle). Therefore, the time-frequency localization of the WTF has a precision limited to a rectangular area of $T\Omega$, and any features of the signal involving a cell area smaller or greater than $T\Omega$ are either underlocalized or overlocalized.

The wavelet transform addresses this problem of inflexible window sizes by examining the signal using variable sized regions. In wavelet analysis, long time regions

are used where precise low-frequency information is required, and shorter time intervals where high-frequency information is required. Each of these regions allow the signal to be examined at different scales, and thus addresses the problem of uncertainty outlined by Heisenberg. The window regions of the wavelet transform in contrast to the Fourier transform and WFT are shown in Fig 4.1.

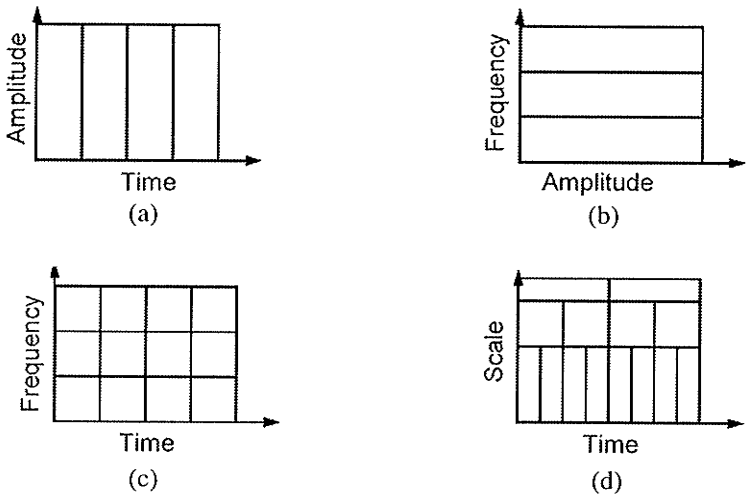

Fig. 4.1 Window shapes for (a) time domain, (b) frequency domain, (c) windowed Fourier transform domain, and (d) wavelet domain (from [MMOP02]).

4.2 The Wavelet Transform

4.2.1 The Continuous Wavelet Transform

As in the FT and the WFT where the signal was decomposed respectively on the basis functions $\{e_w\}_w$ and $\{g_{w,x}\}_{w,x}$, the continuous wavelet transform (CWT) decomposes a signal $f(t)$ using a family of functions $\{\psi_{a,b}, a \in \Re^*, b \in \Re\}$ ($\Re^* = \Re\backslash\{0\}$) generated by a function $\psi(t)$, called *mother wavelet*. Instead of modulation, this family is obtained by *scaling* and shifting given by

$$\Psi_{a,b}(t) = \frac{1}{\sqrt{|a|}}\Psi\left(\frac{t-b}{a}\right) \tag{4.4}$$

and the CWT is defined as

$$\tilde{f}(a,b) = \langle f, \Psi_{a,b}\rangle = \int_{-\infty}^{\infty} \Psi_{a,b}(t) f(t) dt \tag{4.5}$$

The CWT is therefore the correlation of f with ψ shifted by b and scaled by a, as shown in Fig 4.2.

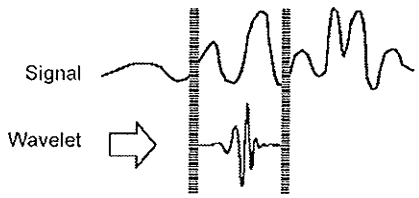

$\tilde{f}(a,b)$

Fig. 4.2 Illustration of the CWT.

Theoretically, there are infinite possibilities for choosing the mother wavelet; every function in $L^2(\Re)$ can be an a priori candidate. However the choice becomes very limited when some constraints are required. The major requirements on the mother wavelets are: (i) in practice, the invertibility of the CWT is needed in order to reconstruct signals from their transform coefficients, and (ii) for the wavelet basis to be interesting, the mother wavelet $\psi(t)$ should be well localized in both time and frequency.

For invertibility, the restriction on the mother wavelet is given by

$$0 < C_\psi = \int_{-\infty}^{\infty} \frac{|\Psi(w)|^2}{w} dw < \infty \tag{4.6}$$

where Ψ is the Fourier transform of ψ. In fact, Eq. 4.6, known as the *admissibility condition*, is sufficient for the reconstruction of the original signal $f \in L^2(\boldsymbol{R})$ by

$$f(t) = \frac{1}{C_\psi} \int_{R^* R} \tilde{f}(a, b) \psi_{a,b}(t) \frac{da db}{a^2} \tag{4.7}$$

The admissibility condition implies that $\Psi(w) \to 0$ as $w \to 0$, then whenever Ψ is continuous at zero, it follows that

$$\Psi(0) = \int_{-\infty}^{\infty} \psi(t) dt = 0 \tag{4.8}$$

Namely, $\psi(t)$ is a "small wave" or "wavelet" representing the impulse response of a bandpass filter in the sense that $\psi(t)$ is an $L^2(\boldsymbol{R})$ function with zero mean.

The CWT is used mainly for mathematical, probabilistic and statistical purposes where properties of functions and stochastic processes can be read from properties of their wavelet transform [Houd94]. However, some applications of the CWT to speech and music analysis [GHKM87], as well as to signal singularities detection [MaHw92] were conducted successfully. To make the wavelet transform more practical, the scaling and shifting parameters can be discretized to give the *discrete wavelet transform* (DWT).

4.2.2 The Discrete Wavelet Transform

Since scaling acts as multiplication, a scale factor $a_0 > 1$ can be fixed, and only scales $a = a_0^m, m \in Z$ can be considered, where Z is the set of all integers. The discrete versions of a and b must be related to each other because if the scale makes the basis

function narrow, then the shifting steps should be correspondingly small, and vice versa. This adjustment to the scale dictates taking $b = nb_0a_0^m, n \in Z$ as discrete time. The discrete wavelet transform (DWT) is then

$$\tilde{f}(m, n) = \langle f, \psi_{m,n} \rangle = \int_{-\infty}^{\infty} \psi_{m,n}(t) f(t) dt \tag{4.9}$$

where $\psi_{m,n}(t) = a_0^{-m/2} \psi(a_0^{-m} t - nb_0^n)$.

Now, there is no guarantee that the admissibility condition in Eq. 4.6 is sufficient for reconstruction since some information is lost by discretizing the coefficients. The ideal case is when the family $\{\psi_{m,n}, m, n \in Z\}$ forms an orthonormal basis for $L^2(\Re)$. In this case one has $\|f\|^2 = \sum_{m,n} |\langle f, \psi_{m,n} \rangle|^2$, and the original signal is recovered by $f(t) = \sum_m \sum_n \langle f, \psi_{m,n} \rangle \psi_{m,n}(t)$. The multiresolution analysis (MRA) not only provides such a basis, but also relates wavelets to filter banks, thus simplifying the use of wavelets in signal processing. The MRA was developed by [Mall89] and will be described in the next section. The class of invertible wavelet transform is not, however, restricted to orthonormal bases. Another class based on the concept of *frames* is very important also and it contains orthonormal bases as a special case. In the following, a brief description of frames is given. For more detail on the subject, the reader is invited to refer to [Kais94], [Mall98], [Daub90], [Lawt90].

A family $\{h_m \in L^2(\boldsymbol{R}), m \in Z\}$ is a frame in $L^2(\boldsymbol{R})$ if there is a pair of constant $0 < A < B < \infty$ such that

$$A\|f\|^2 \le \sum_m |\langle f, h_m\rangle|^2 \le B\|f\|^2, \ \forall f \in L^2(\boldsymbol{R}) \tag{4.10}$$

What is important to notice here is that once Eq. 4.10 is satisfied, then one can construct a family $\{h'_m, m \in Z\}$, called reciprocal family (or basis biorthogonal to $\{h_m\}$, if $\{h_m\}$ is a basis), allowing the recovery of the signal f from the decompositiom $\{\langle f, h_m\rangle\}_{m \in Z}$ by

$$f(t) = \sum_m \langle f, h_m\rangle h'_m(t) \tag{4.11}$$

The frame is self-reciprocal if and only if it is an orthonormal basis, which corresponds to the case $A = B = 1$.

Under the admissibility condition, the continuous wavelet family $\{\psi_{a,b}, a \in \boldsymbol{R}^*, b \in \boldsymbol{R}\}$ is in fact a continuous frame with reciprocal family $\left\{\psi'_{a,b} = \frac{\psi_{a,b}}{a^2 C_\psi}\right\}$, hence the reconstruction in Eq. 4.7. For the discrete family to be a frame and then invertible, a stronger condition is needed.

Let Y_{a_0} be the function defined by

$$Y_{a_0}(w) = (a_0 - 1)\sum_m \left|\Psi(a_0^m w)\right|^2 \tag{4.12}$$

Furthermore, let $\psi \in L^2(\boldsymbol{R})$ be band-limited, with bandwidth Ω. Let $b_0 = 1/\Omega$, and let $0 < A < Y_{a_0}(w) < B < \infty$ for some constants $A, B > 0$ and $a_0 > 1$. Then the family $\{\psi_{m,n}(t) = a_0^{-m/2}\ \psi(a_0^{-m}t - nb_0^n), m, n \in Z\}$ is a frame, and its reciprocal $\{\psi'_{m,n}, m, n \in Z\}$ is the inverse Fourier transform of the family

$$\left\{ \Psi'_{m,n}(t) = \frac{(a_0 - 1)b_0}{Y_{a_0}(w)} \Psi_{m,n}(w),\ m, n \in Z \right\} \text{ so that}$$

$$f = (a_0 - 1)b_0 \sum_{m,n \in Z} \tilde{f}(m,n)\Psi'_{m,n} \tag{4.13}$$

For proof of the above relationship, see [Chui92] or [Kais94].

In image processing, the use of filters with linear phase and with finite impulse response (FIR) is preferable. In fact, phase-linearity means a symmetry in the processing and FIR filters are simpler to implement. The filters associated with an orthogonal wavelet basis are either with linear phase, or with infinite impulse response (IIR) [StNg96], [VeHe92]. The frame theory in general, and the biorthogonal analysis in particular, provide a wavelet basis associated with FIR filters which have linear phase. The price, of course, is the loss of orthogonality and, hence, an increase in the computational complexity.

In practice, the time sampling is fixed at $b_0 = 1$, while the scale factor can be any integer $M \geq 2$. It is called then M-band wavelet bases [GoOB94]. Notice, however, that most of the literature take the case $M = 2$, the two-band (or dyadic) wavelet basis. The main difference between the cases $M = 2$ and $M > 2$ is that in the latter the wavelet basis is generated by more than one wavelet, precisely $(M - 1)$ mother wavelets.

In the rest of the thesis, the time sampling will be fixed at $b_0 = 1$ and the scale factor at $a_0 = 2$.

4.3 Multiresolution Analysis

A multiresolution analysis in $L^2(\Re)$ consists of a sequence of successive approximation spaces $\{V_j, j \in Z\}$ that satisfies the following properties [Mall89]:

$$V_\infty = \{0\} \subset \ldots \subset V_1 \subset V_0 \subset V_{-1} \subset \ldots \subset V_{-\infty} = L^2(\Re) \qquad \text{(M-1)}$$

$$\overline{\lim_{j \to -\infty} V_j} \equiv \overline{\bigcup_{j \in Z} V_j} = L^2(\Re) \text{ and } \lim_{j \to \infty} V_j \equiv \bigcap_{j \in Z} V_j = \{0\} \qquad \text{(M-2)}$$

$$f(x) \in V_j \Leftrightarrow f(x-k) \in V_j \qquad \forall k, j \in Z \qquad \text{(M-3)}$$

$$f(x) \in V_j \Leftrightarrow f(2^j x) \in V_0 \qquad \forall j \in Z \qquad \text{(M-4)}$$

$$\exists \phi(x) \; such \; that \; \{\phi(x-k); k \in Z\} \text{ is an orthonormal basis for } V_0 \qquad \text{(M-5)}$$

The function $\phi(x) \in L^2(\Re)$ is called the *scaling function* and generates, by shifting and scaling, an orthonormal basis $\left\{\phi_{j,n}(x) = 2^{\frac{-j}{2}}\phi(2^{-j}x - n), n \in Z\right\}$ of V_j. The projection of a signal f onto V_j is called an *approximation* of the signal f at *resolution* j (in fact it is a version of f blurred to the scale 2^j) and is given by

$$A_j f = \sum_{n \in Z} \langle f, \phi_{j,n} \rangle \phi_{j,n} \qquad (4.14)$$

Let W_j be the orthogonal complement of V_j in V_{j-1}, i.e,

$$V_{j-1} = V_j \oplus W_j \qquad (4.15)$$

where $\oplus$ denotes a direct sum of spaces.

It was shown [Mall98] that there exists a function $\psi(x)$ such that $\{\psi_{j,n}; n \in \boldsymbol{Z}\}$ forms an orthonormal basis for W_j. The projection of a signal f onto W_j is called the *detail* of f while it is approximated by $A_j f$ at *resolution* j and is then given by

$$D_j f = \sum_{n \in Z} \langle f, \psi_{j,n} \rangle \psi_{j,n} \tag{4.16}$$

It is easy to see from conditions M-1, M-2 and Eq. 4.15, that the family of subspaces $\{W_j; j \in \boldsymbol{Z}\}$ constitutes an orthogonal decomposition of $L^2(\Re)$, i.e.,

$$\bigoplus_{j \in Z} W_j = L^2(\boldsymbol{R}) \tag{4.17}$$

Therefore the wavelet family $\{\psi_{j,n}; j, n \in \boldsymbol{Z}\}$ forms an orthonormal basis for $L^2(\boldsymbol{R})$. This wonderful result allows a perfect reconstruction of the signal from the wavelet coefficients $\{d_n^j = \langle f, \psi_{j,n} \rangle\}_{j,n}$ (also called detail coefficients) by $f = \sum_j \sum_n d_n^j \psi_{j,n}$.

So far two problems, however, can arise in practice. First, the computation of the wavelet coefficients needs an integration. Second, the reconstruction requires an infinite number of coefficients. Fortunately, the MRA gives a solution to these two problems. For the first one, a bridge does exist, thanks to the MRA and Stephan Mallat [Mall89], between *quadrature Mirror Filter* (QMF) and wavelet analysis. In fact, wavelet coefficients-based MRA decomposition as well as the reconstruction from these coefficients can be computed with quadrature mirror filters, consisting of a low-pass filter h and a high-pass filter g. *No* integration is required. This will be the subject of the next two sub-sections. The second problem is treated as follow: from Eq. 4.15, we can write, for any $J > j$

$$A_j f = A_{j+1} f + D_{j+1} f = A_j f + (D_{j+1} f + \ldots + D_j f) \tag{4.18}$$

In practice, it is supposed that the signal f belongs to some V_j (in general V_0) and the decomposition goes from 1 to N (where $N \leq \log_2(length\ of\ f)$). The reconstruction is then

$$f = A_0 f = \sum_{n \in Z} a_n^N \phi_{N,n} + \sum_{j=1}^{N} \sum_{n \in Z} d_n^j \psi_{j,n} \tag{4.19}$$

where $a_n^j = \langle f, \phi_{j,n} \rangle$ are the approximation coefficients.

4.3.1 MRA Analysis Algorithm

From the fact that $\phi(x) \in V_0 \subset V_{-1}$ and $V_{-1} = Span\{\phi_{-1,n}; n \in \mathbf{Z}\}$ there exists $h[n]$, $n \in \mathbf{Z}$ such that

$$\phi(x) = \sum_{n \in Z} h[n] \phi_{-1,n}(x) = \sqrt{2} \sum_{n \in Z} h[n] \phi(2x - n) \tag{4.20}$$

Also, since $\psi(x) \in W_0 \subset V_{-1}$, then there exists $g[n]$, $n \in \mathbf{Z}$ such that

$$\psi(x) = \sum_{n \in Z} g[n] \psi_{-1,n}(x) = \sqrt{2} \sum_{n \in Z} g[n] \psi(2x - n) \tag{4.21}$$

Now, using the definition of a_n^j and combining with Eq. 4.20, the approximation coefficients can be represented as

$$a_n^j = \sum_{k \in Z} h[k] \langle f, \phi_{j-1,k+2n} \rangle \tag{4.22}$$

by substituting $l = k + 2n$, Eq. 4.22 can be expressed as

$$a_n^j = \sum_{l \in Z} h[l - 2n] \langle f, \phi_{j-1,l} \rangle \tag{4.23}$$

but since $\langle f, \phi_{j-1,l} \rangle$ is a_l^{j-1}, therefore

$$a_n^j = \sum_{k \in Z} \tilde{h}[2n - k] a_k^{j-1} \tag{4.24}$$

where $\tilde{h}[n] = h[-n]$. Using the same arguments, the detail coefficients can be obtained from $\tilde{g}[n] = g[-n]$ by

$$d_n^j = \sum_{k \in Z} \tilde{g}[2n - k] a_k^{j-1} \tag{4.25}$$

From Eq. 4.24 and Eq. 4.25, it can be seen that the approximation and the detail coefficients at resolution j can be obtained from the approximation coefficients at resolution $j-1$ by simply filtering by h or g and then downsampling by two. That is the MRA analysis algorithm and is shown on Fig. 4.3

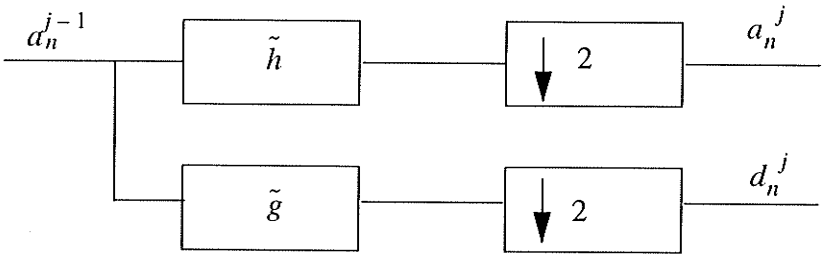

Fig. 4.3 MRA analysis algorithm.

4.3.2 MRA Synthesis Algorithm

For reconstructing the original signal from the transform coefficients, one needs to know only how to come back from coefficients at resolution j to coefficients at resolution $j-1$. Using a similar argument as the MRA analysis algorithm, the MRA synthesis algorithm is

$$a_n^{j-1} = \sum_k h[n-2k]a_k^j + \sum_k g[n-2k]d_k^j \tag{4.26}$$

$$d_n^{j-1} = \sum_k g[2n-k]d_k^j \tag{4.27}$$

The MRA synthesis algorithm is depicted in Fig. 4.4.

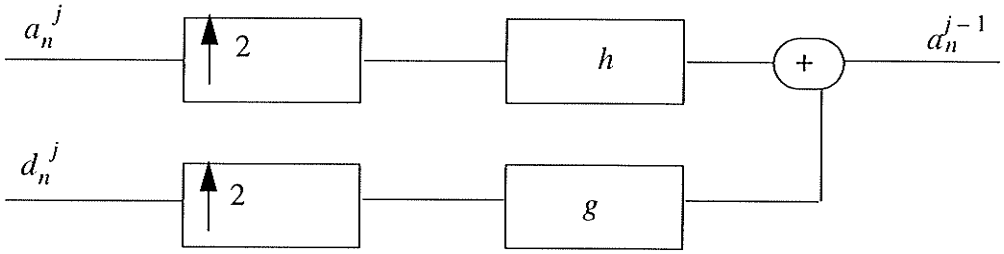

Fig. 4.4 MRA synthesis algorithm.

4.3.3 Properties of MRA

Some necessary conditions of the multiresolution analysis are very important in the construction of a wavelet basis associated with an MRA. In the following, the properties of ϕ, ψ, h, g and their respective Fourier transform Φ, Ψ, H and G are summarized.

From the MRA assumptions on $\{V_j\}$ and $\{W_j\}$, the following orthogonality conditions on ψ and ϕ can easily be deduced [Truc98], [Mall97]

$$\begin{cases} \langle \phi_{j,n}, \phi_{j,m} \rangle = \delta_{n,m} \\ \langle \phi_{j,n}, \psi_{j,m} \rangle = 0 \\ \langle \psi_{j,n}, \psi_{l,m} \rangle = \delta_{j,l}\delta_{n,m} \end{cases} \tag{4.28}$$

Equivalent orthonormality conditions on Fourier domain can also be obtained by taking the Fourier transform of the first and third equalities on Eq. 4.28

$$\sum_n |\Phi(w + 2\pi n)|^2 = \sum_n |\Psi(w + 2\pi n)|^2 = 1 \tag{4.29}$$

Now, taking the Fourier transform in both Eq. 4.20 and Eq. 4.21, one finds

$$\begin{cases} \Phi(w) = \frac{1}{\sqrt{2}} H\left(\frac{w}{2}\right)\Phi\left(\frac{w}{2}\right) \\ \Psi(w) = \frac{1}{\sqrt{2}} G\left(\frac{w}{2}\right)\Phi\left(\frac{w}{2}\right) \end{cases} \tag{4.30}$$

which allows the construction of ϕ and ψ from h and g.

The following equation confirms that h is a low-pass filter and g is a high-pass filter

$$\begin{cases} H(0) = \sum_n h(n) = \sqrt{2} \text{ and } |H(\pi)| = 0 \\ G(0) = \sum_n g(n) = 0 \text{ and } |G(\pi)| = \sqrt{2} \end{cases} \tag{4.31}$$

This corresponds to the fact that the passage from an approximation to the next coarser approximation consists on eliminating details (or high frequencies).

The high-pass filter g is related to the filter h through

$$G(w) = \lambda(w)\overline{H(w+\pi)} \tag{4.32}$$

where λ is $2\pi-$ periodic such that $\lambda(w)+\lambda(w+\pi)=0$ and $|\lambda(w)| = 1$. In general λ is chosen (for a simpler implementation) to be $\lambda(w) = e^{-iw}$ so that g is given by

$$g(n) = (-1)^n h(1-n) \tag{4.33}$$

4.4 Application to SAR

Since the introduction of the MRA, a lot of importance has been given to the application of wavelets in signal and image processing. This growing popularity of wavelets has led several researchers to take an interest in applying wavelets to SAR data. Most of the authors have applied wavelets either to SAR image compression [WeWC94], [Baxt99], or to SAR image speckle filtering [FoBB01], [GaSm96], and only a few applications to raw SAR data can be found in the literature. In [PaSc99], the authors have used wavelets to compress the raw SAR data. Their approach consisted in compressing the entire data frame at once, and then thresholding the coefficients. The insignificant coefficients are quantized to zero, while the significant coefficients are quantized uniformly. To test the performance, they provide the SQNR results only in the image domain, and not in the signal domain. As the entire data frame does not have to be stored in memory before the compression can begin, an alternative approach is proposed here by

applying wavelets to blocks of data, and adapting the quantization to the specifics of each block, thereby creating the new wavelet-BAQ.

4.4.1 2-D MRA

A particular two-dimensional signal will be presented by $I(x, y)$ at every point (x, y) in the screen. For normalization convenience, the work will be over the global contrast $C(x, y) = I(x, y) - I$ where I is the average over the screen [ETHB02]. This is very convenient as wavelets have zero-mean for mathematical reasons [Daub92], and the goal is to express C as a combination of wavelets.

A separable 2-D dyadic wavelet expansion is considered here. Thus, for a given (1-D) *multiresolution analysis* (MRA) determined by a scaling function φ and the associated wavelet ψ, the corresponding 2-dimensional MRA is determined by the scaling function Φ and the three mother wavelets Ψ^0, Ψ^1, Ψ^2 given by [Truc98]

$$\begin{cases} \Phi(x, y) = \varphi(x)\varphi(y) \\ \Psi^0(x, y) = \varphi(x)\psi(y) \\ \Psi^1(x, y) = \psi(x)\varphi(y) \\ \Psi^2(x, y) = \psi(x)\psi(y) \end{cases} \tag{4.34}$$

The horizontal, vertical and diagonal details, at resolution j, are obtained as the inner product of the signal C with a shifted and dilated version of $\Psi^i, i = 0, 1, 2$, respectively, i.e.,

$$\alpha^i_{j,k,m} = \langle C, \Psi^i_{j,k,m} \rangle, \text{ for } i = 0, 1, 2 \tag{4.35}$$

and the approximation of the signal, at resolution j, is given by

$$\beta_{j,k,m} = \langle C, \Phi_{j,k,m} \rangle \tag{4.36}$$

where $\Phi_{j,k,m}(x, y) = 2^j \Phi(2^j x - k, 2^j y - m)$ and $\Psi^i_{j,k,m}(x, y) = 2^j \Psi^i(2^j x - k, 2^j y - m)$.

The greatest scale is fixed as the unity $1 = 2^0$ (i.e., the corresponding approximation and details are a single point) and the jth scale is then 2^{-j}. Assuming that the scale is of the same order as the dispersion of the wavelet, it is possible to distinguish up to 2^{-2j} different blocks. If the smallest scale is denoted by N (which corresponds to the original signal), then the reconstruction of C is given by

$$C(x, y) = \sum_{j=0}^{N} \sum_{k,m=0}^{2^j - 1} \sum_{i=0}^{2} \alpha^i_{j,k,m} \Psi^i_{j,k,m}(x, y) \tag{4.37}$$

In this decomposition (in which the coarsest approximation is neglected), the signal is represented in successive levels of details, from the coarsest to the finest details.

The implementation is as follows: the rows of the input block C are first filtered with h then with g. The filtered output is then down-sampled by 2. Next each column of the row filtered block is again low-pass and high-pass filtered and down-sampled by 2. This is the first level decomposition. The same process is applied to the *hh*-output recursively to obtain the second level decomposition, and the process continues up to the desired resolution.

4.4.2 Wavelet Bases

To conduct the experiment, five orthonormal wavelet bases have been used, namely *Haar wavelet* (HW), the linear and quadratic splines from *Battle-Lemarié* wavelets (BLL and BLQ) which are constructed by orthogonalizing the B-spline functions, and two Daubechies wavelets (D4 and D20). The corresponding mother wavelets in 1-D together with their spectra are plotted in Fig 4.5.

As it can be seen, the Haar wavelet provides better localization in the spatial domain compared to the Battle-Lemarié ones. However, the opposite is true in the frequency domain. A better trade-off between spatial and spectral localization is provided by Daubechies wavelets. Other important properties like symmetry, number of vanishing moments and regularity can be fruitful for data compression. It was established that [Mall98]:

(a) If the wavelet has enough vanishing moments, then the wavelet coefficients are small at fine scales and can be neglected in a compression application. Haar wavelet has only one vanishing moment, BLL and D4 have two, BLQ has three while D20 has ten vanishing moments.

(b) To minimize the number of high amplitude coefficients (which improves the compression), we must reduce the support size of the mother wavelet. Daubechies wavelets have a minimum size support for a given number of vanishing moments.

(c) The regularity of the mother wavelets influences the quantization distortion of the coefficients. Regularity increases with the number of vanishing moments. Haar

wavelet is discontinuous, D4 is Lipshitz 0.55, BLL is continuous, BLQ and D20 are continuously differentiable.

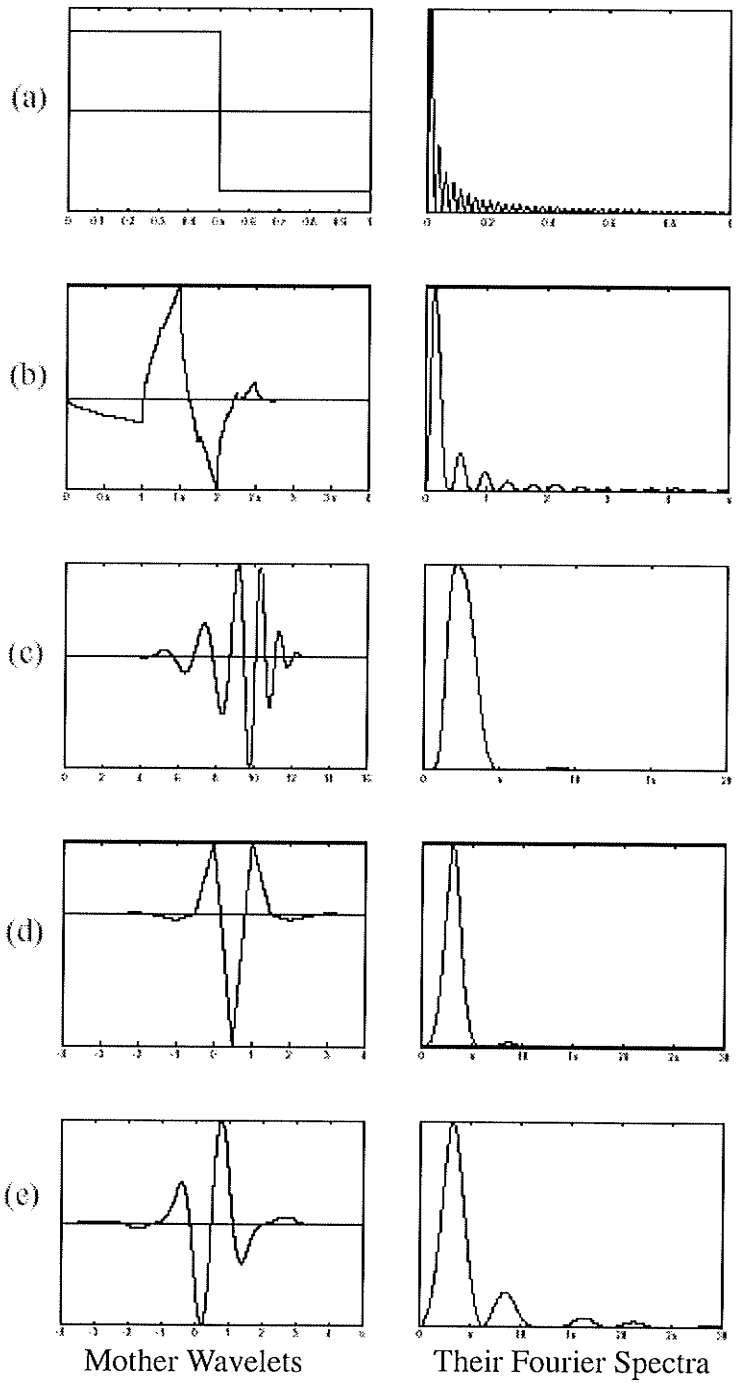

Fig. 4.5 The mother wavelets and their spectra. (a) HW, (b) D4, (c) D20, (d) BLL and (e) BLQ.

4.4.3 Experimental Results

To test the performance of the five kinds of wavelets, the set E1-22089R of the ERS-1 mission was considered. This data frame, of 26624 x 11264 samples in azimuth and range directions, was provided by the *Alaska SAR Facility* (ASF). For the evaluation, the *signal-to-noise ratio* (SNR) which is the ratio of the original raw data variance to the variance of the error between the original and reconstructed data was considered. This error is the same as the quantization error, as long as orthogonal transforms are considered.

Figure 4.6 presents two parts of the original image compared to the corresponding reconstructed ones (for a quantization with 2 bits) obtained after processing the raw data. These two parts were chosen because of their representative features (mountains, river, lake, airport). As it can be seen from the error images amplified by 37% shown in Fig. 4.7, the reconstructions are of high quality, without any recognizable residual pattern. Notice also that there is no significant perceptual difference with respect to the kind of wavelets used.

The wavelet-BAQ results in Table 4.1 are compared with BAQ. The table shows the SQNR (in dB) for a quantization with 1, 2, or 3 bits per sample. These results show no significant difference from basis to basis and no improvement over BAQ, as their SQNR performance remains about the same at all bit levels. This is due to the characteristics of the raw SAR data which are similar to noise. Nevertheless, this analysis uncovered several clues that further improvement could be obtained by searching for an optimal wavelet capable of localizing the important object better.

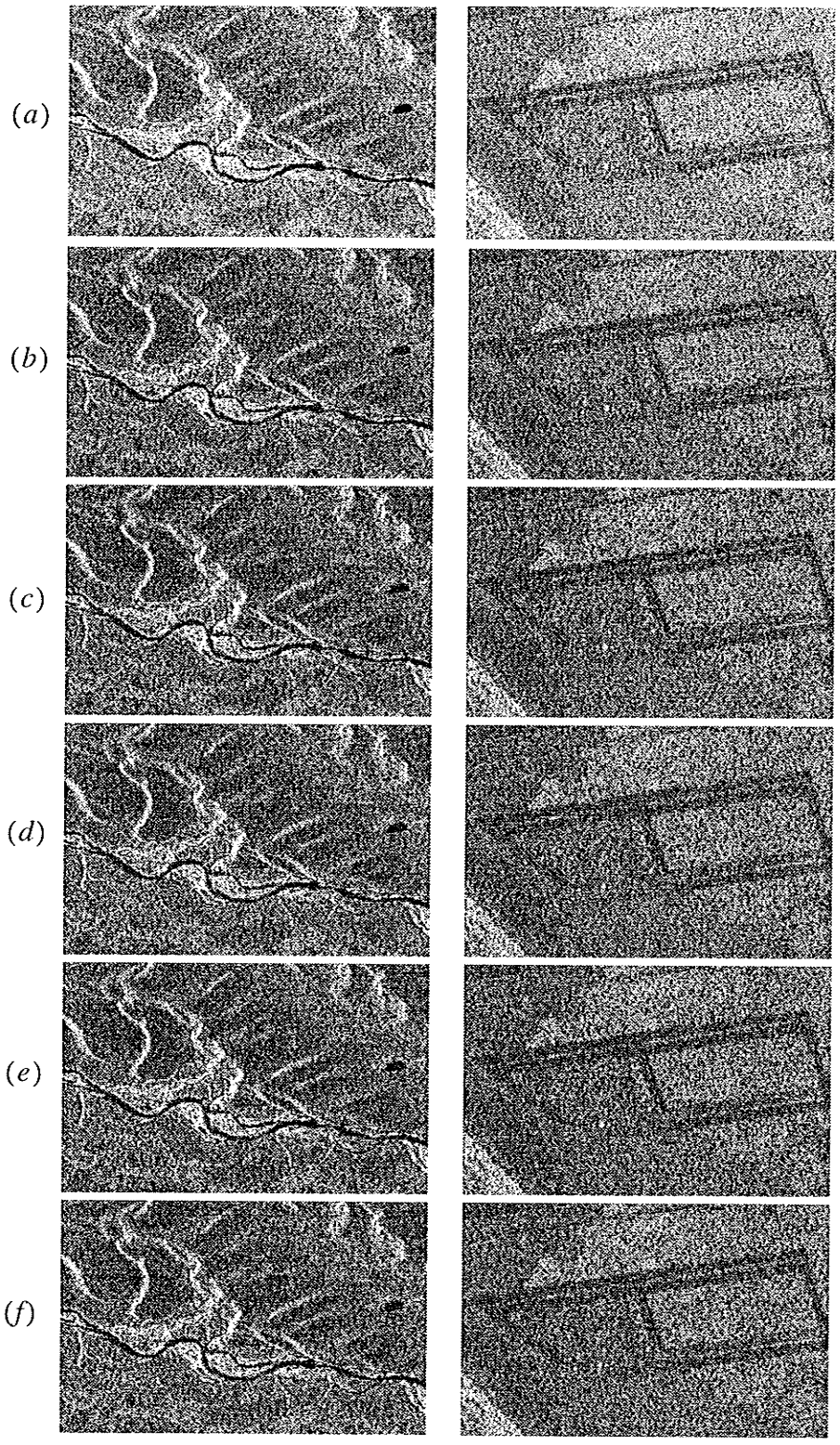

Fig. 4.6 (a) Original image, and reconstructed images using (b) HW, (c) BLL, (d) BLQ, (e) D4 and (f) D20.

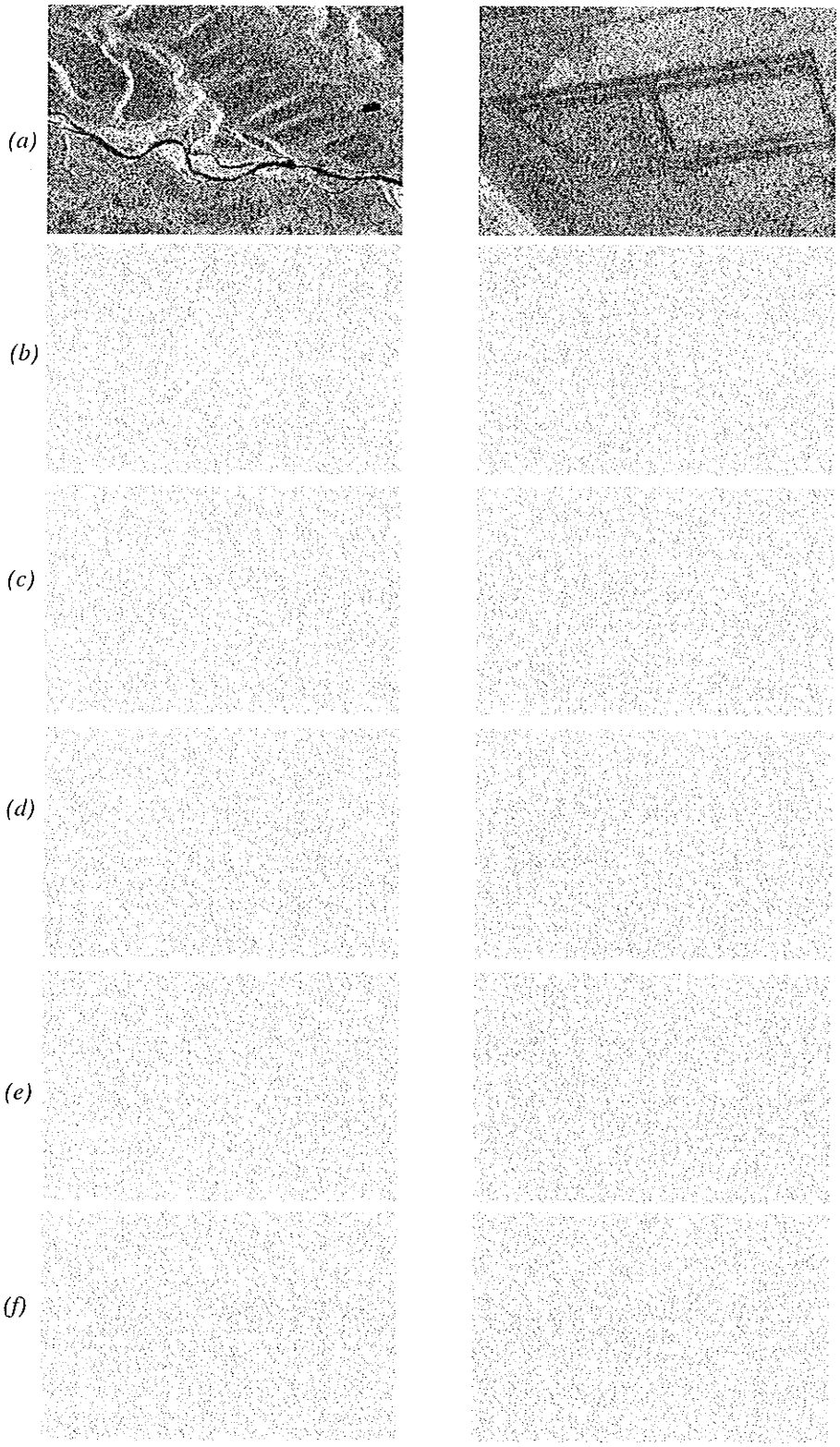

Fig. 4.7 (a) Original image, and error images using (b) HW, (c) BLL, (d) BLQ, (e) D4 and (f) D20.

Table 4.1: SQNR of BAQ and wavelet-BAQ.

bits/ sample	SQNR [dB]						Shannon Bound
	BAQ	Wavelet-BAQ					
		Haar	BLL	BLQ	D-4	D-20	
1	4.39	4.35	4.35	4.35	4.36	4.35	6.02
2	9.30	8.14	8.01	8.00	8.01	8.00	12.04
3	14.61	14.55	14.52	14.59	14.53	14.50	18.06

4.5 Summary

In this chapter, wavelet transform was applied to raw SAR data compression. The wavelet transform decomposes a signal using scaled and shifted versions of a single function. The multiresolution analysis technique for the discrete wavelet transform provides an orthonormal basis permitting a perfect reconstruction of signals from their transform coefficients. The MRA also relates wavelets to filter banks, thus allowing fast computation of the wavelet coefficients.

The goal of studying wavelet-based techniques and their effect on raw SAR signal have been achieved. The quality of the reconstruction is good; however, further improvement of the SNR has to be made. Due to noise like characteristics of the raw SAR signal, the standard wavelets are not very efficient in compacting energy in the transform domain. Hence, research has to be oriented to wavelet optimality, combined with an efficient quantization strategy. This is the subject of the next chapter.

CHAPTER V

WAVELET PACKETS AND OPTIMAL WAVELETS

In the previous chapter, it was concluded that standard wavelet transforms are not very efficient for raw SAR data compression. This chapter provides a formalism leading to the derivation of a 2-D optimal wavelet which minimizes the transform coefficients correlation. The chapter begins by presenting a brief review of the wavelet packet in both 1-D and 2-D. Experimental results with a wavelet packet and the optimal wavelet follow.

5.1 Wavelet Packets

While the wavelet decomposition produces signal components whose spectra consist of consecutive octave bands, the wavelet packet decomposition provides a finer spectral resolution. This generalization can be beneficial in certain applications. Coifman, Meyer and Wickerhauser [CoMW92] showed that conjugate mirror filters transform an orthogonal basis in two orthogonal bases (or in four orthogonal bases for 2-D).

5.1.1 1-D Wavelet Packet

In the passage from resolution j to resolution $j+1$, the wavelet-packet transform (WPT) decomposes not only the approximation subspaces V_j but also the detail subspaces W_j. This is based on a mathematical theorem attributed by Mallat to Coifman, Meyer and Wickerhauser [Mall98], but it is attributed to Daubechies in [GoCh99]. This theorem states that from the orthonormal basis $\{\psi_{j,n}; n \in Z\}$ of W_j, another orthonormal basis $\{\psi'_{j+1,n}, \psi''_{j+1,n}; n \in Z\}$ of W_j can be constructed by

$$\begin{cases} \psi'_{j+1}(x) = \sum_k h[k]\psi_{j,k}(x) \\ \psi''_{j+1}(x) = \sum_k g[k]\psi_{j,k}(x) \end{cases} \tag{5.1}$$

It follows that the detail space W_j can be decomposed in two complementary subspaces $W'_{j+1} = span\{\psi'_{j+1,n}; n \in \mathbf{Z}\}$ and $W''_{j+1} = span\{\psi''_{j+1,n}; n \in \mathbf{Z}\}$; i.e,

$$W_j = W'_{j+1} \oplus W''_{j+1} \tag{5.2}$$

This decomposition is, in fact, a generalization of the decomposition of V_j into V_{j+1} and W_{j+1} and by unifying the notations, both decompositions of V_j and W_j can be treated at once. By setting $W_0^0 = V_0$ and $\psi_0^0 = \varphi$, where φ is the scaling function, then the subspace $W_j^p = span\{\psi_{j,n}^p ; n \in \mathbf{Z}\}$ is decomposed by

$$\begin{cases} \psi_{j+1}^{2p}(x) = \sum_n h[n]\psi_{j,n}^p(x) \\ \psi_{j+1}^{2p+1}(x) = \sum_n g[n]\psi_{j,n}^p(x) \end{cases} \tag{5.3}$$

Figure 5.1 illustrates the WPT decomposition. Note, however, that there is no need to decompose every detail subspace. If one decides to decompose (e.g., W_1^1), a collection of orthonormal bases is then possible. In [CoWi92], the authors developed an entropy-based algorithm for best-basis selection.

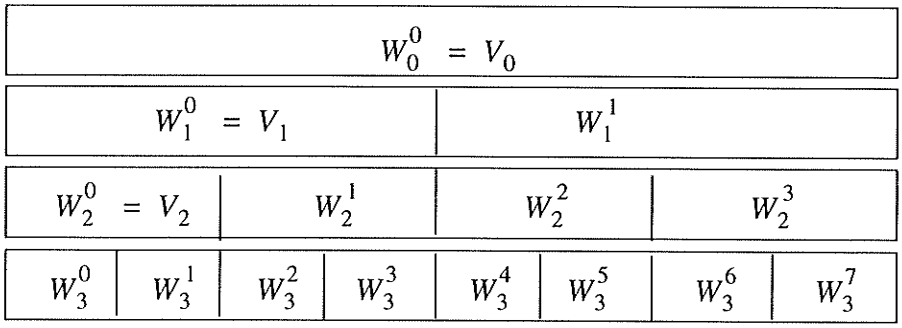

Fig. 5.1 Wavelet packet decomposition.

5.1.2 2-D Wavelet Packets

A separable two-dimensional (2-D) dyadic wavelet packet expansion, in which the 2-D wavelet packet bases are tensor products of the 1-D wavelet packet bases is considered

$$\psi_{j,k,m}^{p,q}(x,y) = \psi_{j,k}^{p}(x)\psi_{j,m}^{q}(y) \tag{5.4}$$

Therefore, the 2-D algorithm repeats the 1-D algorithm first in the x-direction and then along the y-direction. Also, the implementation of the 2-D wavelet packet algorithm is similar to that of the 2-D wavelet algorithm. Here, not only is the approximation (hh) component decomposed to obtain further details of the image, the other wavelet components (hg, gh, gg) are also decomposed.

5.2 Optimal Wavelet Basis

Although wavelet packets are very useful in optimizing the decomposition into individual wavelets, the wavelets themselves may not be optimal. This section addresses the important topic of optimality of wavelets.

The problem of deriving the optimal wavelet representation of signals has specific application to signal detection, enhancement, compression, and target detection. Many algorithms for designing wavelets to match a specified signal have been developed, [TeSJ92], [MaZh93], [AlUn93], [ChDo94], [GoOB94], [Swel96], [ChRa00]. An overview of the wavelet optimality shall be first presented, then a formalism which leads to an optimal wavelet for raw SAR data compression is presented.

5.2.1 An Overview

The construction of standard wavelets requires solving the equations obtained as a necessary condition of a multiresolution analysis (like Daubechies wavelets), or orthogonalizing some existing bases like (*B*-spline). The resulting wavelets are then independent of the signal to be analyzed. In finding optimal wavelets, another cost function is added to the MRA constraints and the wavelet is related to the signal itself. This cost function depends on the application. In [TeSJ92] for example, the authors found an optimal representation of a given signal f at any prescribed resolution J by minimizing the error

$$e = f - \sum_{k \in Z} \langle f, \varphi_{J,k} \rangle \varphi_{J,k} = \sum_{j=J+1}^{\infty} \sum_{k \in Z} \langle f, \psi_{j,k} \rangle \psi_{j,k} \tag{5.5}$$

Gopinath *et al.*, in [GoOB94] extended this optimal representation to M-band wavelets, leading to a *wavelet sampling theorem* generalizing the Shannon sampling theorem by showing that the scaling expansion coefficients $\{\langle f, \varphi_{J,k}\rangle; k \in \mathbf{Z}\}$ uniquely determine the band limited signal f, under some conditions on φ.

Recently, Chapa and Rao [ChRa00] designed a wavelet that matches a signal of interest such that the output of the matched filter bank is maximized. By seeking a wavelet whose scaled and shifted versions have the same spectrum as the signal; i.e., $\Psi_{j,n}(2^j w) = KF(w)$; the wavelet coefficients are then equal to their possible maximum values

$$d_n^j = \langle f, \psi_{j,n}\rangle = \|F\|^2 \left\|\Psi_{j,n}(2^j)\right\|^2 \tag{5.6}$$

thus making the signal detection more efficient.

5.2.2 Optimal Wavelet for SAR Data Compression

In [TMPN97] and [TuPa00], the authors derived optimal representation for natural images able to separate independent features at a different resolution level. Following their approach, a mother wavelet is determined. It is learned statistically from raw SAR data in order to derive a redundancy reducing wavelet basis. The redundancy between wavelet coefficients at different scales should be minimized.

The notation of Ch. 4 is used here. It was established that, for natural images, there exists a multiplicative stochastic process η such that [BuSi99], [TMPN97]

$$\alpha_{j,k,m}(\omega) \tag{5.7a}$$

and

$$\eta_{j,k,m}(\omega)\alpha_{j-1,\left\lfloor\frac{k}{2}\right\rfloor,\left\lfloor\frac{m}{2}\right\rfloor}(\omega) \tag{5.7b}$$

have the same distribution. The equality is required to hold point by point, for any sample, any scale and any position; i.e.,

$$\alpha_{j,k,m}(\omega) = \eta_{j,k,m}(\omega)\alpha_{j-1,\left\lfloor\frac{k}{2}\right\rfloor,\left\lfloor\frac{m}{2}\right\rfloor}(\omega) \tag{5.8}$$

Also the following conditions on the variables $\eta_{j,k,m}$ are assumed

(i) to be independent of each other, and to be independent from $\alpha_{j-1,\left\lfloor\frac{k}{2}\right\rfloor,\left\lfloor\frac{m}{2}\right\rfloor}$

(ii) to have the same distribution for all resolution levels j and spatial location (k, m).

By averaging Eq. 5.6 over the data, and using the conditions above, it follows that

$$\bar{\alpha}_{j,k,m} = \bar{\eta}^{j}\bar{\alpha}_{0,0,0} \tag{5.9}$$

where $\bar{\alpha}$ and $\bar{\eta}$ are the means over the data.

Now, averaging the reconstruction formula over the data, given by Eq. 4.37 (Ch. 4), and applying Eq. 5.7, we find

$$C(x,y) = \bar{\alpha}_{0,0,0}\sum_{j=0}^{N}\sum_{k,m=0}^{2^{j}-1}\bar{\eta}^{j}\psi_{j,k,m}(x,y) \tag{5.10}$$

where ψ is the assumed optimal wavelet.

By taking the Fourier transform in Eq. 5.8, the optimal wavelet is given in the Fourier domain by

$$\Psi(f_1,f_2) = \frac{1}{\bar{\alpha}_{0,0,0}}\left[\hat{C}(f_1,f_2) - \frac{\bar{\eta}}{4}\frac{\Lambda(f_1,f_2)}{\Lambda\left(\frac{f_1}{2},\frac{f_2}{2}\right)}\hat{C}\left(\frac{f_1}{2},\frac{f_2}{2}\right)\right] \tag{5.11}$$

where $\Lambda(f_1,f_2) = (1-e^{-2\pi i f_1})(1-e^{-2\pi i f_2})$ and $\hat{C}$ is the Fourier transform of C.

5.3 Experiments and Results

5.3.1 Wavelet Packet

The Haar wavelet, as well as D4 and D20 from Daubechies wavelet family, were used to compute the wavelet packet decomposition of the raw SAR signal. As mentioned above, each single wavelet packet decomposition gives a collection of bases. It can be shown that there are more than $2^{n^2/4}$ wavelet packet bases for a given block of n^2 pixels. The entropy-based algorithm for best-basis selection developed in [CoWi92] is adapted here. It searches for a best basis that minimizes the Shannon entropy. The search using this algorithm is fast, however it does not guarantee the optimality in the rate-distortion sense. The algorithm was implemented in Matlab 6.5.

Table 5.1 presents the SQNR results obtained when using the wavelet packet algorithms. Table 5.2 presents the SQNR results for the same wavelet bases but using the wavelet transform as well as BAQ. Both tables are presenting results on the data set E1-22089R.

Table 5.1: SNR for wavelet packet using 1 or 2 bits.

Rate [bits/sample]	SNR [dB]		
	Haar	D4	D20
1	5.21	5.02	4.97
2	9.39	9.26	9.20

Table 5.2: SQNR of BAQ and wavelet.

Rate [bits/sample]	SQNR [dB]			
	BAQ	Wavelet-BAQ		
		Haar	D4	D20
1	4.39	4.35	4.36	4.35
2	9.30	8.14	8.01	8.00

It can be seen that the wavelet packet outperforms the wavelet transform in compressing raw SAR data. This is due in part to the ability of the optimal wavelet packet basis to compact the signal energy with a few coefficients.

5.3.2 Optimal Wavelet

A set of 1024 patches of size 512 x 512, taken from the data sets E1-2208P and E2-5551P was used to evaluate the optimal wavelet from Eq. 5.9. After normalization (i.e., dividing each pixel by the total energy), the wavelet obtained is shown in Fig. 5.2 where, for comparison, the vertical Haar wavelet and a frame from raw SAR data set are included.

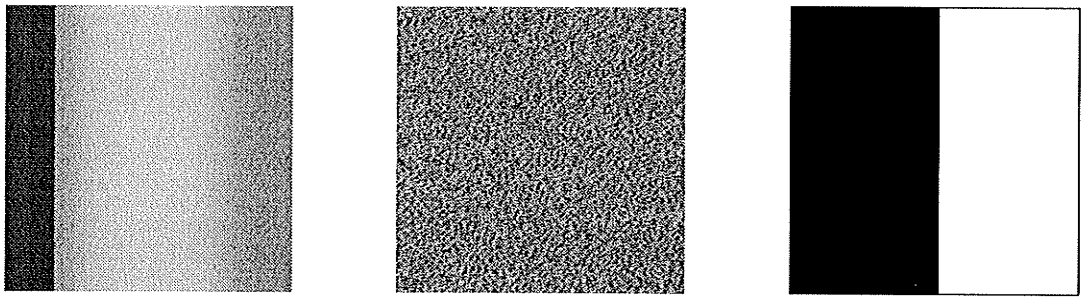

(a) (b) (c)

Fig. 5.2 (a) Optimal wavelet, (b) raw SAR data, and (c) Vertical Haar wavelet.

Two main observations can be made from Fig. 5.2. The first is that, like the vertical Haar wavelet, the optimal wavelet looks like an edge detector. Since there are two main strong transitions, the corresponding wavelet coefficients will be greater around the area with sharp transition and smaller over the smooth regions. The second observation is that unlike the Haar wavelet, the optimal wavelet seems to be well adapted to the raw data. This property is crucial for a better localization of objects within the data.

It was confirmed in many studies that the wavelet transform is capable of compacting the energy (and then performing a good compression) for images belonging to the $1/f$ family, whose power spectrum (the Fourier transform of the correlation) drops whith increasing frequency [Kesh82]. Although SAR data are in the $f^{-\beta}$ family, its power spectrum does not drop as fast as in optical images. It is one of the reasons why wavelet transforms are not very efficient in compressing the SAR signal, as it was pointed out in Ch. 4. Taking this observation into account, the computation of ψ_j^{op}, which is the j^{th} scaled version of the optimal wavelet denoted ψ^{op}, should be adapted. Therefore, contrary to optical images, there is no need to keep the $1/f$ dependance in Fourier domain at each scale. Note that the resulting optimal wavelet is a matrix with a size equal to the

size of the blocks; i.e., 512 x 512, and therefore the multiresolution analysis cannot, unfortunately, be applied for wavelet coefficient computation. A direct evaluation, using the correlation between ψ_j^{op} and each block of the raw data set, has to be performed. At each scale j, the scaled version ψ_j^{op} of ψ^{op} is obtained by first averaging over $2^j \times 2^j$ blocks of the Fourier transform of ψ^{op}, then zero-padding up to 512×512, and finally applying the inverse Fourier transform.

Although the resulting optimal wavelet basis is nearly orthogonal, it is not complete; i.e., the family $\{\psi_{j,n,m}^{op}, j,n,m\}$ is not a basis for $L^2(\Re^2)$. Therefore, a comparison with the standard wavelet bases has no meaning, as the latter generates complete bases. Instead, a comparison with the vertical Haar wavelet is proposed.

Figure 5.3 presents parts of the original images from the data sets E1-2208P and E2-5551P and the reconstructed images using both the optimal wavelet and the vertical Haar wavelet. The images are obtained by wavelet transforming first and processing the raw data afterwards.

Table 5.2 presents the SQNR (in dB) using the optimal wavelet and the vertical Haar wavelet for a quantization with 1 or 2 bits per sample.

Table 5.3: SQNR in dB for the optimal and the vertical Haar wavelets using 1 or 2 bits.

Rate [bits/sample]	SQNR [dB]	
	Haar (vertical)	Optimal wavelet
1	2.21	3.52
2	5.42	6.04

It can be seen from both images and SQNR values that the optimal wavelet performs better than the vertical Haar wavelet. This confirms the ability of this optimal wavelet in decorrelating the wavelet coefficients at different scales. Of course, the description is not complete since the reconstruction is far from being a good approximation, as shown in Fig. 5.3. This is also the case when only one orientation from the Haar basis is taken. An examination of the Haar basis shows that other orientations can be obtained from the vertical orientation.

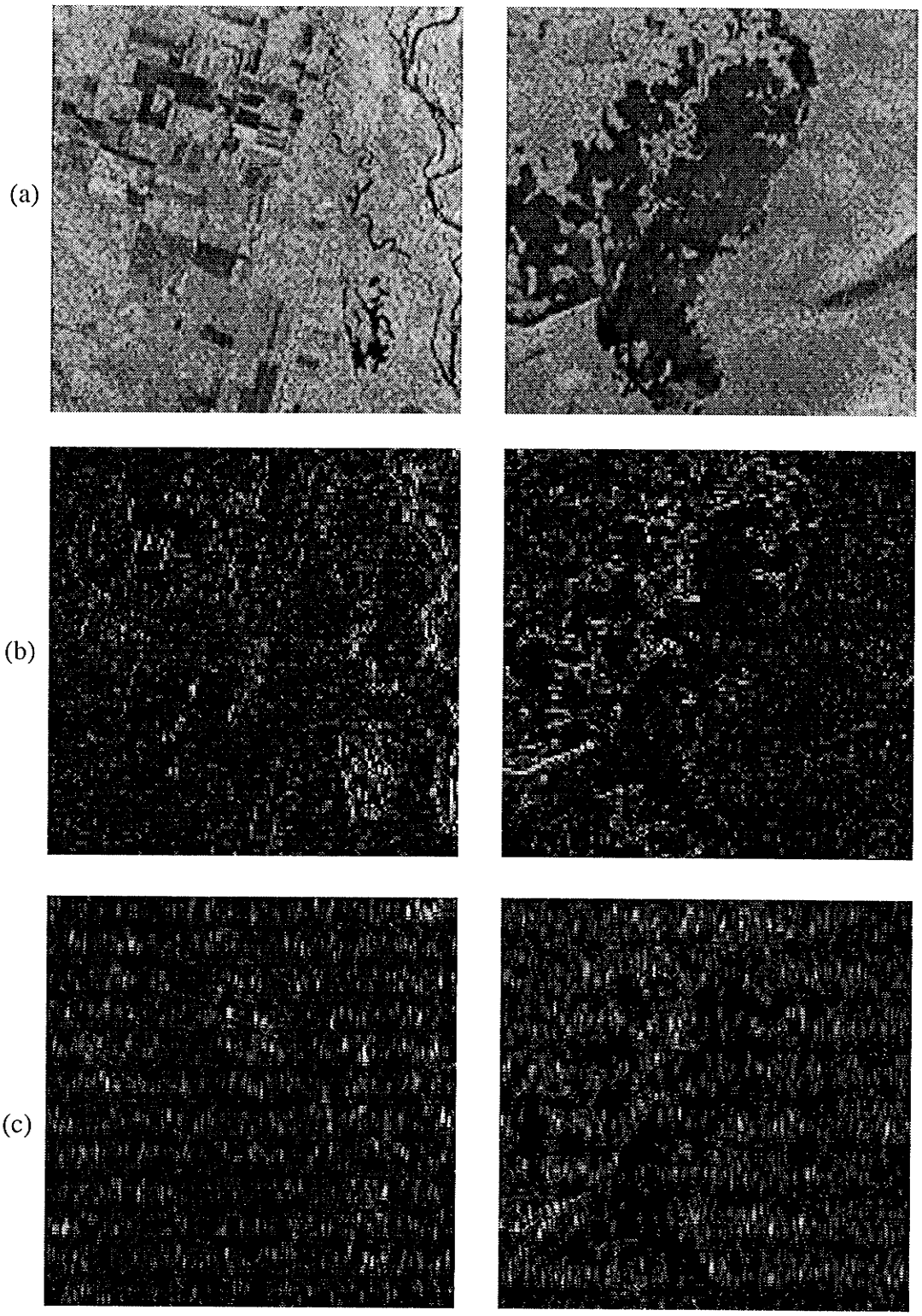

Fig. 5.3 (a) Original images, (b) Reconstructed images using the optimal wavelet and 5 scales, and (c) reconstructed images using the vertical Haar wavelet and 5 scales.

Figure 5.4 suggests that the three orientations can be related by transformations which are a combination of rotations, scaling and translations. The introduction of new orientations is necessary for a complete reconstruction.

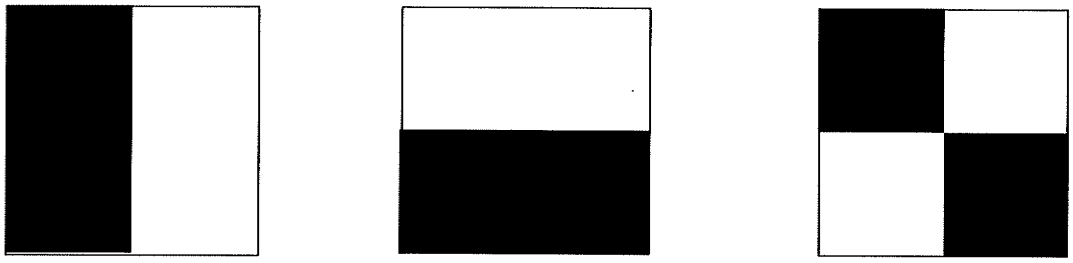

Fig. 5.4 Haar mother wavelets.

5.4 Summary

This study presented a compression of the raw SAR signal using an optimal wavelet estimated from given data and using standard wavelet packet tree. The optimal wavelet gave better results than the vertical Haar wavelet. There is, however, a lack of completeness as the optimal wavelet provides only one orientation. This lack can be addressed by introducing new orientations of this optimal wavelet.

The investigation of wavelets presented in the last two chapters cannot be complete without application to SAR image segmentation and feature extraction. The capabilities of wavelets are not limited to compression but they have been proven to be a good tool for singularity detection and multifractal characterization. This is the subject of the next two chapters.

CHAPTER VI

FRACTALS AND MULTIFRACTAL ANALYSIS

Benoit Mandelbrot defined a *fractal* as a set for which the Hausdorff-Besicovitch dimension (dafinition at Eq. 6.4) strictly exceeds the topological dimension [Mand82]. In an attempt to understand the Mandelbrot definition, this chapter begins by presenting some of the "monster" objects which cannot be handled by the Euclidian geometry. Then, it overviews some of the many fractal dimensions (and then definitions) elaborated in the recent decades with the objective of characterizing such objects [Kins94a][Kins94b]. When dealing with natural signals, images, or objects in general, a multifractal analysis is crucial [Hart91]. The theory behind multifractal measures and singularity spectrum is provided and the role of wavelets in measuring the local regularity of signals is underlined [MaHw92], [Mall98]. Iterated function systems (IFS) offer the possibility of high rates of data compression that can reach 10 000:1 [BaSl88], and furthermore, they allow also the fractal dimension estimation. This chapter is ended by an overview of the basic theory behind iterated function systems (IFSs).

6.1 Fractals

Within the framework of the Euclidean geometry, shapes are generally represented in terms of squares, circles, triangles, parabolas, and other simple curves. Signals (or signals under magnification) are assumed to be as smooth as possible, continuous and differentiable. Unfortunately, nature is too complex to be modeled by these regular shapes. Curves which are everywhere continuous but nowhere differentiable were pointed out at

the early 1900s, but remained intractable. Almost all the natural objects such as trees, rivers, coastlines, mountains, and lightning present an extremely irregular shape that cannot be described by the Euclidean geometry. A new geometry which is capable of describing complex objects either theoretical or natural, was born by the introduction of the concept of Fractal in 1975 [Mand82]. Fractal geometry, which was popularized by Mandelbrot, provides a tool for describing complex structures in a way that conventional techniques cannot. Central to fractal geometry is the concept of *self-similarity.* A set is self-similar if it is the union of a number of smaller copies of itself, i.e., it is invariant under a collection of similarities. Fractals challenged the assumption of rectifiability with the hypothesis of self-similarity [Ning97].

6.1.1 Fractal Objects

An *initiator* and a *generator* are necessary for the generation of a strict fractal object. Although the objects to be presented in this section demonstrate certain complexity, it will be seen that they can be achieved from very simple rules.

Cantor Set

Beginning by the unit interval $I_0 = [0, 1]$ as initiator, Cantor removed the middle third $(\frac{1}{3},\frac{2}{3})$ to obtain $I_1 = \left[0, \frac{1}{3}\right] \cup \left[\frac{2}{3}, 1\right]$. Removing again the middle thirds of both intervals, yields $I_2 = \left[0, \frac{1}{9}\right] \cup \left[\frac{2}{9}, \frac{1}{3}\right] \cup \left[\frac{2}{3}, \frac{7}{9}\right] \cup \left[\frac{8}{9}, 1\right]$. By repeating this process, one obtains at the n^{th} iteration the set I_n wich is the union of 2^n intervals, each having a length 3^{-n} and is included in $I_0, I_1, \ldots, I_{n-1}$, as shown in Fig. 6.1. The Cantor set is then defined as the limit of the removal process by

$$C = \bigcap_{n=0}^{\infty} I_n \tag{6.1}$$

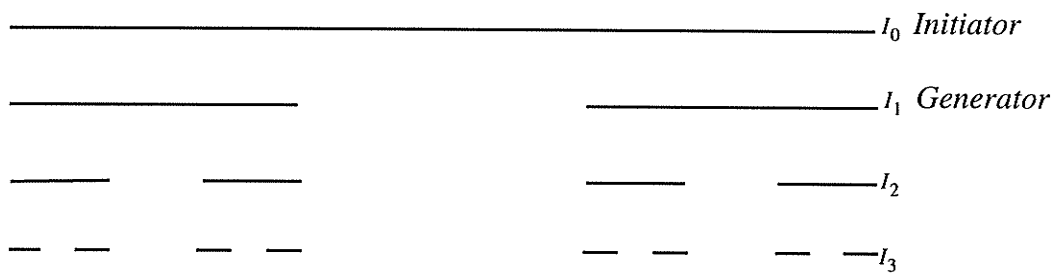

Fig. 6.1 Cantor Set generation.

The irregularity of the Cantor set comes from the fact that it is nowhere dense, and has Lebesgue measure zero.

Minkowski Curve

The Minkowski curve is produced according to the following rule: beginning with a unit straight line as initiator (although it may be anything else), then the Step 1 consists of generating a curve containing eight scaled down initiators (the generator) with a scaling of 1/4 each, as shown in Fig. 6.2. At Step 3, the process is repeated for the eight segments and so on. Once the curve is constructed at step $k-1$, then we scale it by 1/4 and use it to replace every initiator in the generator to obtain the object at step k. The Minkowski curve is the limit curve, when $k \to \infty$. This limiting curve, although produced by simple rules has complicated mathematical characteristics: i) it is nowhere differentiable, and ii) the length of the curve is infinite. At Step k, the length is $L_k = 2^k$, and at the limit the length is $L = \lim_{k \to \infty} 2^k = \infty$. Such irregular characteristics make the Minkowski curve a pure

mathematical fractal object. The self-similarity is obvious in this case since, zooming on the curve, one always gets the same structure (scaled, shifted and rotated) as the entire curve.

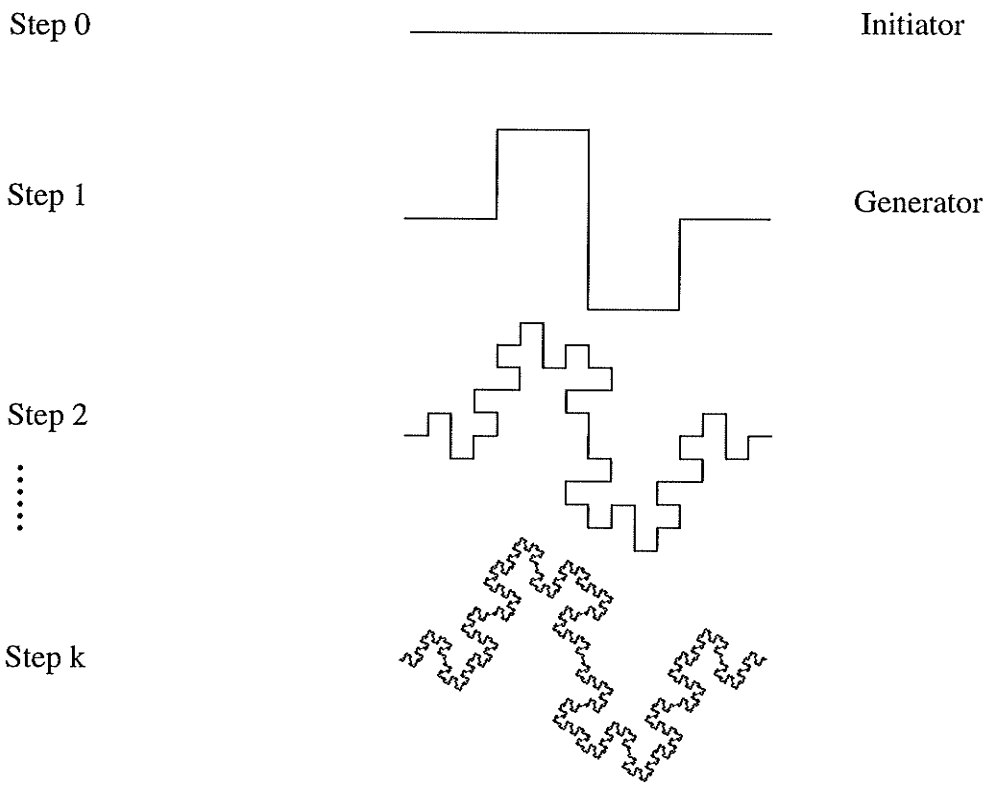

Fig. 6.2 Generation of the Minkowski curve (after [Huan03]).

Von Koch Curve

With the same initiator as in the Minkowski curve production, but using the generator as illustrated in Step 1 of Fig. 6.3, one obtains, at the limit, another example of a pure fractal called the *Von Koch curve*. Here, the initiator is scaled down by a factor $r = 1/3$ and replaced by 4 copies of its scaled version. At the k^{th} iteration, the curve is the union of

4^k segments, each having a 3^{-k} length. Therefore, the length of the Von Koch curve is infinite. Notice also that the Von koch curve is continuous everywhere, but nowhere differentiable. The generator has only 3 points where the curve is not differentiable, and this number, which is 15 at Step 2, increases to the infinity at the limit.

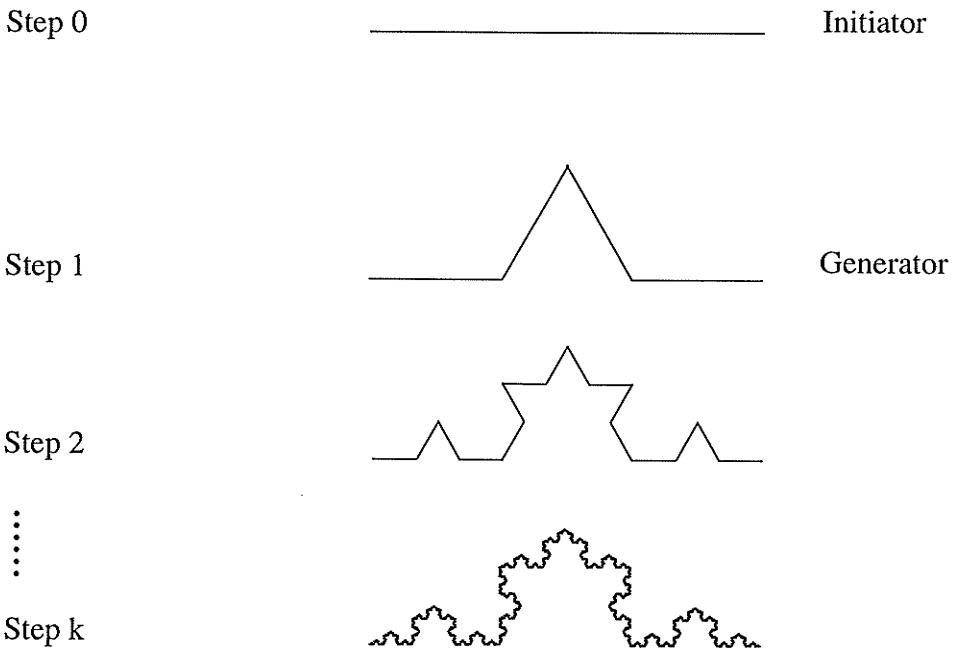

Fig. 6.3 Generation of the Von Koch curve (after [Huan03]).

Both the Minkowski and the Von Koch curves are not single-valued functions, but rather parametrized curves. Examples of nowhere differentiable single valued continuous functions were introduced by Weierstrass in 1875.

Weierstrass Functions

The Weierstrass functions are given by

$$f(x) = \sum_{k=0}^{\infty} \lambda^{-sk} \cos(\lambda^k x), \quad 0 < s < 1 \text{ and } \lambda > 1 \tag{6.2}$$

These functions are continuous, but nowhere differentiable. Mathematicians believed, at that time, that all continuous functions must be differentiable in at least one point. Figure 6.4 presents two examples from this collection.

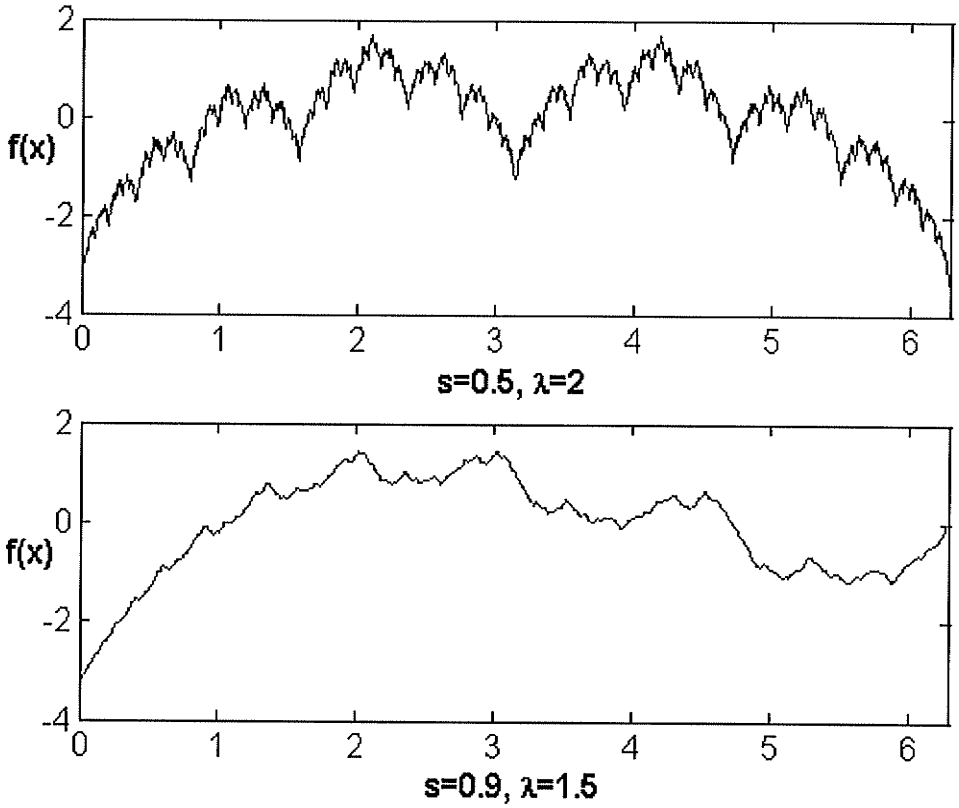

Fig. 6.4 Some examples from Weierstrass functions collection.

It is clear that the fractal objects presented in this section are constructed objects (man-made) exhibiting the self-similarity. In real life, however, objects are more complex. One can extend this notion of self-similarity to the notion of *self-affinity*, i.e., using different scales along different directions [Kins95]. For example, a curve $g(x)$ may satisfy

$$g(\lambda x) = \lambda^{\alpha} g(x) \tag{6.3}$$

for a scaling factor λ and a scaling exponent α.

One can extend the deterministic fractality to statistical self-similarity and self-affinity, leading to *random scaling functions* whose probability density functions satisfy Eq. 6.3 [TuBA98]. The fractional Brownian motion is an example of such statistical fractals. However, most objects in nature are neither strictly deterministic nor statistically self-similar/affine, but instead they have a finite range of self-similarity/affinity [Kins95]. This extension to multiple fractals will be discussed in Sec. 6.2. In the following, a characterization of objects that are strict fractals but not a combination of fractals is first presented.

6.1.2 Fractal Dimensions

The irregularity of a strict fractal object can be characterized by a scalar called *fractal dimension.* The fractal dimension generalizes the *topological* dimension in the sense that for regular objects, both dimensions are the same (The topological dimension of a set is an integer D_T such that each point of the set has arbitrarily small neighborhoods with boundary of dimension $D_T - 1$ [Falc90]). There are many fractal dimensions. Kinsner has presented more than 21 fractal dimensions in a unified framework [Kins94a], where the dimensions are classified into morphological, entropy, variance, and spectral dimensions. In this section, the *Hausdorff dimension*, the *similarity dimension* and the *box-counting dimension* are discussed.

Hausdorff Measure and Dimension

The diameter of a set A of $\Re^d$ is the maximum distance between any pair of

points of A, i.e., $|A| = sup\{|x-y| : x, y \in A\}$. For a given $r>0$, a $r-cover$ of A is any countable collection of subsets $\{U_i\}$ such that $0<|U_i| \le r$ and $A \subset \bigcup_{i=1}^{\infty} U_i$.

The s-dimensional *Hausdorff measure* of A, introduced in 1919 by Hausdorff is defined by [TuBA98]

$$\mu^s(A) = \lim_{r \to 0} inf\left\{ \sum_{i=1}^{\infty} |U_i|^s : \{U_i\} \text{ is a } r-cover \text{ of } A \right\} \tag{6.4}$$

The Hausdorff measure is an extension of the Lebesgue measure. In fact for an integer s, Eq. 6.4 gives the d-dimensional volume multiplied by a constant. More precisely, for Borel sets of $\Re^d$, one has [Falc90]

$$\mu^n(A) = c_n \mu_L(A) \tag{6.5}$$

Where $c_n = \pi^{\frac{n}{2}} / 2^n \left(\frac{n}{2}\right)!$ is the volume of the unit n-dimensional ball and μ_L is the Lebesgue measure.

The Hausdorff (or Hausdorff-Besicovitch) dimension of A is the critical value of s where $\mu^s(A)$ jumps from ∞ to 0, i.e.,

$$D_H = sup\{s : \mu^s(A) = \infty\} = inf\{s : \mu^s(A) = 0\} \tag{6.6}$$

The Hausdorff dimension presents the advantages of being defined for any set (i.e., not only self-similar/affine sets, but also statistical self-similar/affine sets) and of providing a basic and mathematical characterization of the geometrical complexity of fractal objects. It is more adapted, however, to ideal continuous functions and its evaluation is

very difficult for engineers who are dealing with discrete, digital signals and images. A simplification of the Hausdorff dimension that would be easier to compute numerically is then necessary. For self-similar objects, this simplification leads to the *similarity* dimension, and by considering only covering sets with equal diameters, the Hausdorff dimension becomes the so called *box-counting* dimension.

Similarity Dimension

For strictly self-similar fractal sets, the computation of D_H becomes straightforward. In fact, it is known that a self-similar set is made up with $N(r)$ distinct (non-overlapping) copies of itself, each of which has been scaled down by a ratio r in all coordinates. The *similarity dimension* D_S is then given by

$$D_S = \frac{\log N(r)}{\log(1/r)} = -\frac{\log(\text{ number of self-similar copies})}{\log(\text{ magnification factor})} \tag{6.7}$$

The similarity dimension is valid only for strictly self-similar fractal sets. The following subsection presents another simplification of the Hausdorff dimension which is valid for a larger class of fractal objects.

The Box-Counting Dimension

One could require that the diameters of all the covering sets U_i be equal to r (instead of $|U_i| \le r$). The minimum number of the covering set, $N_r(A)$, intersected by the object A is then counted. By replacing $|U_i|$ by r in Eq. 6.4, it follows

$$inf\left\{\sum_i r^s : \{U_i\} \text{ is a } r\text{–}cover \text{ of } A\right\} = N_r(A) r^s \tag{6.8}$$

If the set A has a topological dimension D, then it is obvious that $N_r(A) \sim r^{-D}$. More generally, the box-counting dimension D_{BC} follows the same power-law relation for small r

$$N_r(A) \sim r^{-D_{BC}} \tag{6.9}$$

The box-counting dimension is then defined by repeated measurements of $N_r(A)$ on reduced covering sets diameter according to the following formula

$$D_{BC}(A) = \lim_{r \to 0} \frac{\log N_r(A)}{\log(1/r)} \tag{6.10}$$

When $N_r(A)$ is the number of the "r-mesh" volume elements (vels [Kins94]) of side r that cover A, the box-counting dimension is also called the Hausdorff mesh dimension. Note also that some authors refer to the box-counting dimension as the Minkowski, Minkowski-Boulignard dimension, or the Kolmogorov capacity dimension. The *capacity* dimension generalizes this result and is defined by

$$D_C(A) = \lim_{r \to 0} inf \frac{\log N_r(A)}{\log(1/r)} \tag{6.11}$$

The box-counting dimension can be used to evaluate the self-affine objects while the similarity dimension cannot. Two drawbacks, however, of the box-counting dimension have to be underlined: (i) D_{BC} is only an approximation of D_H even for strict self-similar sets, and (ii) unlike D_H which is associated to a measure, D_{BC} is not, and consequently D_{BC} can be non-zero while D_H is equal to zero.

Table 6.1 shows the dimension values of the pure fractal objects described in Sec.

6.1.1. The similarity dimensions are easily computed for Cantor set, Von Koch and Minkowski curves as they are self-similar, and are given by

$$D_S(\text{Minkowski}) = \lim_{k\to\infty} \frac{\log 8^k}{\log 4^k} = 1.5 \tag{6.12}$$

$$D_S(\text{Koch}) = \lim_{k\to\infty} \frac{\log 4^k}{\log 3^k} \approx 1.262 \tag{6.13}$$

$$D_S(\text{Cantor}) = \lim_{k\to\infty} \frac{\log 2^k}{\log 3^k} \approx 0.631 \tag{6.14}$$

The computation of the fractal dimension of the graph of Weierstrass functions uses more algebra related to the singularity measurements to be studied in the next section. It can be shown that for Weierstrass, with λ and s parameters, D_H and D_{BC} are [Falc90]

$$D_H = D_{BC} = 2 - s, \text{ for } 0 < s < 1 \tag{6.15}$$

Table 6.1: Fractal dimensions for the Von Koch curve, the Minkowski curve, the Cantor set, and the Weierstrass function.

Dimension	Koch Curve	Minkowski Curve	Cantor set	Weierstrass function ($\lambda = 2$, $s = 0.5$)
Hausdorff D_H	1.262	1.500	0.631	1.5
Similarity D_S	1.262	1.500	0.631	n/a
Box-Counting D_{BC}	1.2663	1.5446	0.631	1.5

As stated before, usually the objects in nature are not single fractal objects but multiple fractal objects. The question then is: does the fractal dimension characterize these

types of mixture of fractal objects? The answer is, unfortunately, negative [Kins94]. A simple example follows from the result that the sum of two fractal objects, with fractal dimensions D_1 and D_2, has the Hausdorff fractal dimension $D_H = max\{D_1, D_2\}$. Therefore, fractal dimensions only describe the most complicated features of multiple fractal objects, and any attempt to discriminate multiple fractals by only the mean of their fractal dimension will be inefficient. For a complete description of such objects, the *multi-fractal analysis* (MA) presented in the following section has proven to be a very powerful tool.

6.2 Multifractal Analysis

As stated before, the objects in nature are not single fractal sets but rather a collection of multiple fractal objects. This collection can be made with infinitely many fractals so that the fractal dimension will be useless to characterize such geometry. However, multifractal analysis can give some answers to the characterization of such multiple fractals geometry. While a fractal refers to a set (or an object), a multifractal can be a function, a measure or more generally a stochastic process (or random function). This thesis considers the multifractal measures formalism. For the extension to the multifractal analysis of stochastic processes or random measures see [MaFC97]. Multifractal measures were introduced by Mandelbrot in 1972, popularized by Frish and Parisi in 1985 who used the term "multifractals" [PaFr85], and a strong mathematical basis for this field has been developed within the last few years. MA has been applied to physical processes like turbulence, earthquakes, signal and image processing and recently to economics [MaFC97]. As with fractals, there is no precise definition of multifractal measures. Some authors extend the notion of self-similarity of sets of points, which is fundamental in

geometric (mono)fractals, to self-similarity of measures. For this dissertation, multifractals are defined as measures whose geometric support is the union of one or more fractal sets. This decomposition is the basis of the segmentation scheme which will be presented in the next chapter.

The degree of regularity (or singularity) of multifractals varies, in general, from point to point and it is crucial to characterize it. The following section presents a characterization of singularity by the Hölder exponent.

6.2.1 Regularity Measurements: The Hölder Exponent

Definition 6.1: A signal $S(x)$ has a *Hölder exponent* (or a *Lipschitz regularity*) $h(x_0)$ at the point x_0 if $h(x_0)$ is the sup of the α such that there exist $K > 0$, and a polynomial P of degree $m = \lfloor \alpha \rfloor$ (the integer part of α) such that

$$|S(x) - P(x - x_0)| \leq K|x - x_0|^{\alpha} \tag{6.16}$$

The exponent $h(x_0)$ characterizes the regularity of the signal S at x_0. The smaller the values of h are, the higher is the degree of singularity of S. If $S(x)$ is m times continuously differentiable (in this case, the polynomial P is given by the Taylor development of S in the neighborhood of x_0) but has non derivative at order $m+1$ in x_0, then $h(x_0) = m+1$, meaning that the degree of the regularity is $m+1$ (note that the m^{th} derivative is continuous). Conversely, if $h(x_0) > m$, then S is necessarily m times continuously differentiable. In fact, the Hölder exponent extends the notion of differentiability to the non-integer order. For $0 \leq h(x_0) \leq 1$, the polynomial becomes $P(x - x_0) = S(x_0)$. Figure 6.5 shows different kinds of singularities described by different Hölder exponents.

Continuity and non-differentiability corresponds to $h = 1$, boundedness but discontinuous to $h = 0$, a degree of singularity $h = -1$ corresponds to a dirac (the dirac is not a function in the strict sense, but a generalized function or tempered distribution having a derivative at all order in the sense of distribution [Shwa97]).

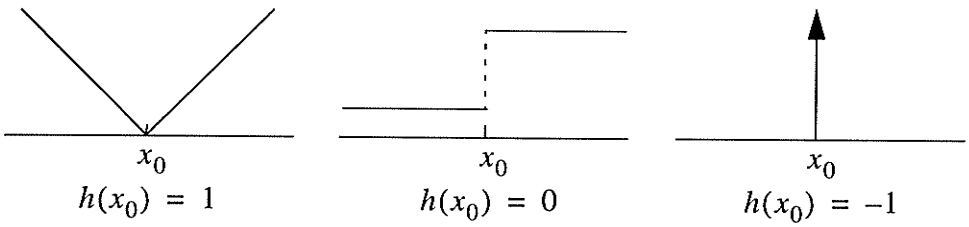

Fig. 6.5 Different types of singularities.

The importance of detecting singularities comes from the fact that it carries most of the information in signals. Mallat and Zhong constructed an approximation of a given signal from its multiscale edges [MaZh92]. Recently, Turiel and Del Pozo reconstructed images from their singular fractal manifold defined as the set of pixels having the minimum possible Hölder exponent [TuDe02]. This importance had lead many researchers to develop techniques to detect and measure the degree of singularity in a signal. Among the used tools, the Fourier transform although it gives a sufficient condition on the irregularity of signals, remains very global and cannot provide any local singularity information. The wavelet transform, however, proved to be an efficient tool to measure the local singularities as can be seen in the next section.

6.2.2 Singularity Detection with Wavelets

This section uses the same notations as in Ch. 4. Therefore for any signal $S \in L^2(\Re)$, and any mother wavelet ψ satisfying Eq. 4.6, the wavelet transform of S is given by Eq. 4.5; i.e.,

$$\tilde{S}_\psi(a,b) = \frac{1}{\sqrt{a}} \int_{-\infty}^{\infty} \psi\left(\frac{x-b}{a}\right) S(x)dx \tag{6.17}$$

A function $\phi \in L^2(\Re)$ is called a smoothing function if ϕ has a fast decay and $\int_{-\infty}^{\infty} \phi(x)dx \neq 0$. This work considers the family of wavelets constructed from smoothing functions by $\psi(x) = (-1)^n \phi^{(n)}(x)$. Such wavelets have exactly n vanishing moments and generalize the concept of Hölder exponent given by Eq. 6.16, as stated in the following theorem [Mall98].

Theorem 6.1: *Let $n > 0$ be an integer, then S has a non-integer Hölder exponent $h < n$ uniformly over an interval (b_1, b_2) if and only if there exists $K > 0$ such that*

$$\forall\ (a,b) \in \Re^+ \times (b_1, b_2)\ , \quad \left|\tilde{S}_\psi(a,b)\right| \leq K a^{h+\frac{1}{2}} \tag{6.18}$$

Equation 6.18 shows that it is possible to measure the Hölder exponents from the scaling behaviour of the wavelet transform modulus. For a local measurement of the Hölder exponent h_0 at a point b_0, Jaffard [Jaff91] extended the result in Eq. 6.18 to

$$\forall\ (a,b) \in \Re^+ \times \Re\ , \quad \left|\tilde{S}_\psi(a,b)\right| \leq K a^{h_0+\frac{1}{2}} \left(1 + \left|\frac{b-b_0}{a}\right|^{h_0}\right) \tag{6.19}$$

The decay at fine scales can also be measured from the wavelet modulus-maxima defined in the following [MaHw92].

Definition 6.2: *A point* (a, b_0) *is called a modulus maxima if* b_0 *is a local maximum of the map* $b \rightarrow |\tilde{S}_\psi(a, b)|$.

The following theorem, proved by Mallat and Hwang [MaHw92], shows how the modulus maxima are related to the singularities of S.

Theorem 6.2: *Under the same conditions as before, it follows*

$\{x$: S has at x a Hölder exponent $h < 1\} \subseteq$

$\{x$: $\forall \varepsilon > 0, \exists$ a modulus maxima point (a, b) with $|(a, b)-(0, x)| < \varepsilon\}$

This means that if the wavelet transform has no modulus maxima at fine scales, then S is locally regular, or equivalently, singularities are located at points to which a sequence of wavelet maxima converges. Therefore, by following the modulus maxima points (which form a continuous line) to the smallest scale, one may find singularities. Morever, Mallat and Zhong presented an algorithm for reconstruction of signals from their wavelet transform modulus maxima [MaZh92].

6.2.3 Multifractal Formalism

To present a multifractal formalism, consider a measure space $(X, B(X), \mu)$ where X is a subset of $\Re^d$, and $B(X)$ are the Borel subsets of X. A sufficient condition for the measure μ to be multifractal is

$$\mu(B_s(x)) = C(x)s^{d+h(x)} + o(s^{d+h(x)}) \text{ for small } s \tag{6.20}$$

where $B_s(x)$ is a closed sphere centered at x with radius s, $C(x)$ is a constant depending only on x, and $h(x)$ is the Hölder exponent at the point x. In fact, Eq. 6.20 allows parti-

tioning the measure support into multiple number of fractal sets, with different sets corresponding to different h. Each fractal component is formed by points having the same Hölder exponent; i.e.,

$$F(y) = \{x \in X: h(x) = y\} \tag{6.21}$$

First, notice that the measure μ may be extremely irregular with singularities of possibly many orders making its support of zero Lebesgue measure, and hence it does not have any associated density function (i.e., Radon-Nikodym derivative). Instead, the description of such measures is then provided by the family of the fractal dimensions $f(y) = dimF(y),\ y \in \Re$, called the *multifractal singularity spectrum*. Therefore, characterizing the measure μ results in computing its multifractal spectrum.

Equation 6.20 gives $h(x) = \lim_{s \to 0} \dfrac{\log \mu(B_s(x))}{\log s}$, and it follows that

$$F(y) = \left\{ x : \lim_{s \to 0} \frac{\log \mu(B_s(x))}{\log s} = y \right\} \tag{6.22}$$

The set $F(y)$ is the limit of the decreasing family of sets obtained for every $\varepsilon > 0$ by

$$F_s(y, \varepsilon) = \left\{ x \in X: \left| \frac{\log \mu(B_s(x))}{\log s} - y \right| < \varepsilon \right\} \tag{6.23}$$

The multifractal spectrum is then expressed as [Hart91]

$$f(y) = \lim_{\varepsilon \to 0} \lim_{s \to 0} \frac{-\log \int_{F_s(y, \varepsilon)} (1/\mu(B_s(x)))\mu(dx)}{\log s} \tag{6.24}$$

An example of multifractal measure is given by the collection $\mu_p, 0 < p < 1$ of Cantor measures defined on the Cantor set C. Each member μ_p of the family is obtained as a limit by allocating a probability p to the left subinterval and $1-p$ to the right subinterval, as shown in Fig. 6.6.

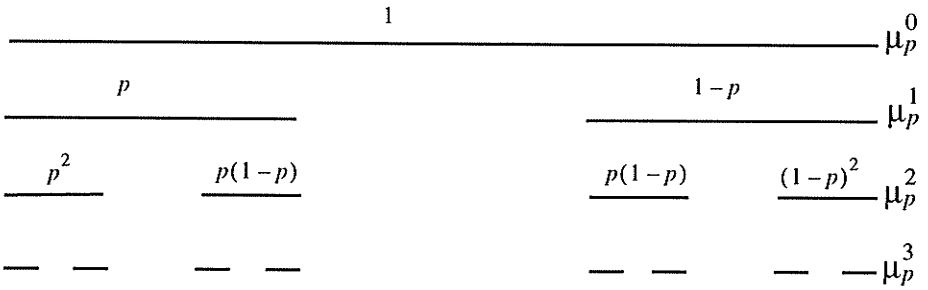

Fig. 6.6 The Cantor measure μ_p .

A probabilty measure μ_p^n is then defined on each subset I_n. Let $K_n(y)$ be the set of sub-intervals J of width 3^{-n} such that $(\log\mu_p^n(J))/(\log 3^{-n}) = y$. Then the multifractal spectrum of μ_p can be expressed as

$$f_p(y) = \lim_{n\to\infty} \frac{\log\ card(K_n(y))}{\log 3^{-n}} \tag{6.25}$$

Figure 6.7 shows the graphs of $f_{1/2}(y)$ and $f_{1/3}(y)$. Notice that $f_{1/2}$ exists at only one point $y = \log 2/\log 3$, and $f_{1/2}(\log 2/\log 3) = \log 2/\log 3$ which is the fractal dimension of the Cantor set. This reflects the fact that $\mu_{1/2}$ is a monofractal. This function is represented by the dotted line. The spectrum of $\mu_{1/3}$ is supported by a continuous range of values of y $\left(y_{min} = \left(-\log\frac{2}{3}\right)/(\log 3) = 1-(\log 2)/(\log 3),\right.$ and $\left. y_{max} = \left(-\log\frac{1}{3}\right)/(\log 3) = 1\right)$, indicating the multifractal nature of $\mu_{1/3}$.

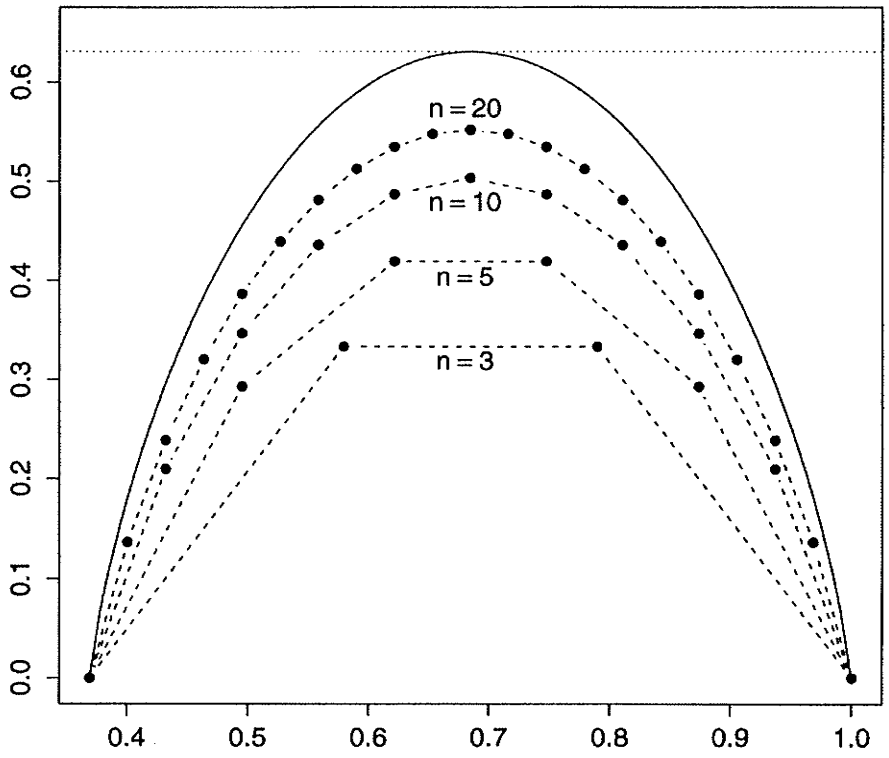

Fig. 6.7 Multifractal spectrum of the Cantor measures $\mu_{1/2}$ and $\mu_{1/3}$ (After [Hart91]).

As the singularities in multifractals are not isolated, the numerical computation of Hölder exponents at each point can be very complicated, and so is for $f(y)$. In many cases, it is preferable to estimate first the *scaling exponent* defined by

$$\theta(q) = \lim_{s \to 0} \frac{\log \int_{(\mu(B_s(x)) > 0)} \mu^{q-1}(B_s(x)) \mu(dx)}{\log s} \tag{6.26}$$

and then find the multifractal spectrum from the Legendre transform given by

$$f(y) = \min_q \{qy - \theta(q)\} \tag{6.27}$$

The exponent $\theta(q)$ is very close to the so called *Rényi dimension spectrum* defined in the

following subsection.

The Rényi Dimension Spectrum

The Rényi entropy H_q is a generalization of the Shannon entropy and is given for any probability distribution $P = (p_j)$ by [CoTh91]

$$H_q(P) = \frac{1}{1-q}\log\sum_i p_j^q \qquad -\infty < q < \infty \tag{6.28}$$

A generalization of the Rényi entropy to any measure μ leads to the Rényi dimension spectrum denoted D_q and is given by

$$\begin{cases} D_1 = \lim\limits_{s\to 0} \dfrac{\int\limits_{(\mu(B_s(x))>0)} (\log\mu(B_s(x)))\mu(dx)}{\log s} \\ D_q = \dfrac{\theta(q)}{q-1} \qquad \text{for } q \neq 1 \end{cases} \tag{6.29}$$

The Rényi dimension spectrum is a bounded monotonically decreasing function of q, and is related to the multifractal spectrum by Eq. 6.27. When the measure μ has a *pdf*, D_q is constant for every $q > 0$. Also, for many particular values of q, D_q is reduced to some known fractal dimensions. More precisely, one can show that D_0 is simply the box-counting dimension, D_1 is called the *information dimension*, and D_2 is the *correlation dimension* [Kins94]. The bounds on D_q can also be found for $q = \pm\infty$ [Kins94].

There are many techniques to estimate the Rényi dimension spectrum. Based on the fact that $\theta(q)$ is the powerlaw exponent of a probabilty distribution, most of the techniques try to estimate D_q, for $q = 2, 3, 4, \ldots$. To have a clear view, let $X_1, X_2, \ldots, X_q$ be random variables (r.v), independent and identically distributed as μ. Then, the probability

distribution of the r.v $X = max\{\|X_i - X_q\|, i = 1, \ldots, q-1\}$ is given by

$$F_X(y) = \int \mu^{q-1}(B_s(x))\mu(dx) \tag{6.30}$$

and from Eq. 6.26, it follows that $\theta(q)$ is the decay at fine scale of $F_X(y)$; i.e.,

$$\theta(q) = \lim_{s \to 0} \frac{\log F_X(y)}{\log s} \tag{6.31}$$

Grassberger and Procaccia suggested a method to estimate this probability distribution based on pair-correlation ($q = 2$) [GrPr83]. Pawelzik and Schuster extended the pair-correlation function to any q^{th} order correlation [PaSc87], [Hart91].

A simpler technique, but requiring more memory, is the box counting algorithm which estimates the probability distribution by dividing the phase space into vels (volume elements) without overlapping [Kins94b]. In the next section, a Rényi spectrum estimation based on wavelets is presented.

6.2.4 Singularity Spectrum Using Wavelets

So far, the multifractal formalism for any measure μ was presented. In practice, engineers deal with images and there is a need then to specify a measure able to show the multifractal nature of such images when it is the case. Although many ways can be found to determine such measures [TuPa00], only some of them make Eq. 6.20 useful. The log-log linear regression on Eq. 6.20 can discriminate the Hölder exponents only if the measure is taking advantage from scaling. That is the case for the measure defined by the wavelet transform

$$\mu(B_s(x)) = \tilde{S}_\psi(s, x) \tag{6.32}$$

Equation 6.32 presents two advantages: (i) the first is computational, as there exist powerful algorithms to perform a wavelet transform, and (ii) second, the scaling power law provided by Eq. 6.18. Morever, there exists an algorithm to estimate the scaling exponent from the wavelet transform modulus maxima, as described in the following [Mall98]

Table 6.2: Mallat Algorithm for the Scaling exponent estimation.

Steps	Description
1	• Compute the wavelet transform of the signal.
2	• Find the modulus maxima $\{u_n(s)\}$ at each scale s.
3	• Compute the sum at power q, $Z_s(q) = \sum \left\lvert \tilde{S}_\psi(s, u_n(s)) \right\rvert^q$.
4	• The scaling exponent $\theta(q)$ is then obtained by linear regression of $\log Z_s(q)$ vs $\log s$.

The multifractal spectrum is obtained from $\theta(q)$ by taking the Legendre transform. In the next chapter, however, another approach to estimate the multifractal spectrum will be used. The iterated function systems (IFSs) introduced in the next section plays an important role in the estimation of the multifractal spectrum.

6.3 Iterated Function Systems (IFS)

Iterated function system (IFS) is the name given by Barnsley and Demko to define a set of contractive transformations, $\{w_i, i = 1, \ldots, N\}$ on $\Re^d$ [BaDe85]. For $d = 2$, the affine transformations allow all possible two dimensional transformations. Therefore, the study is restricted to the affine transformations (the IFS is then called *affine IFS*) given by

$$w_i\begin{pmatrix} t \\ x \end{pmatrix} = \begin{bmatrix} a_i & b_i \\ c_i & d_i \end{bmatrix} \begin{bmatrix} t \\ x \end{bmatrix} + \begin{bmatrix} e_i \\ f_i \end{bmatrix} \tag{6.33}$$

It is seen that, for a system using the self-similarity/affinity, the whole image can be described by only a few parameters $\{a_i, b_i, c_i, d_i, e_i, f_i, i = 1, \ldots, N\}$. This can lead to a compression rate of thousands to one. Figure 6.8 shows the so-called Barnsley's fern. It is constructed from an arbitrary point on the plan by iteratively applying the given IFS code.

a_i	b_i	c_i	d_i	e_i	f_i
0.85	0.04	–0.04	0.85	0	1.6
0.2	–0.26	0.23	0.22	0	1.6
–0.15	0.28	0.26	0.24	0	0.44
0	0	0	0.16	0	0

Fig. 6.8 Barnsley's fern and its IFS code.

6.3.1 IFS Decoding

The transformation of a compact subset $B \subset \Re^d$ with all the maps is denoted by

$$W(B) = \bigcup_{i=1}^{N} w_i(B) \tag{6.34}$$

It can be shown that W is also a contractive transformation on the metric space of compact subsets equipped with the Hausdorff distance (The hausdorff metric between two compact subsets A and B is the maximum separation of the farthest elements of A or B from the opposite set). Furthermore, the fixed point theorem states that W has a unique fixed point A which can be reached from any initial compact subset $B \subset \Re^d$ [Barn93] by

$$A = W(A) = \lim_{k \to \infty} W^k(B) \tag{6.35}$$

This fixed point A of W is called the *attractor* of the IFS, and the IFS decoding process consists of generating A by applying iteratively the transformations w_i, as indicated by Eq. 6.35. For that purpose, two methods were investigated: the *deterministic algorithm* (DA) and *the random iteration algorithm* (RIA). Starting from a non-empty compact set A_0, the deterministic algorithm computes the sequence $A_k = W^k(A_0)$ up to the attractor. While the convergence can be rapid, the DA uses all the maps at each iteration and this results in a large amount of computation. To overcome the memory constraint, the random algorithm applies at each iteration only one of the transformations $\{w_i\}$, randomly chosen with a predefined set probabilities $\{p_i\}$, often calculated using the formula (by default)

$$p_i = \frac{|a_i d_i - b_i c_i|}{\sum_{j=1}^{N} |a_j d_j - b_j c_j|} \tag{6.36}$$

Figure 6.9 displays the fractal object (the Sierpinski triangle here) for different iteration numbers, by applying both the deterministic algorithm and the random iteration algorithm with the default probabilities. The DA takes only 20 iterations to converge. Each iteration, however, takes many seconds to be performed because many points may be computed again and again. On the other hand, the RIA performs ten thousands more iterations in only a few seconds.

6.3.2 IFS Encoding

The IFS encoding process, also called IFS *inverse problem* can be formulated as follows:

Given any compact set A, find an IFS whose attractor is A. Due to its application to fractal signal and image compression, the inverse problem is becoming very important. Although no constructive solution can be obtained in general, the Barnsley's *collage theorem* gives an approximation by an IFS whose attractor is close to A.

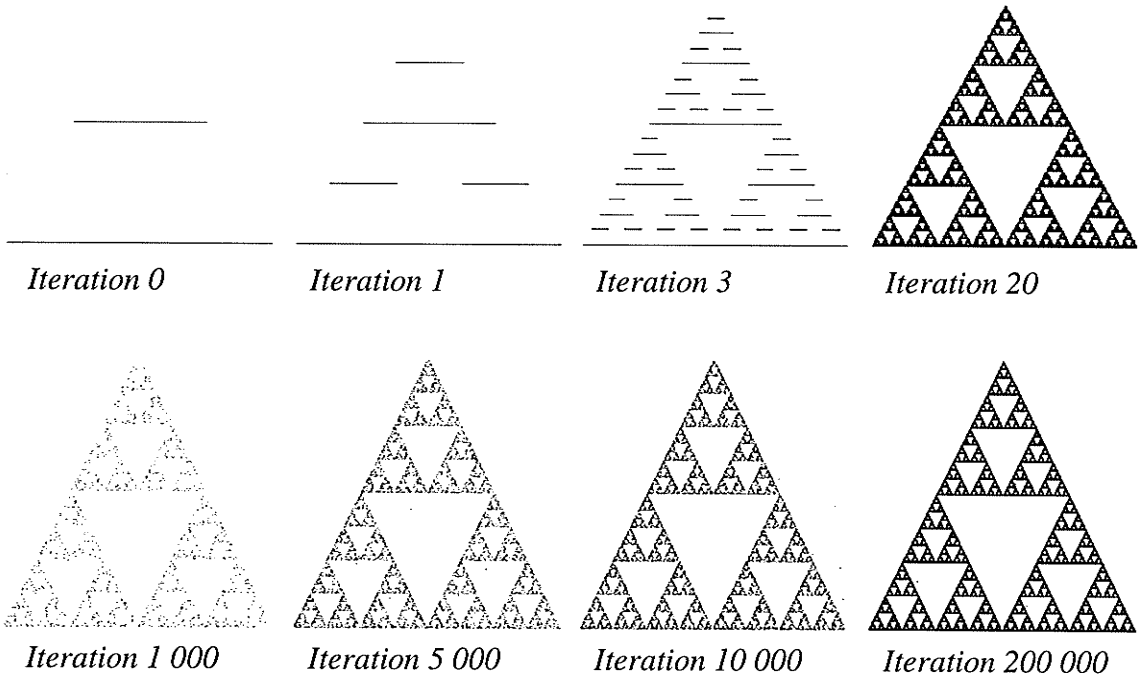

Fig. 6.9 Sierpinski triangle generated by IFS decoding. Top row: using Deterministic Algorithm, and down: using Iterated Random Algorithm.

The Collage Theorem [Barn93]: *Given an IFS code* $\{w_i, i = 1, \ldots, N\}$, *with contractive factor* $0 \le s < 1$ *and attractor* A, *then for every compact subset*

$$d(B, A) \le \frac{d(B, W(B))}{1 - s} \tag{6.37}$$

where $d(B, A)$ *is the Hausdorff metric*, and the factor s is the maximum of the contractive factors s_i of each w_i.

This theorem does not solve directly the inverse problem, but states that for a given subset A search for an IFS such that $d(A, W(A))$ is very small because such IFS has an attractor very close to A. Using another approach, Berkner constructed a wavelet-based solution for a special class of self-similar functions [Berk97].

In the present case, the interest is in approximating curves which are image boundaries from a collection of control points $\{(t_i, x_i), i = 0, 1, \ldots, N\}$, where $t_0 < t_1 < \ldots < t_N$. These curves are often fractals (continuous but nowhere differentiable) and can be modeled by an IFS whose attractor is the graph of a function f interpolating the control points, i.e., $f(t_i) = x_i$ for each i. Such functions are called *fractal interpolation functions* (FIF). It is shown [Barn93] that this inverse problem has a solution given by

$$w_i\begin{pmatrix} t \\ x \end{pmatrix} = \begin{bmatrix} a_i & 0 \\ c_i & d_i \end{bmatrix} \begin{bmatrix} t \\ x \end{bmatrix} + \begin{bmatrix} e_i \\ f_i \end{bmatrix} \tag{6.38}$$

where the parameters a_i, c_i, d_i, e_i, and f_i are determined by the following conditions:

$$a_i = (t_i - t_{i-1})/(t_N - t_0) \tag{6.39}$$

$$e_i = (t_N t_{i-1} - t_0 t_i)/(t_N - t_0) \tag{6.40}$$

$$c_i = ((x_i - x_{i-1}) - d_i(x_N - x_0))/(t_N - t_0) \tag{6.41}$$

$$f_i = \frac{((t_N x_{i-1} - t_0 x_i) - d_i(t_N x_0 - t_0 x_N))}{(t_N - t_0)} \tag{6.42}$$

$$|d_i| < 1 \tag{6.43}$$

The free parameters d_i are called *vertical scaling factors* and are related to the fractal dimension D of the curve by

$$\sum_{i=1}^{N} a_i^{D-1} |d_i| = 1 \tag{6.44}$$

For more complicated (high curvature) boundaries, the generalized fractal interpolation functions which are attractors of hidden IFS are used. Here, the data points are 3-dimensional $\{(t_i, x_i, y_i), i = 0, 1, \ldots, N\}$ and the curve to be approximated has $\{(x_i, y_i), i = 0, 1, \ldots, N\}$ as control points. The IFS model is written by

$$w_i \begin{bmatrix} t \\ x \\ y \end{bmatrix} = \begin{bmatrix} a_i & 0 & 0 \\ c_i & d_i & 0 \\ c_{yi} & 0 & d_{yi} \end{bmatrix} \begin{bmatrix} t \\ x \\ y \end{bmatrix} + \begin{bmatrix} e_i \\ f_i \\ f_{yi} \end{bmatrix} \tag{6.45}$$

where a_i, c_i, d_i, e_i, and f_i are the same as in Eqs. 6.39 to 6.43, c_{yi} and f_{yi} are given by replacing x_i by y_i respectively in Eq. 6.41 and Eq. 6.42, while d_{yi} are free parameters such that $|d_{yi}| < 1$.

6.4 Summary

Following Kinsner's conjecture [Kins94], it was pointed out, in this chapter, that it is not sufficient to characterize a complicated object just using one or two complexity measures. Although there exist many fractal dimension definitions, no single dimension can be, by itself, a characteristic of discrimination between complex objects. Instead, the multifractal singularity spectrum as well as the Rényi dimension spectrum, which are related by the Legendre transform, can characterize the complexity of objects completely. Two methods for estimating the scaling exponents were discussed. One is based on probability distribution and the other one on the wavelet modulus maxima. It was also shown

that an IFS is a simple collection of contraction mappings capable of providing a high compression rate but also estimating the fractal dimension of a set. What is needed now is how to use the material presented here in order to segment SAR images. This is the objective of the next chapter.

CHAPTER VII

MULTIFRACTAL ANALYSIS BASED SEGMENTATION FOR SAR IMAGES

This chapter presents an algorithm based on multifractal analysis and iterated function systems (IFS) for SAR image segmentation. It begins by computing the wavelet transform modulus and modulus maxima. Then, the Rényi dimension spectrum for the SAR images is approximated. After estimating the multifractal singularity spectrum, an IFS-based approach in calculating the dimensions of the multifractal components is used. The chapter ends by a presentation of the segmentation results.

7.1 SAR Image Segmentation: An Overview

SAR provides a high-resolution imagery, which is usually used for terrain classification. For classification purposes, SAR images need to be segmented. This segmentation is not straightforward, due to the presence of the speckle noise on images. As stated in Ch. 2, the speckle is a natural phenomenon generated by the coherent processing of radar echoes. It is a non-Gaussian and multiplicative noise; i.e., regions of high signal intensity on images are subjected to more noise. The presence of the speckle reduces the ability to resolve fine details and also makes any statistical treatment for SAR image segmentation difficult. Several studies have addressed the issue of SAR image segmentation by adopting different techniques based either on grey levels or texture analysis. Segmentation based on grey levels involves the estimation of thresholds selected at the valleys of image histogram [EZWJ02]. Segmentation based on texture analysis,

which is the approach most widely investigated, uses techniques such as *Markov random fields* (MRF) [SmDe97], [DoFM03], various edge-based schemes [FLMC98], [Horr99], [GeRe01], [ToDL03], neural networks [Deca89], [KäWi91], [HaAY94], and fractals [DuYe02]. Some of these different methods are described below.

In [EZWJ02], segmentation is performed by estimating first the histogram parameters using a maximum likelihood technique, and then determining threshold(s). The method works for multi-modal images and allows one to select several thresholds to partition the images. Markov random fields approaches have been shown to provide an accurate segmentation of SAR images because of the ability to recognize objects by their statistics and textures. For example in [DoFM03], the SAR image is separated in small regions and the probability density function of each region is approximated by either Gamma- or Gaussian-MRF. Adjacent regions are then considered different if their means and/or standard deviations and/or spatial textures are different. Moreover in [SmDe97], MRF are used with an adaptive neighborhood. Information from other sources (such as maps and optical data) is integrated in order to choose an optimized neighborhood around the pixel of interest (minimum Markovian neighborhood). This last method may help to identify 1 and 2 pixel-wide structures.

Segmentation of SAR images using edge-detection techniques has also been widely investigated. Standard edge detectors (such as gradient-based or Bayesian detectors) perform poorly on SAR images because of the multiplicative speckle noise (more false edges are detected in areas of high reflectivity than in areas of low reflectivity). Therefore, several statistical edge detectors with constant false alarm rates have been

developed specifically for SAR images, like the ROA (*Ratio Of Averages*) [Bovi88], the LR (*Likelihood Ratio*) [OlBW96] and the ROEWA (*Ratio Of Exponentially Weighted Averages*) [FLMC98] operators. As an example, the ROEWA operator combined with watershed thresholding and LR region merging provides a rapid and efficient segmentation method, which permits the detection of all regions that can be distinguished by eye on the SAR images [FLMC98]. Another edge-detection method using the minimum mean square error (MMSE) principle in Bayesian off-line change-point detectors has been recently developed [ToDL03], and has given slightly better results than the ROEWA detector, at a higher computational cost.

Different studies have established that there is a correlation between decreasing fractal dimension of SAR data and microwave backscatter from special objects, which help in interpreting SAR images [TuBA98]. Fractal characterization, however, is very limited in detecting local regularities in images. In contrast, multifractal analysis has been applied in image analysis and classification, and proven to be important in texture analysis [DuYe02], [VGBF03]. In their approach, the authors begin by computing the Hölder exponents at each point, then they estimate the singularity spectrum, and finally they perfom multifractal exponents based feature extraction on the image.

In recent years, researchers have developed many techniques and approaches for edge detection, local regularity measurement and Hölder exponents estimation, as well as the Rényi dimension spectrum and the multifractal singularity spectrum computation. The power of the wavelet transforms comes from the fact that it offers a unified technique for performing all these matters. Stephane Mallat and his collaborators presented a framework

for the use of wavelets. In the following section, the wavelet modulus and mudulus maxima for SAR images are computed. Then, these results are used for Hölder exponents and Rényi dimension spectrum computation.

7.2 Wavelet Modulus and Modulus Maxima

Inspired by the Canny edge detection algorithm, Mallat defined the wavelet transform of an image $f(x, y)$ by using two wavelets obtained from a smoothing function $\theta(x, y)$ by

$$\tilde{f}_{\Psi}(x, y, s) = (\tilde{f}_{\psi^1}(x, y, s), \tilde{f}_{\psi^2}(x, y, s)) \tag{7.1}$$

where $\Psi = (\psi^1, \psi^2)$ and

$$\begin{cases} \psi^1(x, y) = \dfrac{\partial}{\partial x}\theta(x, y) \\ \psi^2(x, y) = \dfrac{\partial}{\partial y}\theta(x, y) \end{cases} \tag{7.2}$$

The horizontal and the vertical 2-D wavelet transform $\tilde{f}_{\psi^i}(x, y, s)$ for $i = 1, 2$ are given by

$$\tilde{f}_{\psi^i}(x, y, s) = \frac{1}{\sqrt{s}} \int_{-\infty}^{\infty} \psi^i\left(\frac{u-x}{s}, \frac{v-y}{s}\right) f(u, v)\,du\,dv \tag{7.3}$$

and the wavelet modulus at scale s is then defined as

$$\left|\tilde{f}_{\Psi}(x, y, s)\right| = \sqrt{\left|\tilde{f}_{\psi^1}(x, y, s)\right|^2 + \left|\tilde{f}_{\psi^2}(x, y, s)\right|^2} \tag{7.4}$$

As defined in Ch. 6, the wavelet modulus maxima are the points where the modulus is locally maximum.

For experiments, the partial derivative along x and y of the Gaussian kernel is used. The *dyadic* (i.e., the scales are $s = 2^j$) wavelet modulus, as well as the wavelet modulus maxima, are performed for three SAR images obtained after processing the three data sets E1-2208P, E2-5551P, and R1-24576R. The experiments were conducted on three subregions of these original images, each of them has a size 256 x 256 and they were chosen because of their representative features (mountains, lakes, farms).

Results on these images which are called now E1, E2, and R1, are shown on Figs. 7.1 to 7.3, respectively. Although these results are not the objective of this study but only a means for estimating the parameters of interest, some remarks are in order. There are more curves on the modulus maxima of the image E1 than the other two. This is because it contains more structures than the others. The curves correspond in this case to singularities in one direction and regularity in the other. The image R1 is less structured where the local maxima corresponding to the edges (the border of the lake) are present at almost all the scales. The figures show also the reconstructed images from their modulus maxima. Mathematically speaking, the wavelet modulus maxima do not characterize signals uniquely. Mallat and Liang Hwang presented an algorithm which provides a good approximation of the original image from its wavelet modulus maxima. Table 7.1 presents the SNR of images reconstruction.

Table 7.1: SNR of the reconstruction from the wavelet modulus maxima.

Image	SNR [dB]
E1	20.43
E2	16.51
R1	16.02

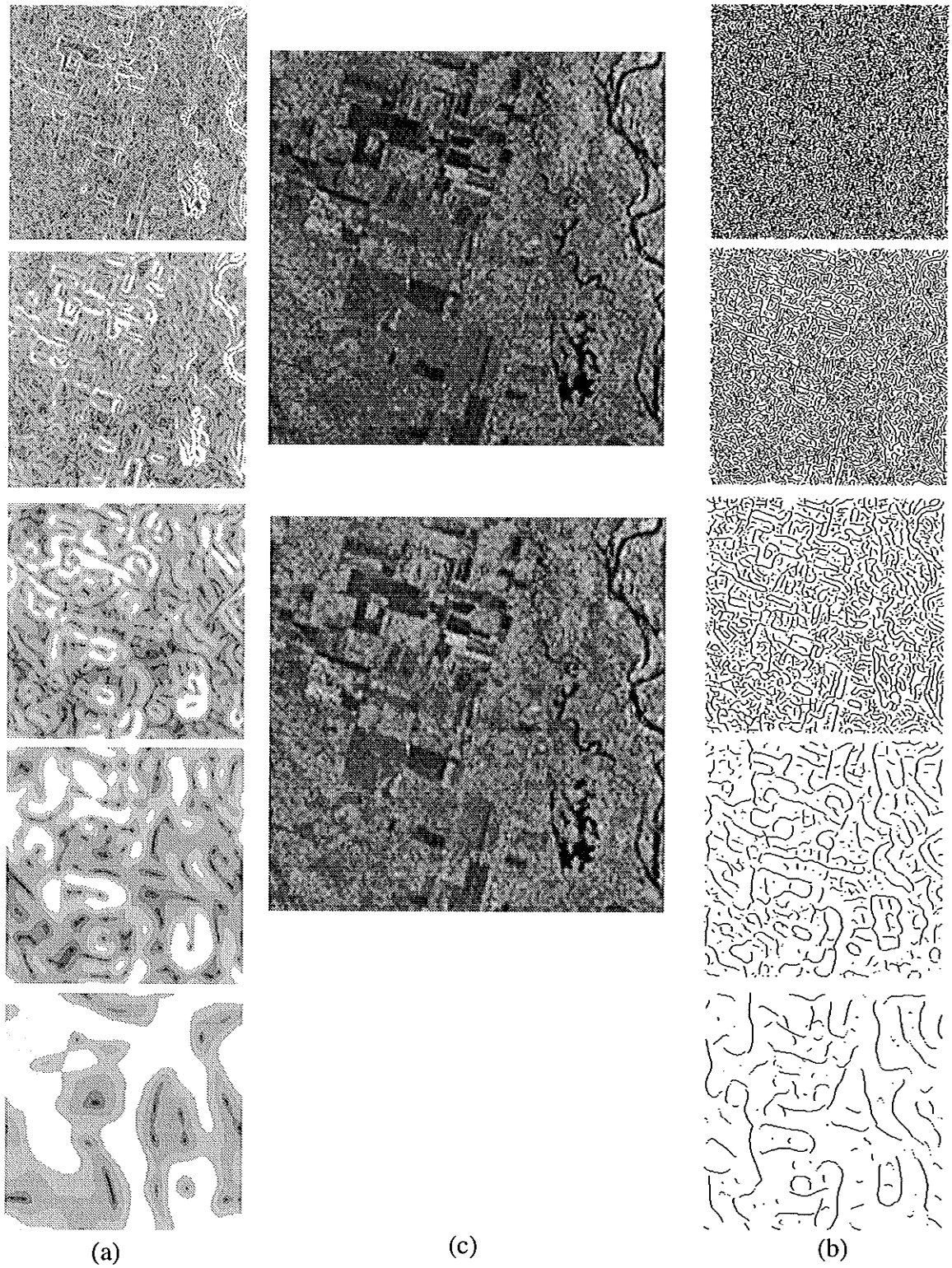

Fig. 7.1 Wavelet decomposition of E1 image at scales 2^j for $j = 1, 2, 3, 4, 5$. (a) Wavelet modulus, (b)Wavelet modulus-maxima, and (c) Original and reconstructed images.

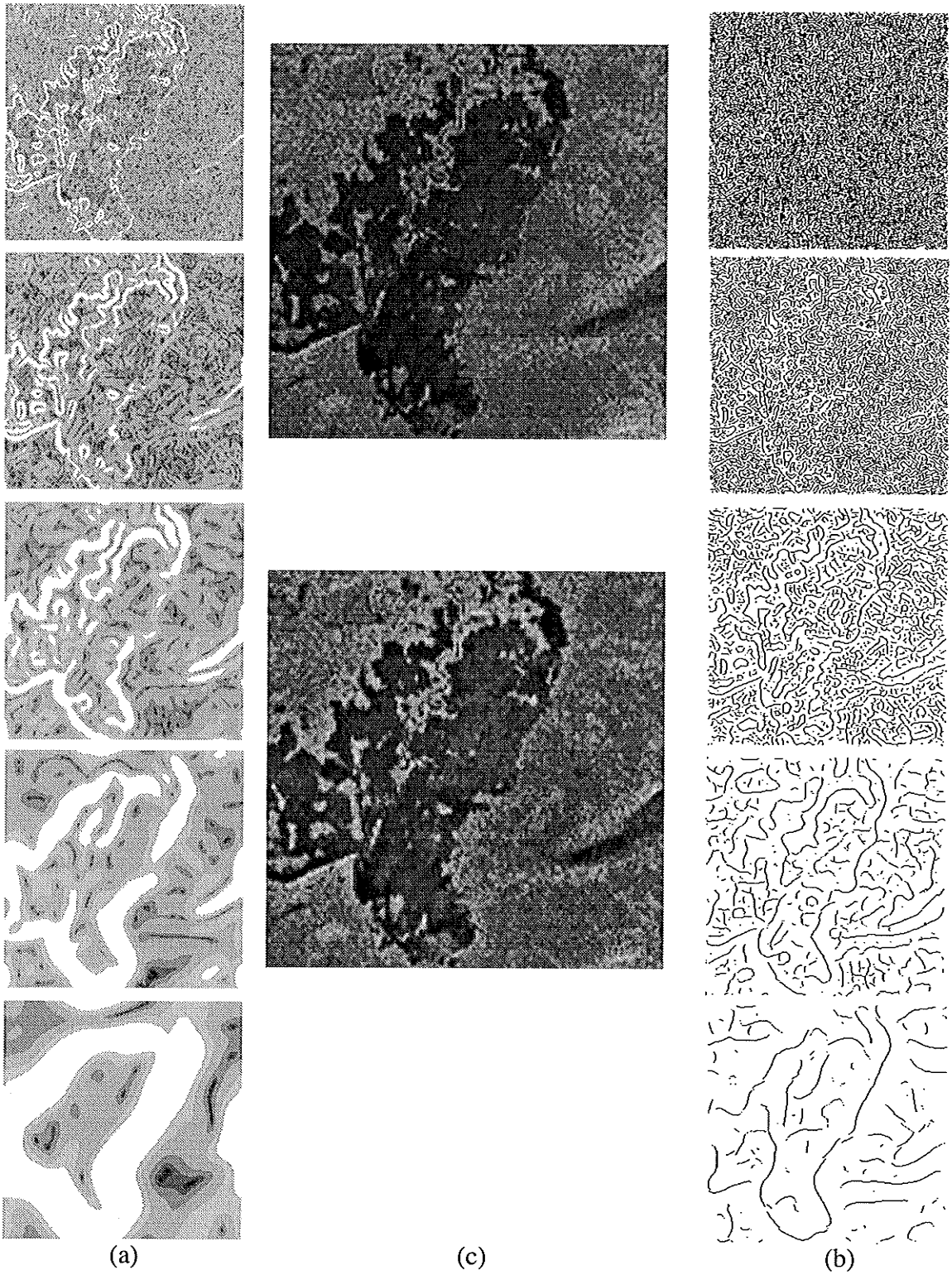

Fig. 7.2 Wavelet decomposition of E2 image at scales 2^j for $j = 1, 2, 3, 4, 5$. (a) Wavelet modulus, (b)Wavelet modulus-maxima, and (c) Original and reconstructed images.

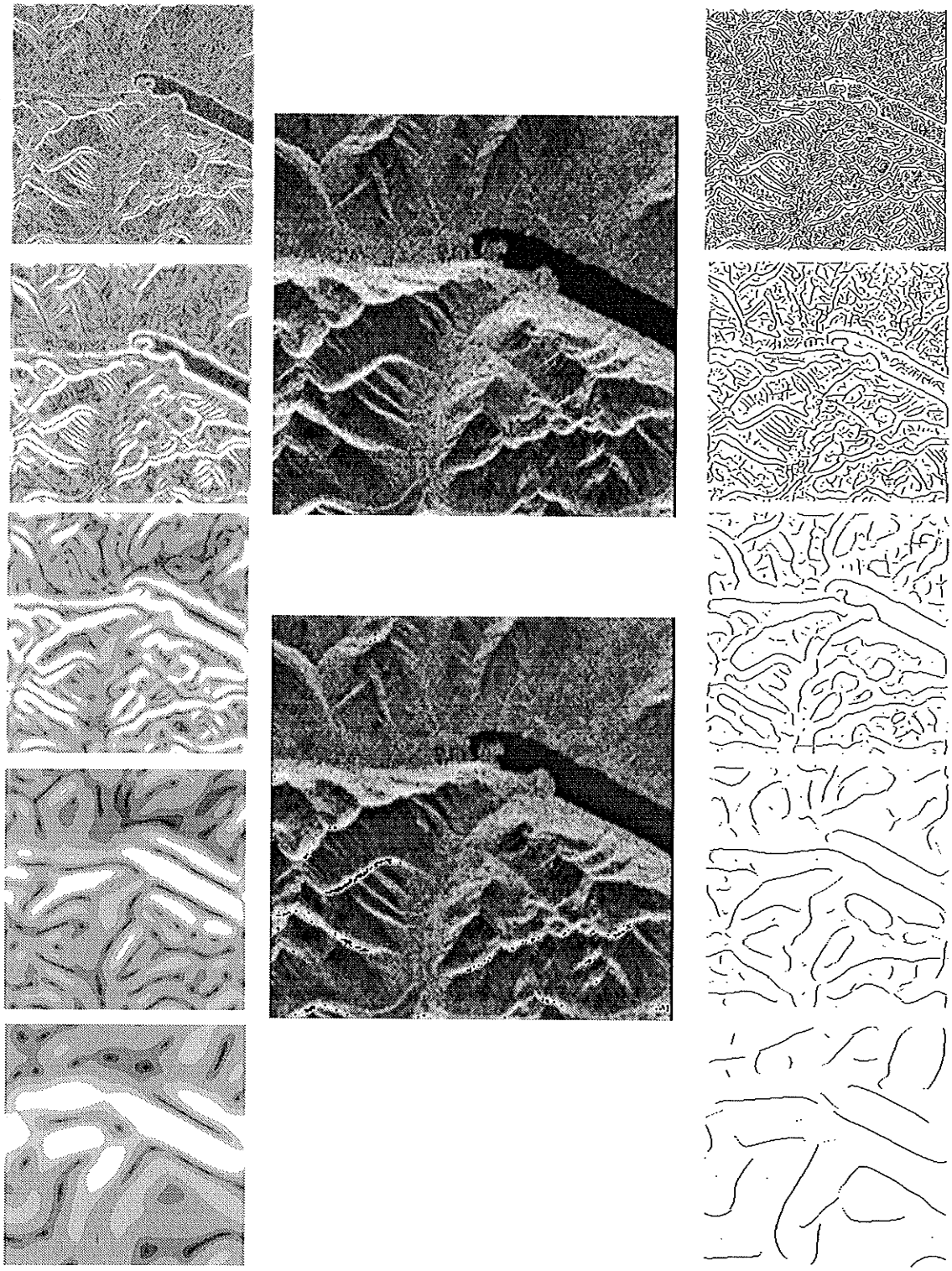

Fig. 7.3 Wavelet decomposition of R1 image at scales 2^j for $j = 1, 2, 3, 4, 5$. (a) Wavelet modulus, (b)Wavelet modulus-maxima, and (c) Original and reconstructed images.

The first application of the wavelet modulus and modulus maxima is the estimation of the Rényi dimension spetrum. This is the subject of the next section.

7.3 Multifractal Characteristics of SAR Images

The objective of this section is to confirm and to provide the multifractal characteristics of SAR images in order to use them on the next section for segmentation. To measure the complexity of the images, the following section begins by an estimation of the Rényi dimension spectrum.

7.3.1 The Rényi Dimension Spectrum

The global behaviour of the considered SAR images is shown in Fig. 7.4. In estimating the Rényi spectrum, the algorithm described in Ch. 6 was implemented. At each scale 2^j, we determined the position of all local maxima in a neighborhood of each pixel (we used a 15 x 15 window). The corresponding values of the modulus image at the same scale are used to compute $Z_j(q)$. Then the scaling exponent is obtained by linear regression of $\log Z_j(q)$ against j.

Figure 7.4 shows that the Rényi dimension spectrum is bounded by (1.9, 2.8) for all images. There are, however, small differences characterizing each image. The R1 image seems to be the most complex. This is because of the edges created by mountains tops. The E1 image contains more structures than E2 image, and this is reflected by the Renyi curve which is showning more complexity.

The Rényi curves of the three images are decreasing strictly monotonically and are bounded, thus confirming the multifractal characteristics of these images.

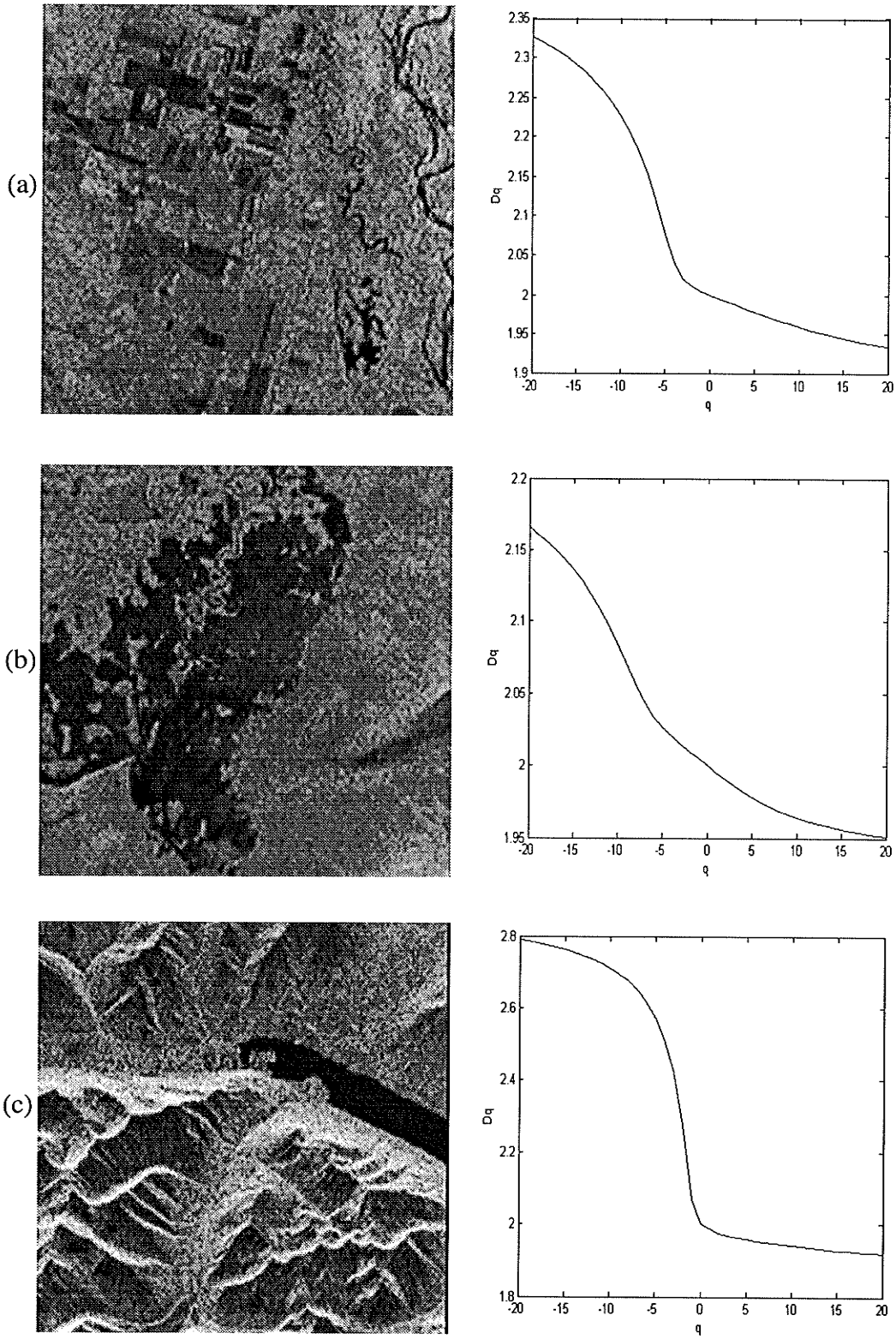

Fig. 7.4 Processed SAR images and their Rényi spectrum.

7.3.2 The Hölder Exponents

To estimate the Hölder exponents at each pixel, a 9 x 9 window is used and the corresponding exponent for every point in the image is obtained from the log-log plot of the wavelet modulus versus the scale. As the analyzing wavelet has only one vanishing moment, it detects only singularities exponents below 1. This is sufficient in this case as most interesting information is carried by the most singular edges.

The fractal components are then formed from sets of pixels having the same Hölder exponents. Among these sets, one is of great importance. It is called the *most singular manifold* (MSM) and is defined as the set of pixels having the minimum Hölder exponent h_{min}. The importance of the MSM comes from its ability to characterize the multifractal spectrum as it is seen in the following section.

7.3.3 The Multifractal Singularity Spectrum

To estimate the singularity spectrum, this thesis adopts the general expression for a log-Poisson singularity spectrum which is given by [TuPa00]

$$D(h) = D_{min} + \frac{h - h_{min}}{\gamma}\left[1 - \log\left(\frac{h - h_{min}}{\gamma(2 - D_{min})}\right)\right] \tag{7.5}$$

where $\gamma = -\log\left(1 + \frac{h_{min}}{(2 - D_{min})}\right)$, and D_{min} is the fractal dimension of the MSM.

Notice from Eq. 7.5 that the multifractal singularity spectrum is fully determined from the MSM characteristics h_{min} and D_{min}. Although a wide collections of natural images belongs to this class of log-Poisson multifractals, no hypothesis for SAR images is made. Many other spectrum estimation techniques are valid for SAR images but they suf-

fer from the numerical instability, and Eq. 7.5 is believed to give a good approximation for SAR image spectrum if an accurate evaluation of the MSM parameters is performed.

7.4 Segmentation of SAR Images

The proposed segmentation algorithm is summarized in the following

Table 7.2: Segmentation Algorithm for SAR images

Steps	Operation
1	• Compute the Hölder exponents of the image.
2	• Detemine the MSM.
3	• Estimate the fractal dimension of the MSM.
4	• Compute the singularity spectrum at each pixel from Eq. 7.5.
5	• Use the spectrum image as feature's space for the K-means algorithm for pixel classification.

To estimate the fractal dimension of the MSM, the IFS algorithm described in Ch. 6 is used.

7.4.1 Estimating Fractal Dimension with IFSs

The standard techniques for fractal dimension estimation have many limitations. For example, the power spectrum technique can be ineffective if the data are not from a fractional Brownian motion model. The box-counting can also be inefficient when it is applied to data-limited. In contrast, the IFS does not have these limitations. The IFS does not assume any statistical model and can be very efficient for different data.

To determine the fractal dimension of the MSM, a plot is derived by transforming the corresponding pixels to a curve. This approach is believed to preserve the fractal characteristics [PeLo97]. The vertical scaling factors of the IFS model are taking as function values at the first, middle, and last points of the curve as mentioned in [PeLo97]. The fractal dimension is then obtained from

$$D_{min} = 1 + \frac{\log\left(\sum_i |d_i|\right)}{\log K} \tag{7.6}$$

where d_i are the scaling factors, and K is the number of maps.

Table 7.2 shows the minimum Hölder exponent for each image as well as the corresponding fractal dimension.

Table 7.3: Minimum Hölder exponent and the MSM fractal dimension.

Image	h_{min}	D_{min}
E1	-0.01	1.23
E2	-0.006	1.02
R1	-0.34	1.37

7.4.2 Segmentation Results

To highlight the edges of various textures, the well-known K-means algorithm [MiAn73] is applied to the obtained spectrum image. Once K is fixed (K = 2 in this work), this unsupervised algorithm finds the minimum mean squared error fit of the data to the K prototypes. After mapping to the image space, the results are shown in Fig. 7.5.

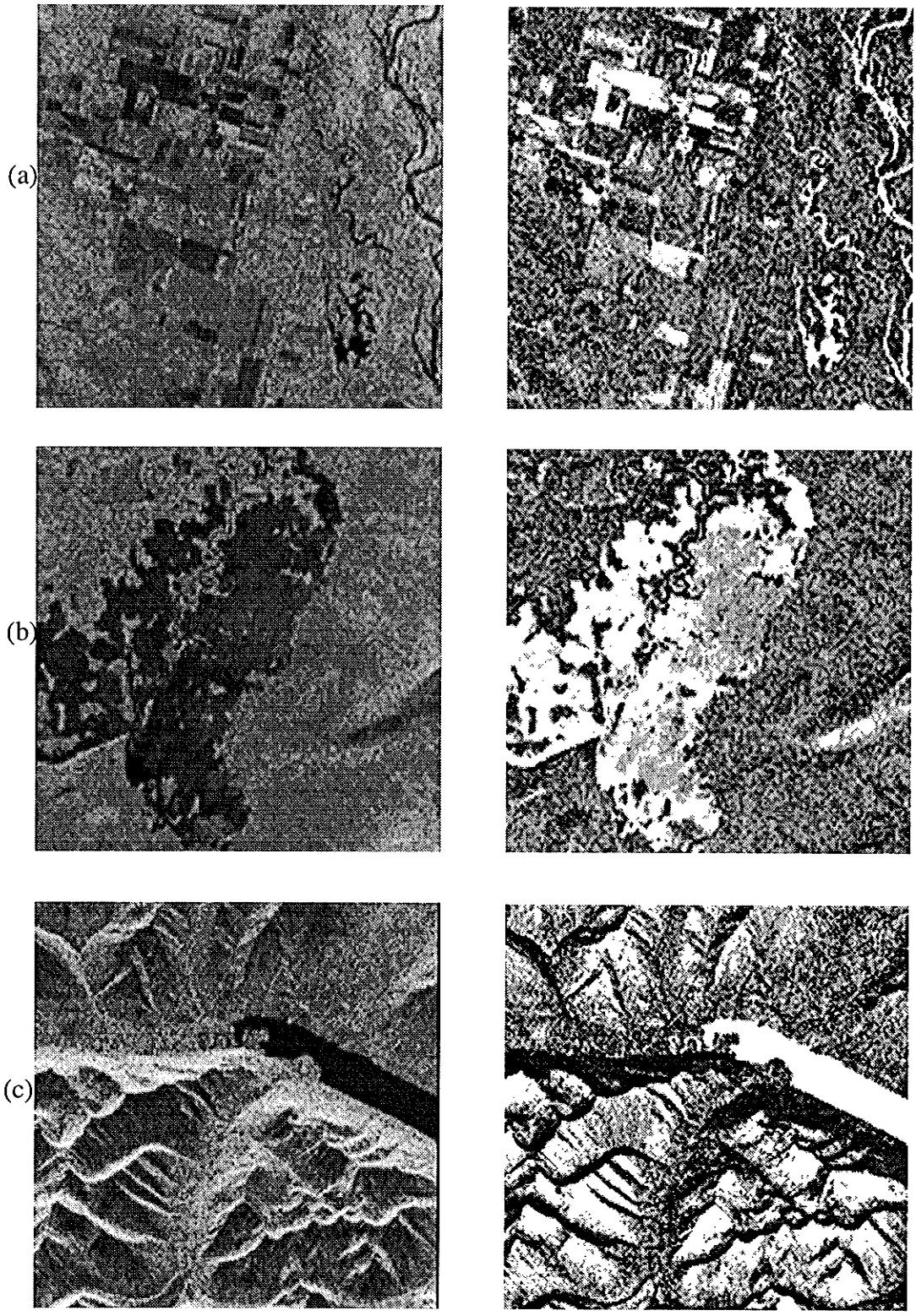

Fig. 7.5 The Original and the segmented images. (a) E1, (b) E2, and (c) R1.

The textures are clearly classified as can be seen from the segmented images. Both the lakes on the two images are highlited and their shapes are accurately drawn. Morever, the structure of the road and the farms on the E1 image is well preserved and clearly shown.

7.5 Coding

The segmentation algorithm for SAR images was coded in Matlab 6.5. The most computationaly intensive part of the algorithm was the calculation of Hölder exponent for each image . In order to find the Hölder exponent, a 9x9 pixel window size was selected for each scale (8 in total in this case) and this calculation took about 40 seconds for each image. The computer used for this purpose was Intel based Pentium-4 2.4 GHZ, with 512 Mbytes of RAM.

7.6 Summary

This chapter presented an algorithm combining multifractal analysis and the iterated function system. The theoretical development is very sound. The application of the proposed algorithm to the SAR images characterized by speckle noise, and known to be difficult to segment, shows very promising qualitative results. The image textures were described and discriminated efficiently, leading to the conclusion that multifractal analysis is a good tool for SAR image segmentation.

CHAPTER VIII

CONCLUSIONS AND RECOMMENDATIONS

8.1 Conclusions

In this work, the application of neural networks, wavelets, wavelets packet, wavelet optimality, and multifractal analysis for raw SAR data compression and SAR image segmentation has been studied. Throughout the development of this thesis, tests were run on pre-conditioned raw SAR datasets to evaluate the performance of each compression technique. Each contribution from each technique is compared to the performance of the popular technique, mainly to the Block Adaptive Quantization (BAQ).

Based on different books and papers, a critical review of the SAR principles and a SAR system is presented. This review shows that the SAR processor is a linear system able to achieve a high range and azimuth resolution independently of the distance radar-target. The statistical properties of the signal lead to the identification of the components of raw SAR signal as Gaussian distributed with a low variation in the signal power. This model was confirmed on real SAR data sets. To convert data to 8 bits, a new raw SAR data pre-conditioning technique is developed using cubic spline interpolation and produces better results than the existing pre-conditioning techniques.

Current techniques for raw SAR data compression have been analyzed in this thesis. Due to its importance, the BAQ algorithm was discussed in more details. Although the BAQ algorithm is attractive due to its simplicity, other techniques have been developed because BAQ has a low SQNR performance when compared to the Shannon

bound. Techniques using vector quantization such as BAVQ give better performance, but with the price of an increase of the computation complexity. Finally, a neural networks based technique is presented. Considering both the compression ratio and the distortion error (SQNR greater than BAQ), this technique appears to be an efficient way for raw SAR data compression.

The wavelets and wavelet packets are also investigated in this thesis, due to their time-frequency localization. A transform-based compression system was presented using: (i) standard wavelets including the Haar wavelet, the Battle-Lemarié wavelets (linear and quadratic) and Daubechies wavelets (D4 and D20), and (ii) wavelet packet tree with Haar, as well as D4 and D20 bases. The transformed data are then quantized using a bit allocation strategy. While the wavelet decomposition produces signal components whose spectra form consecutive octave bands, the wavelet packet decomposition provides a finer spectral resolution. Experimental results point out advantages and drawbacks of both approaches and show that the use of wavelet packet is more adequate than the wavelet transform. The quality reconstruction is very good; however, further improvement of the SQNR has to be made. It was found that none of the standard wavelet basis produced an SQNR performance greater than BAQ. The different wavelets showed very little variation with all wavelets differing by a maximum of only 0.09 dB for 2 bits/sample quantization.

Due to noise-like characteristics of the raw SAR signal, the standard wavelets are not very efficient in compacting energy in the transform domain. This has lead to orient the research to wavelet optimality, combined with an efficient quantization strategy. In this spirit, a method was proposed to determine an optimal 2-D wavelet which is learned

directly from the raw SAR data. The optimality criterion in the learning processes is redundancy minimization in the transform domain. More precisely, the wavelet coefficients at different scales should be as independent as possible. Experiments show that this single-orientation optimal wavelet performs better than the vertical Haar wavelet. There is however a lack of completeness with one orientation, which can be addressed by introducing new orientations of the optimal wavelet.

The last part of the thesis presents an algorithm combining multifractal analysis and the iterated function systems. Its complete theoretical basis has been developed. The application of the proposed algorithm to the SAR images characterized by speckle noise, and known to be difficult to segment, shows very promising qualitative results. The image textures were described and discriminated efficiently, leading to the conclusion that multifractal analysis is a good tool for SAR image segmentation.

8.2 Contributions

The main contributions of this thesis and the research done towards its completion are summarized as follows:

1. The development of a raw SAR data pre-conditioning technique for reduced dynamic range test sets that produces superior quality test sets than the standard pre-conditioning techniques.

2. A deep study of quantization and bit allocation strategies. Both theoretical and practical aspects are treated.

3. An extensive study of the different techniques for raw SAR data compression, their implementation, and comparison.

4. The implementation of a back-propagation neural network-based technique for the compression of raw SAR data. This technique, shown to approximate the KLT transform, provides an SQNR greater than BAQ, and permits a compression with a fractional number of bits.

5. A presentation of wavelet theory, as well as the development of a new compression scheme using wavelets, leading to the wavelet-BAQ algorithm. The wavelet packets are also studied and implemented for raw SAR data compression.

6. Derivation of a new optimal wavelet for raw SAR data compression able to minimize redundancy in the transform domain. The implementation does not use the standard MRA algorithm but a new scheme for computation.

7. A presentation of the theoretical framework combining wavelets and multifractal analysis, as well as iterated function systems.

8. Development of a new technique for SAR image segmentation based on multifractal analysis and iterated function systems showing very promising results.

8.3 Recommendations

Based on the work done in this thesis, the following recommendations are suggested for future work in this area:

1. Introduction of new orientations of the optimal wavelet in order to have a complete basis and then a perfect reconstruction of the signal.

2. Extention of the optimal wavelet formalism to the case of wavelet packet to obtain a maximum compression rate while keeping a good quality reconstruction.

3. Other approaches for estimating both the Rényi fractal dimension spectrum and the multifractal singularity spectrum should be elaborated for an accurate approximation.

4. Comparison of the segmentation results of Ch. 7 with other published results using different approaches.

5. The use of a combination of the probabilistic neural-network and the multifractal spectrum as a feature space for SAR image classification and segmentation.

REFERENCES

[Algr00] T. Algra, "Compression of raw SAR data using entropy-constrained quantization," in *Proceedings of the International Geoscience and Remote Sensing Symposium (IGARSS'00)*, pp. 2660-2662, 2000.

[AlUn93] A. Aldroubi and M. Unser, "Families of multiresolution and wavelet spaces with optimal properties," *Numer. Func. Optim.*, vol. 14, no. 5-6, pp. 417-446, 1993.

[Arno87] D. V. Arnold, "Vector quantization of synthetic array radar data," M.S. thesis, Brigham Young University, Provo, Utah, USA, 1987.

[ArVE99] G. Arslan, M. Valliappan, and B. L. Evans, "Quality assessment of compression techniques for synthetic aperture radar images," in *Proceedings of the International Conference on Image Processing*, pp. 857-861, 1999.

[Atte91] E. P. W. Attema, "The active microwave instrument on-board the ERS-1 satellite," *Proceedings of the IEEE*, vol. 79, pp. 791-799, June 1991.

[BaDe85] M. F. Barnsley and S. Demko, "Iterated function systems and the global construction of fractals," *Pro. Roy. Soc.*, London, vol. A399, pp. 243-275, 1985.

[Barn93] M. F. Barnsley, *Fractal Everywhere.* Academic Press, INC., 1993.

[BaSl88] M. F. Barnsley and A. D. Sloan, "A better way to compress images," Byte, January 1988.

[Baxt99] R. A. Baxter, "SAR image compression with the Gabor transform," *IEEE Transactions on Geoscience and Remote Sensing*, vol. 37, no. 1, pp. 574-588, January 1999.

[Benz94] U. C. Benz, "A fuzzy block adaptive quantizer for synthetic aperture radar," in *Proceedings of the IEEE Conference on Fuzzy Systems*, pp. 1006-1011, 1994.

[Berk97] K. Berkner, "A wavelet-based solution to the inverse problem for fractal interpolation functions," in Lévy Véhel, Lutton, Tricot (eds.) *Fractals in Engineering '97,* Springer-Verlag, 1997.

[BeSM95] U. Benz, K. Strodl, and A. Moreira, "A comparison of several algorithms for SAR raw data compression," *IEEE Transactions on Geoscience and Remote Sensing*, vol. 33, pp. 1266-1276, September 1995.

[Bolle97] J. Bolle, "Coding of SAR raw data using reversible transforms," in *Proceedings of the Internation Airborne Remote Sensing Conference and Exibition*, pp. 122-129, 1997.

[Bolle98] J. Bolle, "Coding of SAR raw data," *the European Conference on Synthetic Aperture Radar*, Friedrichshafen, Germany, 1998.

[Bovi88] A. C. Bovik, "On detecting edges in speckle imagery," *IEEE Transactions on Acoustic, Speech, and Signal Processing,* vol. 36, pp. 1618-1627, October 1988.

[Brow67] W. M. Brown, "Synthetic aperture radar," *IEEE Transactions on Aerospace and Electronic Systems*, vol. AES-3, pp. 217-229, March 1967.

[BrEK02] K. Brunham, A. El Boustani, and W. Kinsner, "A study of bit planes for the compression of raw synthetic aperture radar data," in *Proceedings of the Canadian Conference on Electrical and Computer Engineering* (CCECE'02), Winnipeg, Canada, pp. 347-352, May 2002.

[Brun02] K. Brunham, "Development of an FPGA based wavelet transformer for the compression of raw synthetic aperture radar data," M.S. thesis, University of Manitoba, Manitoba, Canada, 2002.

[BuSi99] R. W. Buccigrossi and E. P. Simoncelli, "Image compression via joint statistical characterization in the wavelet domain," *IEEE Transactions on Image Processing*, vol. 8, pp. 1688-1701, December 1999.

[ChDo94] S. Chen and d. Donoho, "Basis pursuit," *IEEE Transactions 28th Annu. Asilomar Conf. Signals, Syst., Comput.,* November 1994.

[ChRa00] J.O. Chapa and R.M. Rao, "Algorithms for designing wavelets to match a specified signal," *IEEE Transactions on Signal Processing*, vol. 48, no. 12, pp. 3395-3406, December 2000.

[Chui92] C. K. Chui, *An Introduction to Wavelets*. Academic Press, New York, 1992.

[CLPV66] L. J. Cutrona, E. N. Leith, L. J. Porcello, and W. E. Vivian, "On the application of coherent optical processing techniques to synthetic-aperture radar," *Proceedings of the IEEE*, vol. 54, pp. 1026-1032, August 1966.

[CoMW92] R. R. Coifman, Y. Meyer, and M. V. Wickerhauser, "Wavelet analysis and signal processing," *Wavelet and their applications,* M. B. ruskai *et al.* (Eds.), Jones and Bartlett, pp. 153-178, 1992.

[CoMZ87] G. W. Cotrell, P. Munro, and D. Zipser, "Learning internal representations from grey-scale images: an example of extensional programming," *Proc. 9th Annual Cognitive Science Society Conf.,* Seattle, WA, pp. 461-473, 1987.

[Cook60] C. E. Cook, "Pulse compression - Key to more efficient radar transmission," *Proceedings of the IRE*, vol. 48, pp. 310-316, March 1960.

[CoTh91] T. Cover and J. Thomas, *Elements of Information Theory.* NY, John Wiley & Sons, 1991.

[CoWi92] R. R. Coifman and M. V. Wickerhauser, "Entropy-based algorithms for best basis selection," *IEEE Transactions on Information Theory*, vol. 38, no. 2, pp. 713-718, March 1992.

[CuHa62] L. J. Cutrona and G. O. Hall, "A comparison of techniques for achieving fine azimuth resolution," *IRE Transactions on Military Electronics*, vol. MIL-6, pp. 119-121, April 1962.

[CuMc91] J. C. Curlander and R. N. McDonough, *Synthetic Aperture Radar: Systems and Signal Processing*. New York, NY: Wiley, 1991.

[CVLH61] L. J. Cutrona, W. E. Vivian, E. N. Leith, and G. O. Hall, "A high-resolution radar combat-surveillance system," *IRE Transactions on Military Electronics*, vol. MIL-5, pp. 127-131, April 1961.

[Dans01] R. Dansereau, "Progressive image transmission using fractal and wavelet techniques with image complexity measures," Ph.D dissertation, University of Manitoba, Winnipeg, MB, Canada, 2001.

[Daub90] I. Daubechies, "The wavelet transform, time-frequency localization and signal analysis," *IEEE Transactions on Information Theory*, vol. 36(5), pp. 961-1005, September 1990.

[Daub92] I. Daubechies, *Ten Lectures on Wavelets*. Philadelphia, PA: Society for Industrial and Applied Mathematics, 1992.

[Deca89] S. E. Decatur, "Application of neural networks to terrain classification," *Proceedings of the International Joint Conference on Neural Networks*, Washington, DC, 18-22 June 1989, vol. 1, pp. 283-288, June 1989.

[DoFM03] Y. Dong, B. C. Forster, and A. K. Milne, "Comparison of radar image segmentation by Gaussian- and Gamma- Markov random field models," *International Journal of Remote Sensing,* vol. 24, no. 4, pp. 711-722, 2003.

[DuCu92] M. Dutkiewicz and I. Cumming, "Methods of evaluating the effects of coding on SAR data," in *Proceedings of the NASA Space and Earth Science Data Compression Workshop*, pp. 59-72, 1992.

[DuCu94] M. Dutkiewicz and I. Cumming, "Evaluation of the effects of encoding on SAR data," *Photogrammetric Engineering and Remote Sensing*, vol. 60, pp. 895-904, July 1994.

[Dutk93] M. Dutkiewicz, "SAR pre-processing on-board ERS-1 data pre-conditioning," MacDonald Dettwiler, Richmond, BC, Canada, MDA Technical Report DC-TN-50-5137, ESA Technical Report ESA CR(P) 3792, 1993.

[DuYe02] G. Du and T. S. Yeo, "A novel lacunarity estimation method applied to SAR image segmentation," *IEEE Transactions on Geoscience and Remote Sensing,* vol. 40, no. 12, pp. 2687-2691, December 2002.

[EBJW82] C. Elachi, T. Bicknell, R. L. Jordan, and C. Wu, "Spaceborne syntheric-aperture imaging radars: Applications, techniques, and technology," *Proceedings of the IEEE*, vol. 70, pp. 1174-1209, October 1982.

[ElKi01] A. El Boustani and W. Kinsner, "Selective compression of MRI brain images using two classes of neural networks," in *Proceedings of the International Conference on Image and Signal Processing* (ICISP'01), Agadir, Morroco, May 3-5, 2001.

[ElBK01] A. El Boustani, K. Brunham, and W. Kinsner, "A review of current raw SAR data compression techniques," in *Proceedings of the Canadian Conference on Electrical and Computer Engineering* (CCECE'01), Toronto, Canada, vol. 2 of 2, pp. 925-930, May 13-16, 2001.

[Elbo02] A. El Boustani, "Compression des données brutes RSO avec les ondelettes," *Research report*, INRIA, UR Rocquencourt, France, April 2002.

[ETHB02] A. El Boustani, A. Turiel, A. Huot, K. Brunham, and W. Kinsner, "Wavelet transform based compression techniques for raw SAR data," in *Proceedings of the Canadian Conference on Electrical and Computer Engineering* (CCECE'02), Winnipeg, Canada, pp. 857-862, May 2002.

[ElBK03a] A. El Boustani, K. Brunham, and W. Kinsner, "An optimal wavelet for raw SAR data compression," in *Proceedings of the Canadian Conference on Electrical and Computer Engineering* (CCECE'03), Montréal, Canada, May 2003.

[ElBK03b] A. El Boustani, K. Brunham, and W. Kinsner, "Investigation of wavelets for SAR Raw data compression," in *Proceedings of the International Geoscience and Remote Sensing Symposium* (IGARSS'03), Toulouse, France, July 21-25, 2003.

[ElKi03] A. El Boustani and W. Kinsner, "SAR raw data compression: Wavelet packet versus wavelet," in *Proceedings of the International Conference on Image and Signal Processing* (ICISP'03), Agadir, Morroco, June 2003.

[ElKi04] A. El Boustani and W. Kinsner, "SAR raw data compression: Wavelet packet versus wavelet," *Journal of Control, Computer Science, and Signal Processing.* 2004 (In press).

[ESKW04] A. El Boustani, S. Siddiqui, W. Kinsner, and S. Wesolkowski, "A multifractal analysis approach for SAR image segmentation," in *Proceedings of the IEEE Canadian Conference on Electrical and Computer Engineering* (CCECE'04), Niagara Falls, Canada, pp. 1427-1430, May 2-5, 2004.

[EZWJ02] A. El Zaart, D. Ziou, S. Wang, and Q. Jiang, "Segmentation of SAR images," *Pattern Recognition,* vol. 35, pp. 713-724, 2002.

[Falc90] K. Falconer, *Fractal geometry: Mathematical Foundations and Applications.* John Wiley and sons Ltd, 1990.

[FiBM99] T. R. Fischer, U. Benz, and A. Moreira, "Efficient SAR raw data compression in frequency domain" *Proceedings of IGARSS'1999,* pp. 2261-2263, 1999.

[FiMW91] T. R. Fischer, M. W. Marcellin, and M. Wang, "Trellis-coded vector quantization," *IEEE Transactions on Information Theory,* vol. 37, pp. 1551-1566, November 1991.

[FLMC98] R. Fjortoft, A. Lopès, P. Marthon, and E. Cuberto-Castan, "An optimal multiedge detector for SAR image segmentation," *IEEE Transactions on Geoscience and Remote Sensing,* vol. 36, no. 3, pp. 793-802, May 1998.

[FoBB01] S. Foucher, G. B. Bénié, and J. M. Boucher, "Multiscale MAP filtering of SAR images," *IEEE Transaction on Image Processing,* vol. 10, no. 1, pp. 49-60, january 2001.

[Fouc00] S. Foucher, "Analyse multiéchelle d'images radar: Application au filtrage, a la classification et à la fusion d'images radar et optique," Ph.D dissertation, Université de Sherbrooke, Sherbrooke, Quebec, Canada, 2000.

[Gabo46] D. Gabor, "Theory of communication," *J. Inst. Elect. Eng.*, vol. 93, no. 3, pp. 429-457, 1946.

[GaSm96] L. Gagnon and F. D. Smaili, "Speckle noise reduction of airborne SAR images with symmetric Daubechies wavelets," *In Proc. SPIE Signal Data Processing Small Targets*, 1996.

[GeGr91] A. Gersho and R. M. Gray, *Vector Quantization and Signal Compression*. Norwell, MA: Kluwer Academic Publishers, 1991.

[GeRe01] O. Germain and P. Réfrégier, "Edge location in SAR images: performance of the likelihood ratio filter and accuracy improvement with an active contour approach," *IEEE Transactions on Image Processing,* vol. 10, no. 1, pp. 72-78, January 2001.

[GHKM87] A. Grossman, M. Holschneider, R. Kronland-Martinet, and J. Morlet, "Detection of abrupt changes in sound signals with the help of wavelet transforms," *In Inverse Problems*, pp. 289-306, Academic Press, 1987.

[GoCh99] J. C. Goswami, and A. K. Chan, *Fundamentals of Wavelets: theory, Algorithms, and Applications*. John Wiley & Sons, 1999.

[GoOB94] R. A. Gopinath, J. E. Odegard, and C. S. Burrus, "Optimal wavelet representation of signals and the wavelet sampling theorem," *IEEE Transaction on Circuits and Systems-II: Analog and Digital Signal Processing*, Vol. 41, no. 4, pp. 262-277, April 1994.

[Good75] J. W. Goodman, "Statistical properties of laser speckle patterns," in *Laser Speckle and Related Phenomena*, Vol. 9, *Topics in Applied Physics*, J. C. Dainty, Ed. Berlin: Springer-Verlag, 1975.

[GoWo92] R. C. Gonzalez and R. E. Woods, *Digital Image Processing*. New York, NY: Addison-Wesley Publishing, 1992.

[Gray84] R. M. Gray, "Vector quantization," *IEEE Acoustics, Speech, and Signal Processing Magazing*, pp. 4-29, April 1984.

[GrNe98] R. M. Gray and D. L. Neuhoff, "Quantization," *IEEE Transactions on Information Theory*, vol. 44, pp. 2325-2383, October 1998.

[GrPr83] P. Grassberger and I. Procaccia, "Characterization of strange attractor," Phys. Rev. Lett., vol. 50, no. 5, pp. 346-349, Jan. 1983.

[HaAY94] Y. Hara, R. G. Atkins, and S. H. Yaeh, "Application of neural networks to radar image classification," *IEEE Transactions of Geoscience and Remote Sensing*, vol. 32, no. 1, pp. 100-109, 1994.

[Hart91] D. Harte, *Multifractals: Theory and Applications*. Chapman & Hall/CRC, 2001.

[HOCC88] J. E. Harris, R. S. Ostler, D. M. Chabries, and R. W. Christiansen, "Quality measures for SAR images," in *Proceedings of the International Conference on Acoustics, Speech, and Signal Processing*, pp. 1064-1067, 1988.

[Horr99] M. S. Horritt, "A statistical active contour model for SAR image segmentation," *Image and Vision Computing*, vol. 17, pp. 213-224, 1999.

[Houd94] C. Houdre, "Wavelets, probability, and statistics: Some bridges," CRC Press, pp. 365-398, 1994.

[Huan03] B. Huang, "Compression of ECG signals with feature extraction, classification, and browsability," Ph.D dissertation, University of Manitoba, Winnipeg, MB, Canada, 2003.

[Hune89] B. L. Huneycutt, "Spaceborne imaging Radar-C instrument," *IEEE Transactions of Geoscience and Remote Sensing*, vol. 27, pp. 164-169, March 1989.

[Hune90] B. L. Huneycutt, "Innovative operating modes and techniques fot the spaceborne imageing Radar-C instrument," *IEEE Transactions of Geoscience and Remote Sensing*, vol. 28, pp. 603-608, July 1990.

[Jaff91] S. Jaffard, "Pointwise smoothness, two-microlocalization and wavelet coefficients," *Publications Matematiques*, vol. 35, pp. 155-168, 1991.

[Jian99] J. Jiang, "Image compression with neural networks: a survey," Signal processing: image Communication, vol. 14, pp. 737-760, 1999.

[JoHW91] R. L. Jordan, B. L. Huneycutt, and M. Werner, "The SIR-C/X-SAR synthetic aperture radar system," *Proceedings of the IEEE*, vol. 79, pp. 827-838, June 1991.

[JVFC88] R. V. Jones, V. D. Vaughn, R. L. Frost, and D. M. Chabries, "The effect of codebook size on the vector quantization of SAR data," in *Proceedings of the IEEE National Radar Conference*, 1988, pp. 129-133.

[Kais94] G. Kaiser, *A Friendly Guide to Wavelets*. Boston, MA: Birkhäuser, 1994.

[KäWi91] D. Kähry and W. Wiesbeck, "Optimum input parameters for classification of multi-frequency polarimetric SAR data using neural networks," Proceedings of the International *Geoscience and Remote Sensing Symposium* (IGARSS'91), Espoo, Finland, vol. iv, pp. 2157-2160, June1991.

[Kesh82] M. S. Keshner, "1/f noise," *Proceedings of the IEEE*, vol. 70, pp. 212-218, Marsh 1982.

[Kins94a] W. Kinsner, "Fractal dimension: morphological, entropy spectrum, and variance classes," *Technical Report, DEL 94-4*, Department of Electrical and Computer Engineering, University of Manitoba, May 1994, 146 pp.

[Kins94b] W. Kinsner, "Batch and real-time computation of a fractal dimension based on variance of a time series," *Technical Report, DEL 94-6*, Department of Electrical and Computer Engineering, University of Manitoba, May 1994, 22 pp.

[Kins95] W. Kinsner, "Self-similarity: fractals, chaos, scaling and their application," *Technical Report, DEL 95-2*, Department of Electrical and Computer Engineering, University of Manitoba, Jan. 1995, 113 pp.

[Kova76] J. J. Kovaly, *Synthetic Aperture Radar*. Dedham, MA: Artec House, 1976.

[Kram91] M. A. Kramer, "Nonlinear principal component analysis using autoassociative neural networks," *AIChE Journal,* vol. 37, pp. 233-243, 1991.

[KuDC94] G. Kuduvalli, M. Dutkiewicz, and I. Cumming, "Synthetic aperture radar sugnal data compression using block adaptive quantization," in *Proceedings of the Goddard Science Information Management and Data Compression Workshop*, 1994, pp. 43-57.

[KwJo89] R. Kwok and W. T. K. Johnson, "Block adaptive quantization of Magellan SAR data," *IEEE Transactions of Geoscience and Remote Sensing*, vol. 27, pp. 275-383, July 1989.

[Lawt91] W. M. Lawton, "Necessary and sufficient conditions for constructing orthonormal wavelet bases," *journal of mathematical Physics,* vol. 32(1), pp. 57-61, January 1991.

[Lebe95] D. Lebedeff, "Étude de la quantification vectorielle des données brutes issues d'un radar à synthèse d'ouverture," Ph.D dissertation, Université de Nice-Sophia Antipolis, Nice, France, 1995.

[LiBG80] Y. Linde, A. Buzo, and R. M. Gray, "An algorithm for vector quantizer design," *IEEE Transactions on Communications*, vol. COM-28, pp. 84-95, January 1980.

[LiBu77] R. G. Lipes and S. A. Butman, "Bandwidth compression of synthetic aperture radar imagery by quantization of raw radar data," *Proceedings of the SPIE*, vol. 119, pp. 107-114, 1977.

[Lloy82] S. P. Lloyd, "Least squares quantization in PCM," *IEEE Transactions on Information Theory*, vol IT-28, pp. 129-137, March 1982.

[LMBL95] D. Lebedeff, P. Mathieu, M. Barlaud, C. Lambert-Nebout, and P. Bellemain, "Adaptive vector quantization for raw SAR data," in *Proceedings of the International Conference on Acoustics, Speech, and Signal Processing*, 1995, pp. 2511-2514.

[MaFC97] B. B. Mandelbrot, A. Fisher, and L. Calvet, "A Multifractal Model of Asset Returns," Cowles Foundation Discussion Paper 1164, Sept. 15, 1997, 39 pp.

[MaHw92] S. Mallat and W. L. Hwang, "Singularity detection and processing with wavelets," *IEEE Transactions on Information Theory*, vol. 38(2), pp. 617-643, March 1992.

[Mall89] S. Mallat, "A theory for multiresolution signal decomposition: The wavelet transform," *IEEE Transactions on Pattern Analysis and Machine Intelligence*, vol. 11, pp. 674-693, July 1989.

[Mall98] S. Mallat, *A Wavelet Tour of Signal Processing*. San Diego, CA: Academic Press, 1998.

[Mand82] B. B. Mandelbrot, *The Fractal Geometry of Nature.* New York, NY: W. H. Freeman, 1982.

[Mass93] J. L. Massey, *Applied Digital Information Theory I.* Course notes, Fach Nr. 35-417 G, Germany, Wintersemester 1992/1993.

[Max60] J. Max, "Quantizing for minimum distortion," *IRE Transactions on Information Theory*, pp. 7-12, March 1960.

[MaZh92] S. Mallat and Z. Zhong, "Characterization of signals from multiscale edges," *IEEE Transactions on Pattern Analysis and Machine Intelligence*, vol. 14, no. 7, pp. 710-732, July 1992.

[MaZh93] S. Mallat and Z. Zhong, "Matching pursuit with time-frequency dictionaries," *IEEE Transactions on Signal Processing*, vol. 41, pp. 3397-3415, December 1993.

[McCu95] I. H. McLeod and I. G. Cumming, "On-board encoding of the ENVISAT wave mode data," in *Proceedings of the International Geoscience and Remote Sensing Symposium*, 1995, pp. 1681-1683.

[MGBB94] J. M. Moureaux, P. Gauthier, M. Barlaud, and P. Bellemain, "Vector quantization of raw SAR data," in *Proceedings of the International Conference on Acoustics, Speech, and Signal Processing*, 1994, pp. 189-192.

[MiAn73] R. Michael and R. Anderberg, *Cluster Analysis for Applications.* New York: Academic, 1973.

[MMOP02] M. Misiti, Y. Misiti, G. Oppenheim, and J. Poggi, *Wavelet Toolbox User's Guide*, The Mathworks Inc., 2002.

[MoAA91] M. Mougeot, R. Azencott, and B, Angeniol, "Image compression with back-propagation: improvement of the visual restoration using different cost functions," *Neural networks,* 4(4), pp. 467-476, 1991.

[MoBl93] A. Moreira and F. Bläser, "Fusion of block adaptive and vector quantizer for efficient SAR data compression," in *Proceedings of the International Geoscience and Remote Sensing Symposium*, pp. 1583-1585, 1993.

[MuVi89] D. C. Munson and R. L. Visentin, "A signal processing view of strip-mapping synthetic aperture radar," *IEEE Transactions on Acoustics, Speech, and Signal Processing*, vol. 37, pp. 2131-2147, December 1989.

[Ning97] L. Ning, *Fractal Imaging.* Academic Press, 24-28 Oval Road, London, UK, 1997.

[OlBW96] C. J. Oliver, D. Blacknell, and R. G. White, "Optimum edge detection in SAR," *Inst. Elec. Eng. Proc. Radar Sonar Navigat.,* vol. 143, February 1996.

[Olms93] C. Olmsted, "Alaska SAR Facility Scientific SAR User's Guide," Alaska SAR Facility, Fairbanks, Alaska, Technical Report ASF-SD-003, July 1993.

[OlQu98] C. Oliver and S. Quegan, *Understanding synthetic aperture radar images.* Artech house, inc., 1998.

[OMHK99] J. W. Owens, M. W. Marcellin, B. R. Hunt, and M. Kleine, "Compression of synthetic aperture radar phase history data using trellis coded quantization techniques," in *Proceedings of the International Geoscience and Remote Sensing Symposium*, pp. 1080-1085, 1999.

[OMHK97] J. W. Owens, M. W. Marcellin, B. R. Hunt, and M. Kleine, "Compression of synthetic aperture radar phase history data using trellis coded quantization techniques," in *Proceedings of the Internation Conference on Image Processing*, pp. 592-595, 1997.

[Owen97] J. W. Owens, "Compression of synthetic aperture radar phase history data," Ph.D. dissertation, University of Arizona, Tucson, Arizona, USA, 1997.

[PaCl99] S. M. Parkes and H. L. Clifton, "The compression of raw SAR and SAR image data," *International Journal of Remote Sensing*, vol 20, pp. 3563-3581, December 1999.

[PaFr85] G. Parisi and U. Frisch, "On the singularity structure of fully developed turbulence," in *turbulence and predictictability in Geophysical Fluid Dynamics. Proc. Intl. School of Physics,* E. Fermi, M. Ghil, R. Benzi, and G. Parisi, Eds., Amsterdam, North Holland, pp. 84-87, 1985.

[Papo84] A. Papoulis, *Probability, Random variables, and Stochastic Processes.* Second Edition, NY: McGraw-Hill, 1984.

[PaSc87] K. Pawelzik and H. G. Schuster, "Generalized dimensions and entropies from a measured time series," Phys. Rev., vol. A35(1), pp. 481-84, Jan. 1987.

[PaSc99] V. Pascazio and G. Schirinzi, "Wavelet transform coding for SAR raw data compression," in *Proceedings of the International Geoscience and Remote Sensing Symposium*, 1999, pp. 2251-2253.

[PaSc00] V. Pascazio and G. Schirinzi, "SAR phase history data compression by using wavelet packets," in *Proceedings of the International Geoscience and Remote Sensing Symposium*, 2000, pp. 2639-2641.

[PaSB99] V. Pascazio, G. Schirinzi, and I. D. Buttarello, "Low bit rate transform coding for SAR raw data compression, " in *Proceeding of the IEEE Radar Conference*, 1999, pp. 233-236.

[PeLo97] A. I. Penn and M. H. Loew, "Estimating fractal dimension with fractal interpolation function models," *IEEE Transactions on Medical Imaging,* vol. 16, no. 6, pp. 930-937, December 1997.

[PrFT92] W. H. Press, B. P. Flannery, and S. A. Teukolsky, *Numerical Recipes in C: The Art of Scientific Computing*. Cambridge, England: Cambridge University Press, 1988.

[RACC88] C. J. Read, D. V. Arnold, D. M. Chabries, and R. W. Christiansen, "A computation compression technique for SAR based vector quantization," in *Proceedings of the IEEE National Radar Conference*, 1988, pp. 123-128.

[RLLA91] R. K. Raney, A. P. Luscombe, E. J. Langham, and S. Ahmed, "Radarsat," *Proceedings of the IEEE*, vol. 79, pp. 839-849, June 1991.

[Sayo96] K. Sayood, *Introduction to Data Compression*. San Francisco, CA: Morgan Kaufmann, 1996.

[SBBE94] K. Strodl, U. Benz, F. Bläser, T. Eiring, and A. Moreira, "A comparison of several algorithms for on-board SAR raw data reduction," in *Proceedings of the International Geoscience and Remote Sensing Symposium*, 1994, pp. 2197-2199.

[Shan48] C. E. Shannon, "A mathematical theory of communications," *The Bell System Technical Journal*, vol. 27, pp. 379-423, 623-656, July, October 1948.

[ShRR62] C. W. Sherwin, J. P. Ruina, and R. D. Rawcliffe, "Some early developments in synthetic aperture radar systems," *IRE Transactions on Military Electronics*, vol. MIL-6, pp. 111-115, April 1962.

[Schw97] L. Schwartz, *La Theorie Des Distributions*. Hermann & Cie, Paris, 1997.

[SiEK04] S. Siddiqui, A. El Boustani, and W. Kinsner, "Modelling multifractal object boundaries using iterated function system," *Proceedings of the IEEE Canadian Conference on Electrical and Computer Engineering* (CCECE04), Niagara Falls, ON, pp. 1431-1435, May 2-5, 2004.

[Skol70] M. I. Skolnik, *Radar Handbook*. New York, NY: McGraw-Hill, 1970.

[SmDe97] P. C. Smits and S. G. Dellepiane, "Synthetic aperture radar image segmentation by a detail preserving markov random field approach," *IEEE Transactions on Geoscience and Remote Sensing*, vol. 35, no. 4, pp. 844-857, July 1997.

[SMTH83] M. Sekine, Y. Mocha, T. Tomita, T. Hagisawa, T. Irabu, and E. kiuchi, "Weibull distributed sea clutter," IEE Proceedings F, vol. 130, p. 476, 1983.

[StNg96] G. Strang and T. Nguyen, *Wavelets and Filter Banks*. Wellesley, MA: Wellesley-Cambridge Press, 1996.

[Swel96] W. Sweldens, "The lifting scheme: A custom design construction of biorthogonal wavelets," *J. Appl. comput. Harmon. Anal., vol. 3,* no. 2, pp. 186-200, 1996.

[TeSJ92] A. H. Tewfik, D. Sinha, and P. Jorgensen, "On the optimal choice of a wavelet for signal representation," *IEEE Transactions on Information Theory*, vol. 38, pp. 747-765, March 1992.

[ToDL03] J. Tourneret, M. Doisy, and M. Lavielle, "Bayesian, off-line detection of multiple change-points corrupted by multiplicative noise: application to SAR image edge detection," *Signal Processing*, vol. 83, pp. 1871-1887, 2003.

[Tomi78] K. Tomiyasu, "Tutorial review of synthetic-aperture radar with applications to imaging of the ocean surface," *Proceedings of the IEEE*, vol. 66, pp. 563-583, May 1978.

[Touz88] R. Touzi, "Analyse d'images radar en télédétection: Améliorations radiométriques, filtrage du speckle et détection des contours," Ph.D dissertation, Université Paul sabatier, Toulouse, France, 1988.

[Touz99] R. Touzi, "Speckle filtering of stationary and nonstationary scene signals in SAR imagery," IGARSS'1999, vol. 3, pp. 1807-1809.

[TMPN97] A. Turiel, G. Mato, N. parga, and J.P. Nadal, "Self-similarity properties of natural images," *Proceedings of NIPS'97*, vol. 10, MIT press, pp. 836-842, 1997.

[Tree71] H. L. V. Trees, *Detection, Estimation and Modulation Theory.* New York, Wiley, vol. 3, 1971.

[Truc98] F. Truchetet, *Ondelettes pour Le Signal Numérique.* Editions HERMES, Paris, 1998.

[TuBA98] M. J. Turner, J. M. Blackledge, and P. R. Andrews, *Fractal Geometry in Digital Imaging. Wellesley*, SD: Academic Press, 1998.

[TuDe02] A. Turiel and A. Del Pozo, "Reconstructing images from their most singular fractal manifold," *IEEE Transactions on Image Processing,* vol. 11, pp. 345-350, 2002.

[TuPa00] A. Turiel and N. Parga, "The multifractal structure of contrast changes in natural images: from shap edges to textures," Neural Computation 12, pp. 763-793, 2000.

[VeHe92] M. Vetterl and C. Herley, "Wavelets and filter banks: theory and design," *IEEE Transactions on Signal Processing*, vol. 40, pp. 2207-2232, September 1992.

[VGBF03] M. Voorons, M. Germain, G. Bertin Bénié, and K. Fung, "Segmentation of high resolution images based on the multifractal analysis," *Proceedings of the International Geoscience and Remote Sensing Symposium, (IGARSS03)*, Toulouse, France, July 21-25, 2003.

[WeWC94] S. A. Werness, S. C. Wei, and R. Carpinella, "Experiments with wavelets for compression of SAR data," *IEEE Transactions of Geoscience and Remote Sensing*, vol. 32, pp. 197-201, Janvier 1994.

[Wils80] S. G. Wilson, "Magnitude/phase quantization of independent Gaussian variates," *IEEE Transactions on Communications*, vol. COM-28, pp. 1924-1929, November 1980.

[WiNC87] I. H. Witten, R. M. Neal, and J. G. Cleary, "Arithmetic coding for data compression," *Commun. of the ACM.,* vol. 30, pp. 520-540, June 1987.

[ZiLe77] J. Ziv and A. lempel, "A universal algorithm for data compression," *IEEE Transaction on Information Theory*, IT-23(3), pp. 337-343, May 1977.

APPENDIX A

RADAR AND DATA CHARACTERISTICS

A.1 Data Characteristics

As mentioned in Ch. 2, data were provided by the Alaska SAR facility (ASF). They are from three different satellites ERS-1, ERS-2, and Radarsat-1. The data sets are called E1-22089R, E2-551R, and R1-24576R, where the first letter corresponds to the first letter of the satellite and is followed by the number of the satellite (1 or 2). Then, the digits correspond to the serial numbers provided by ASF. The letter R refers to raw data.

Details of the original test sets are shown in Table A.1. Table A.2 shows the characteristics of Radarsat-1 and ERS-1.

Table A.1 Details of the raw SAR data test sets.

Test set	Radar	Bits per sample	Complex samples per range line	Range lines
E1-22089R	ERS-1	32	5544	26624
E2-551P	ERS-2	32	5616	20390
R1-24576R	RADARSAT-1	16	6708	64498

Table A.2 Characteristics of the Radarsat-1 [RLLA91] and ERS-1 [Atte91] radars.

	Radarsat-1 (Standard Mode)			**ERS-1** (Image Mode)
Radar Frequency (f_r)	5.3 GHz			5.3 GHz
Relative platform speed (V_s)	7402 m/s			7497 m/s
Platform Height (H)	800 km			785 km
Antenna height (L_g)	1.5 m			1m
Antenna length (L_a)	15 m			10 m
Beam incidence angle (θ)	20-49°			23°
Pulse bandwidth (B)	11.6	17.3	30 MHz	15.5 MHz
Sampling frequency (f_s)	12.9	18.5	32.3 MHz	18.96 MHz
Pulse repetition frequency (f_{prf})	1270-1390 Hz			1680 Hz
Time duration of pulse (τ_p)	42.0 μs			37.1μs
Ground swath width (W_g)	100 km			100 km
Azimuth resolution (δ_a)	25m			30 m
Ground range resolution (δ_g)	28 m			30 m
A/D converted bits	4 bits			5 bits
I/Q wordsize	4 bits			5 bits
Compression technique	none			none
Downlink channel bandwidth	105 Mbits/s			105 Mbit/s

A.2 Data Pre-processing

As described in Ch. 2, we use a cubic spline interpolation to convert data to 8 bits. The characteristics of the pre-processed data sets using cubic spline (PS) are shown in table A.3

Table A.3 Details of the pre-processed SAR data test sets.

Test set	Radar	Bits per sample	Spline offset	Quantization block size
E1-22089PS	ERS-1	256	0.08	1386
E2-5551PS	ERS-2	256	0.08	702
R1-24576PS	RADARSAT-1	256	0.3	3354

Tables A.4 and A.5 presents respectively the statistics of the E2-5551R and R1-24576R test sets as compared with the pre-conditioned data.

Table A.4 Statistics of the original and cubic spline pre-processed data from the E2-5551R test set.

Statistic	Original	Pre-processed
Entropy	4.04	7.11
Redundancy	0.96	0.89
Standard deviation	16.01	132.04
σ factor		8.25
Kurtosis	1.24	1.25
Skewness	1.09	1.09
Mean	0.001	0.01

Table A.5 Statistics of the original and cubic spline pre-processed data from the R1-24576R test set.

Statistic	Original	Pre-processed
Entropy	3.64	7.43
Redundancy	0.36	0.57
Standard deviation	8.06	133.84
σ factor		16.60
Kurtosis	1.53	1.37
Skewness	1.19	1.13
Mean	0.00	0.00

Figures A.1 to A.4 show the histograms of data sets E2-5551R and R1-24576R and the histograms of the corresponding cubic spline pre-processed sets E2-5551PS and R1-24576PS.

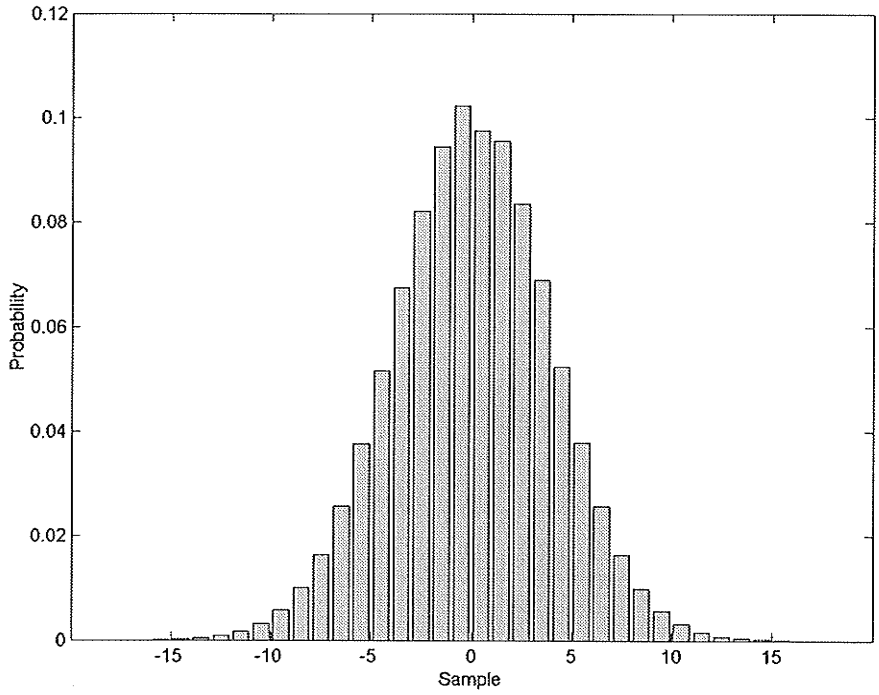

Fig. A.1 Histogram of E2-5551R data set.

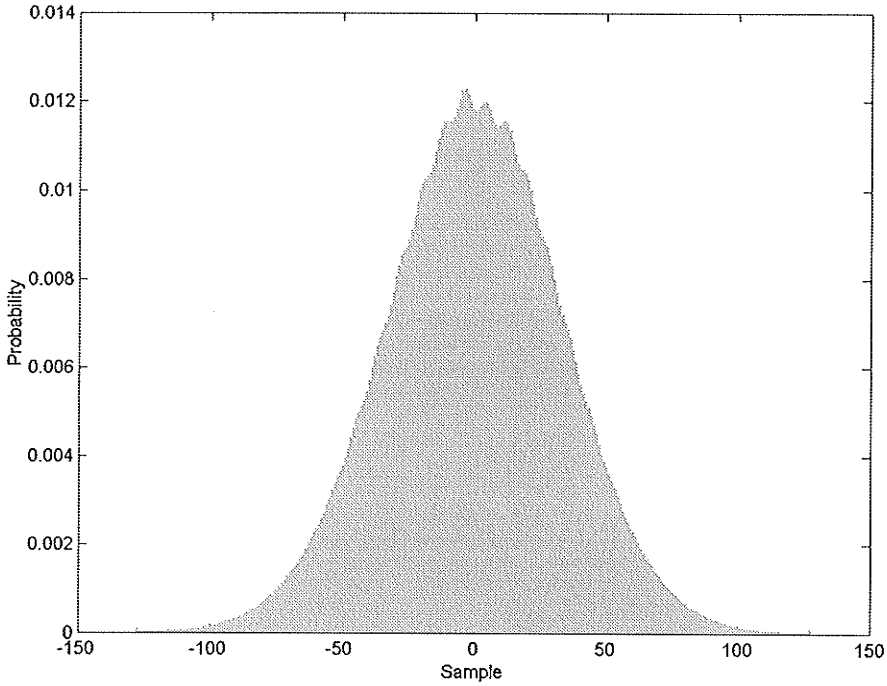

Fig. A.2 Histogram of E2-5551PS data set.

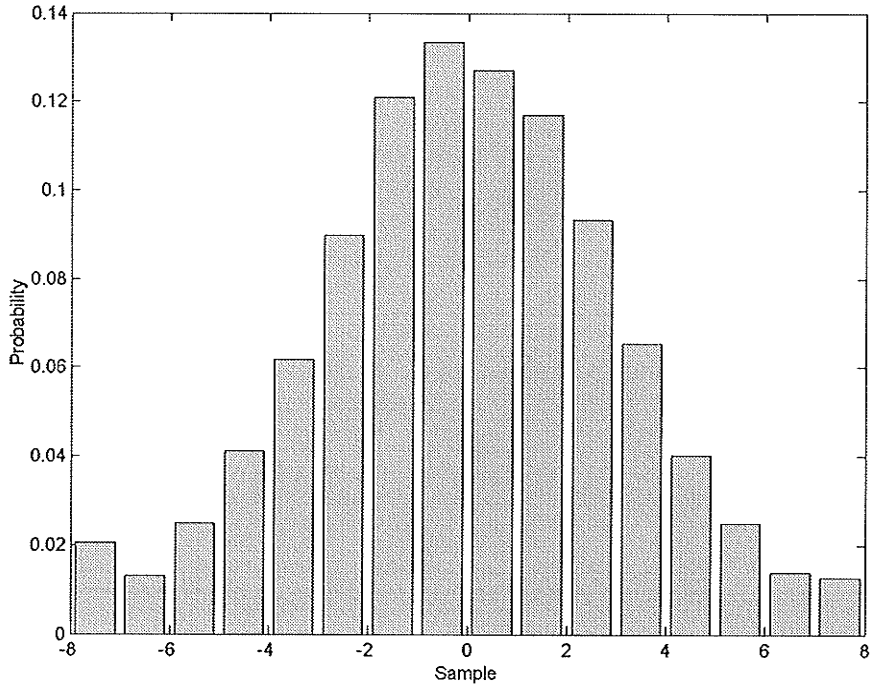

Fig. A.3 Histogram of R1-24576R data set.

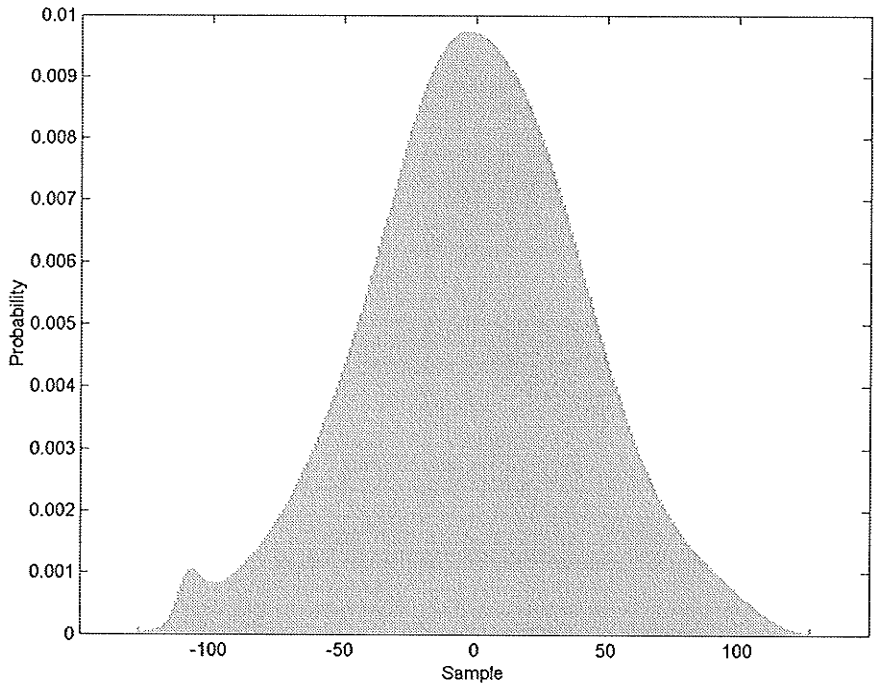

Fig. A.4 Histogram of R1-24576PS data set.

A.3 Processed Images

In order to obtain the SAR images, a processing of the raw data is necessary as described in Ch. 2 (the azimuth focusing). We used a software provided by ASF to process the three data sets. The obtained images are shown in figs A.5 to A.7.

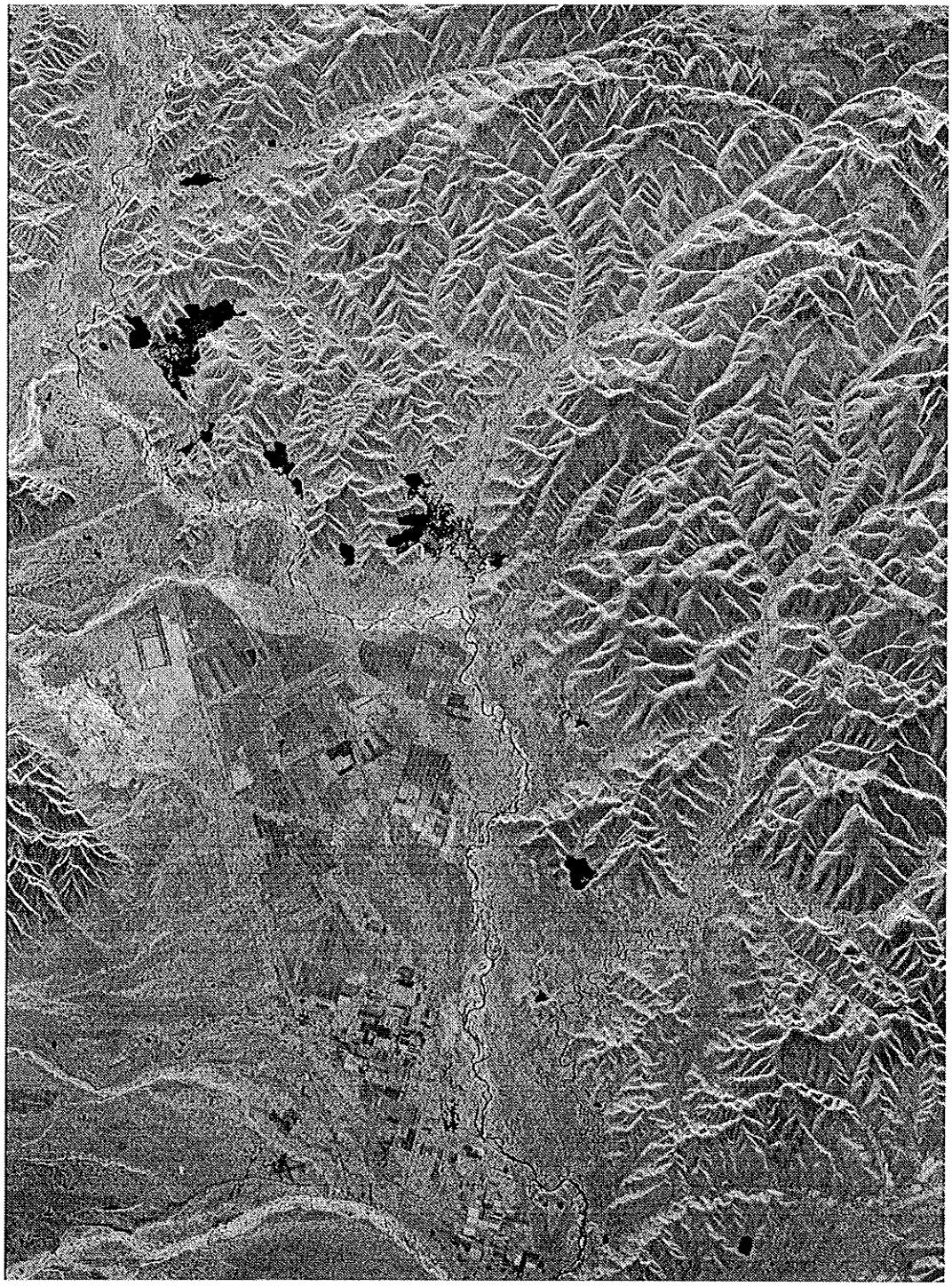

Fig. A.5 Processed amplitude image of E1-2208PS.

Fig. A.6 Processed amplitude image of E2-5551PS data set.

Fig. A.7 Processed amplitude image of R1-24576PS data set.